© Copyright by Oswaldo Russian, August 2016

All Rights Reserved

CASA AND PARAMETRIC STUDY ON THE COLLAPSE OF THE USS SALEM WHARF

A Thesis

Presented to

the Faculty of the Department of Civil and Environmental Engineering

University of Houston

In Partial Fulfillment

of the Requirements for the Degree

Master of Science

in Civil Engineering

by

Oswaldo Russian

August 2016

CASE AND PARAMETRIC STUDY ON THE COLLAPSE OF THE USS SALEM WHARF

Oswaldo Russian

Approved:

Chair of the Committee
Dr. Mina Dawood, Associate Professor,
Civil and Environmental Engineering

Committee Members:

Dr. Abdeldjelil Belarbi, Hugh Roy and Lillie Cranz Cullen Distinguished Professor,
Civil and Environmental Engineering

Dr. Paul Schuman, Senior Staff II, Simpson, Gumpertz & Heger, Inc.

Dr. Suresh K. Khator, Associate Dean,
Cullen College of Engineering

Dr. Roberto Ballarini, Professor and Chair,
Civil and Environmental Engineering

Acknowledgements

I would convey my sincere appreciation for my advisor, Dr. Mina Dawood, as his knowledge and vision are the pillars upon which this research stands. More importantly, his kindness, patience and understanding are vital to my academic career and personal life. He gave me my first opportunity and for that I will always be grateful.

Furthermore, I would gratefully acknowledge Dr. Paul Schuman and the team at Simpson, Gumpertz & Heger, Inc. (SGH) for their continued guidance and assistance during the realization of this research. Additionally, I would like to express my gratitude to Dr. Abdeldjelil Belarbi for being a valued member of my thesis committee and giving me his time and thoughtful recommendations.

The patience and guidance of Dr. Hossein Karagah and Dr. Cheng Shi were vital to the completion of this work and are gratefully acknowledged as such. Additionally, I would like to thank my friends Dr. Mossab El-Tahan, Dr. Aram Raheem, Mr. Ben Wang, and Mr. Botong Zheng for their support and advice throughout my experience at the University of Houston.

I would especially thank my sister, Gisselle, and brother-in-law, Edgar, for welcoming me into their home the last two years. I cannot do anything but assure them that my gratitude for this most wonderful act of generosity is undying. My aunt Iris and uncle Ned were also invaluable in providing me with caring support and structure throughout my stay in Houston.

Finally, I am most appreciative of my parents, Oswaldo and Arima, as well as my brothers and sisters Javier, Joanna, Gisselle, and Carla for their love and support. I am certain that their contributions to whatever accomplishments are ascribed to me greatly exceed my own. Making them proud is my biggest motivation and their happiness and peace determine my own. I am truly blessed to have them.

CASE AND PARAMETRIC STUDY ON THE COLLAPSE OF THE USS SALEM WHARF

An Abstract

Of a

Thesis

Presented to

the Faculty of the Department of Civil and Environmental Engineering

University of Houston

In Partial Fulfillment

of the Requirements for the Degree

Master of Science

in Civil Engineering

by

Oswaldo Russian

August 2016

Abstract

The research presented herein has two principal objectives, which are (i) to develop a numerical framework to predict the collapse load of highly redundant structures with stiff superstructures under vertical (gravity) loads considering the instability of severely corroded steel H-piles as the predominant failure mode, and (ii) to investigate the influence of sheet and battered piles, stiffness of the superstructure, redundancy of supporting elements, and distribution of corroded piles on the performance of wharf structures.

The findings of this research indicated that higher collapse loads corresponded to an increase in the number of buckled piles and that the stiffness of the superstructure was a principal factor in the resulting load redistribution capabilities of this type of structure. Additionally, results indicated that the performance of the USS Salem Wharf structure could be maintained with a reduced number of piles, if the superstructure stiffness reached a level corresponding to un-cracked concrete sections.

Table of Contents

List of Figures

List of Tables

Chapter 1 : Introduction

Corrosion deterioration of waterfront facilities, including piers, wharves, mooring structures and fuel lines is a serious problem affecting the US Navy (Naval Facilities Engineering Command, 1992). This type of degradation is also a concern for bridge structures constructed over waterways, which represent 83% of all bridges in the US (Collins Engineers, 2010). In general, structures where steel elements are subject to continuous wetting and drying cycles are subject to deterioration due to corrosion. Pile-supported wharves and bridges generally fit this description, and typically have stiff superstructures. Wharves are also characterized by the high-degree of redundancy in their substructure.

The behavior of steel piles with severe and localized corrosion has been investigated experimentally and numerically by Karagah, et al. (2015) and Shi, et al. (2014), respectively. However, the research done to date does not account for the system effects that incorporate the highly non-linear behavior of structural systems with stiff superstructures and a high degree of redundancy in the substructure. Assessing these effects is important, as substructure collapse induced by buckling of vertical piles under axial loads has been identified as a prevalent failure mode in structures with these characteristics (Bhattacharya, et al., 2008).

To study the performance and collapse of steel-pile-supported wharves, bridges, and similar structures under gravity loads it is necessary to incorporate the behavior of individual piles and its effect on that of the complete structural system. Achieving accurate representations of structural systems with these characteristics is complex because of the high degree of material and geometric non-linearity and the significant challenges associated with modeling very large structures (with overall dimensions in the tens to hundreds of feet), for which failure is heavily influenced by very small localized features (dimensions in the range of a fraction to tens of inches).

1.1 Objectives

This thesis presents the findings of a numerical investigation conducted with two primary objectives, which are (i) to develop a numerical framework to predict the collapse load of highly redundant structures with stiff superstructures under vertical (gravity) loads considering the instability of severely corroded steel H-piles as the predominant failure mode, and (ii) to investigate the influence of sheet and battered piles, stiffness of the superstructure, redundancy of supporting elements and distribution of corroded piles on the performance of wharf structures.

To these ends, the USS Salem Wharf is adopted as a test-bed structure due to the extensive database of corroded pile measurements available to inform the modeling effort.

1.2 Outline of Thesis

This thesis is comprised of five chapters. The problem statement, significance of research, objectives and outline of the thesis are summarized in this introductory chapter.

Chapter 2 presents a review of the relevant literature in two sections. The first section describes the history and current condition of the USS Salem Wharf. The second section summarizes the previous research on the performance evaluation of highly redundant structures with stiff superstructures in different contexts.

Chapter 3 describes the finite element model that was implemented to determine the axial load-shortening relationships of the corroded steel piles that support the USS Salem Wharf. This chapter also presents the results and discussion pertaining to these analyses.

Chapter 4 describes the numerical framework that was developed to evaluate the collapse of wharf structures under gravity loads. The chapter also presents the results and discussion for the case study of the USS Salem Wharf and the details of a parametric study that was performed to evaluate the influence of various parameters including influence of sheet and battered piles, stiffness of the superstructure, redundancy of supporting elements and distribution of corroded piles on the collapse behavior of the wharf.

The research conclusions are presented in Chapter 5, where recommendations for future work are also summarized.

Chapter 2 : Background

2.1 Introduction

Wharf structures are one of the primary elements of the transportation sector and are associated with the expansion of the global economy (Dwakarish, 2015). Moreover, they can play a strategic role in a nation's defense (Hanson, 2013). These structures primarily serve to dock commercial and military ships for the loading and unloading of passengers, personnel or cargo. However, a wide range of services including repairs, berthing and storage can be performed in wharves. These structures often consist of a reinforced concrete superstructure supported on steel or reinforced concrete pilings, and may also include sheet and battered steel piles. Because of their importance, they are subject to periodic evaluation and maintenance.

The main characteristics of the USS Salem Wharf and a review of background literature on the evaluation of similar structures are presented in this chapter.

2.2 Description of the USS Salem Wharf Structure

This wharf was built in 1959 and is located in Quincy, MA. The owner of the site at the time, Bethlehem Steel Corporation, undertook the project to expand its shipbuilding facilities in the Fore River Shipyard, and the wharf was used to assist in various shipbuilding activities (P. Schuman, personal communication, 2016). In 1994, the USS Salem was brought and moored to the wharf. According to the United States Naval Shipbuilding Museum (2016), the USS Salem is currently an approximately 700 ft. long non-operational former US Navy heavy cruiser serving as a permanently moored museum. The ship was also used to house students, boy and girl scouts, and other large groups on extended overnight stays after it became non-operational. Originally, a moving crane used for shipbuilding was located on the superstructure of the wharf. After the crane was removed, the acting gravitational loads were considerably lower. Due to the failure of the adjacent sea wall, the owner of the site requested an assessment of the wharf condition and possible repair recommendations. Simpson Gumpertz & Heger, Inc. (SGH) and their sub-consultant, Appledore Marine Engineering, Inc. (AMEI), were tasked with performing these inspections. The general orientation of the USS Salem Wharf and its surroundings are depicted in Figure 2.1. Structural drawings were provided by SGH and are presented in Figure 2.2 to Figure 2.4.

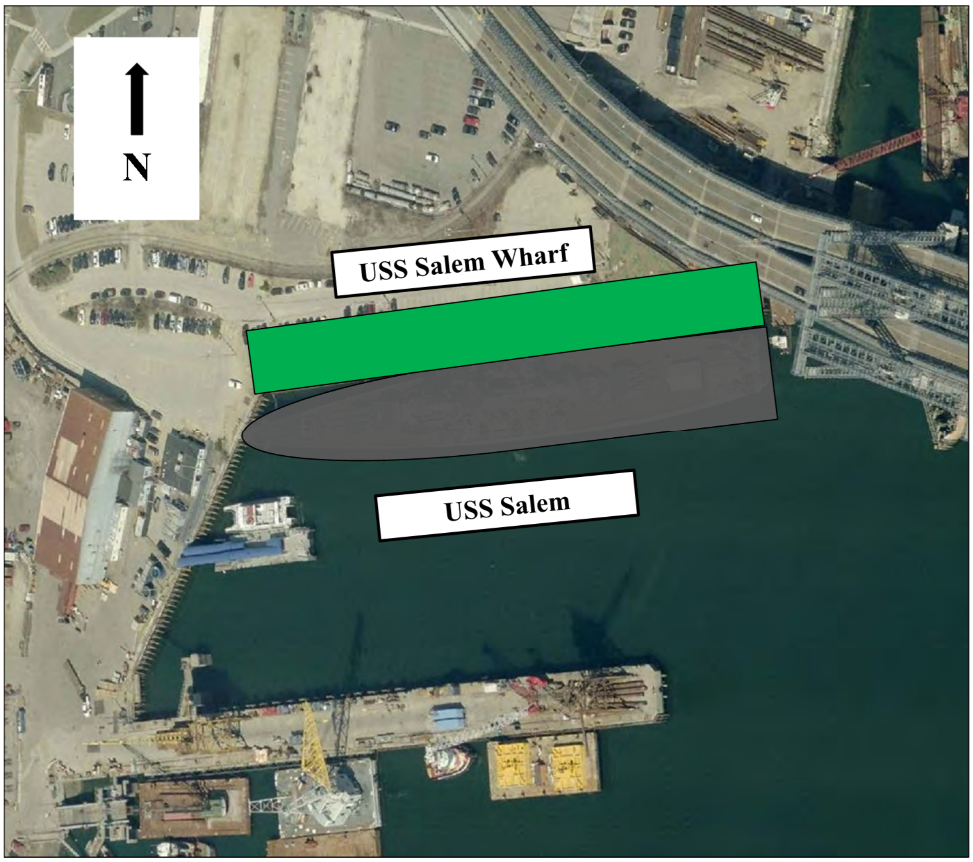

Figure 2.1- USS Salem Wharf orientation (P. Schuman, personal communication, 2016)

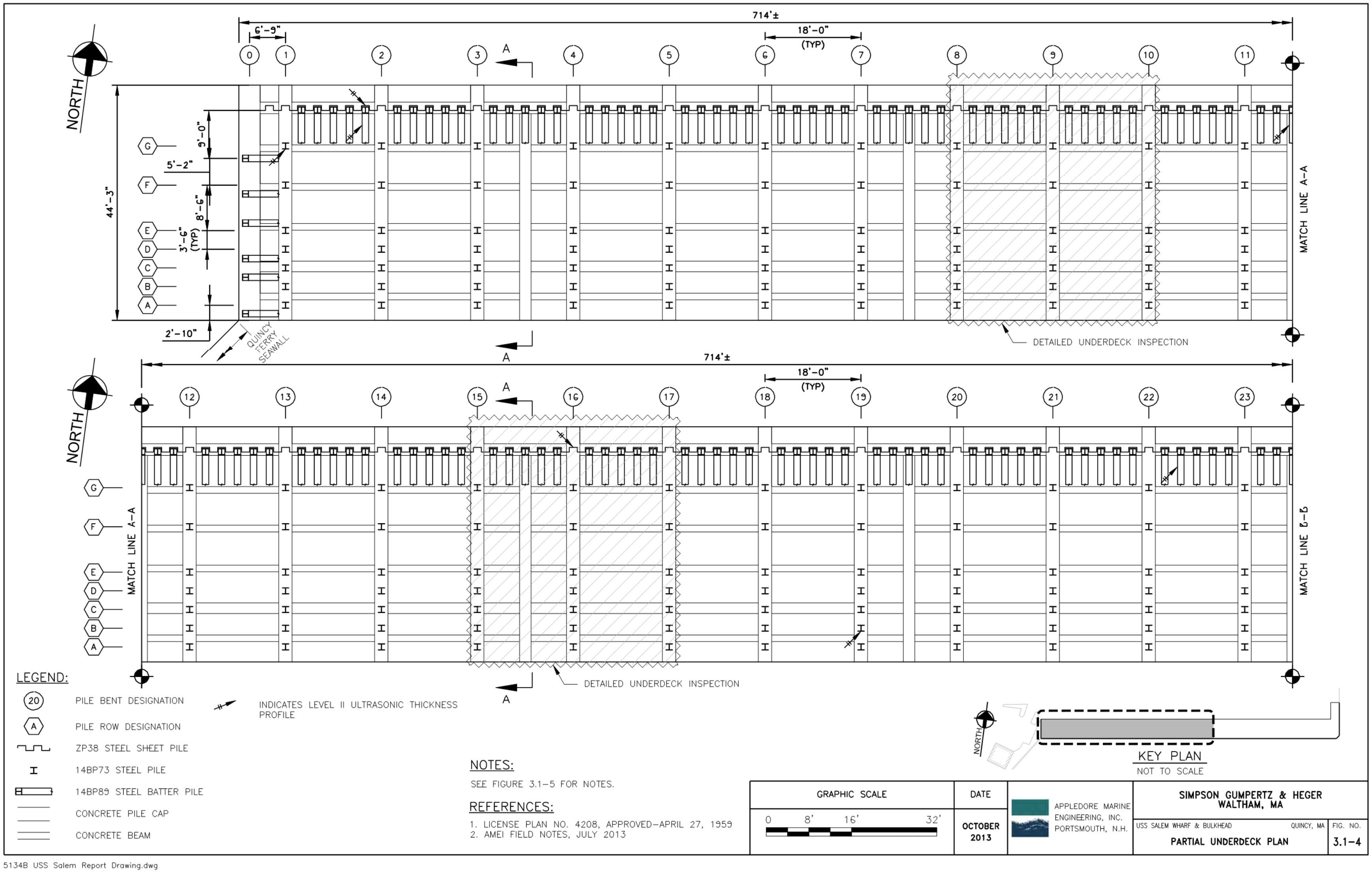

Figure 2.2- USS Salem Wharf bents 0 to 23 (P. Schuman, personal communication, 2016)

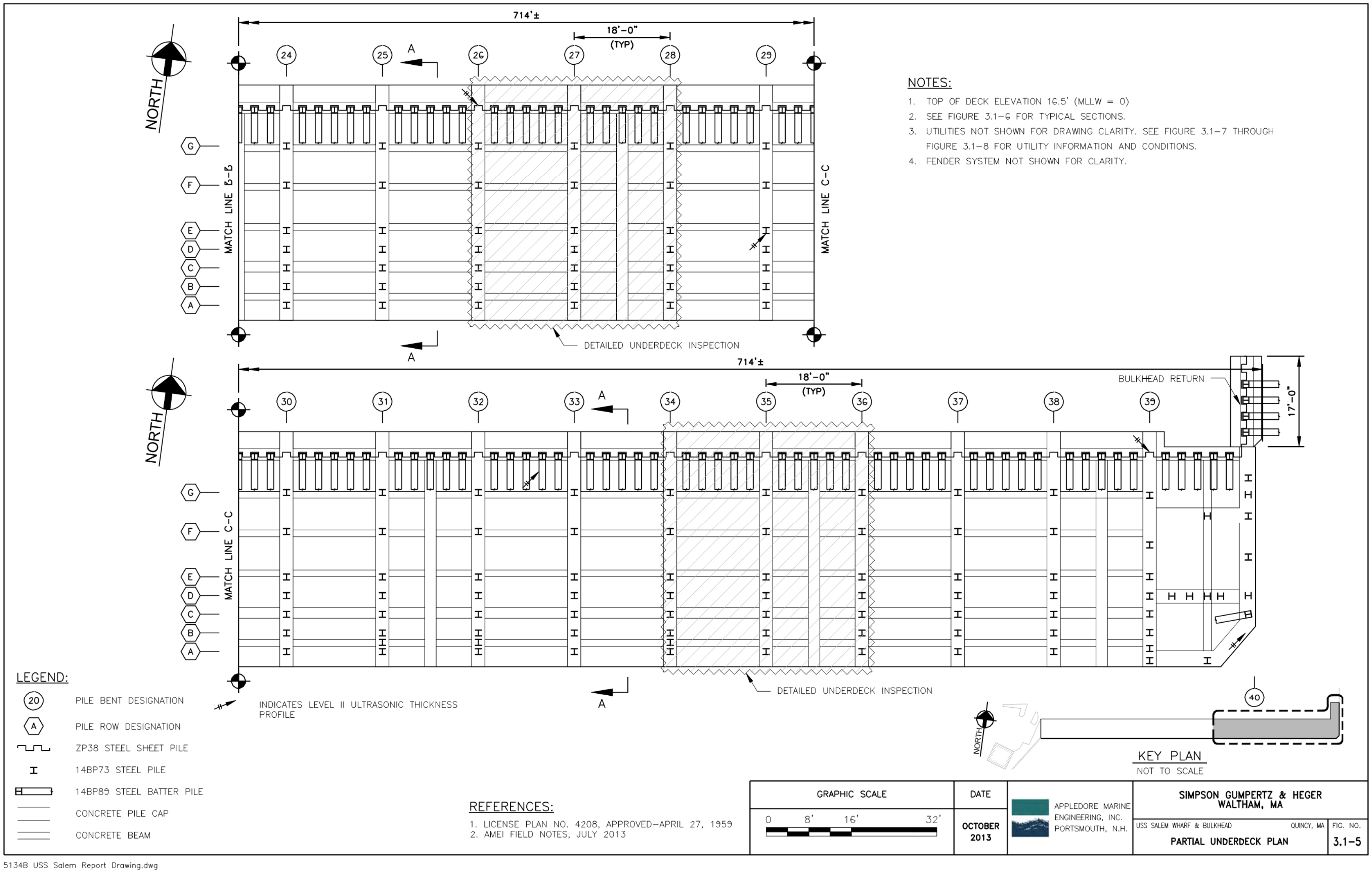

Figure 2.3- USS Salem Wharf bents 24 to 40 (P. Schuman, personal communication, 2016)

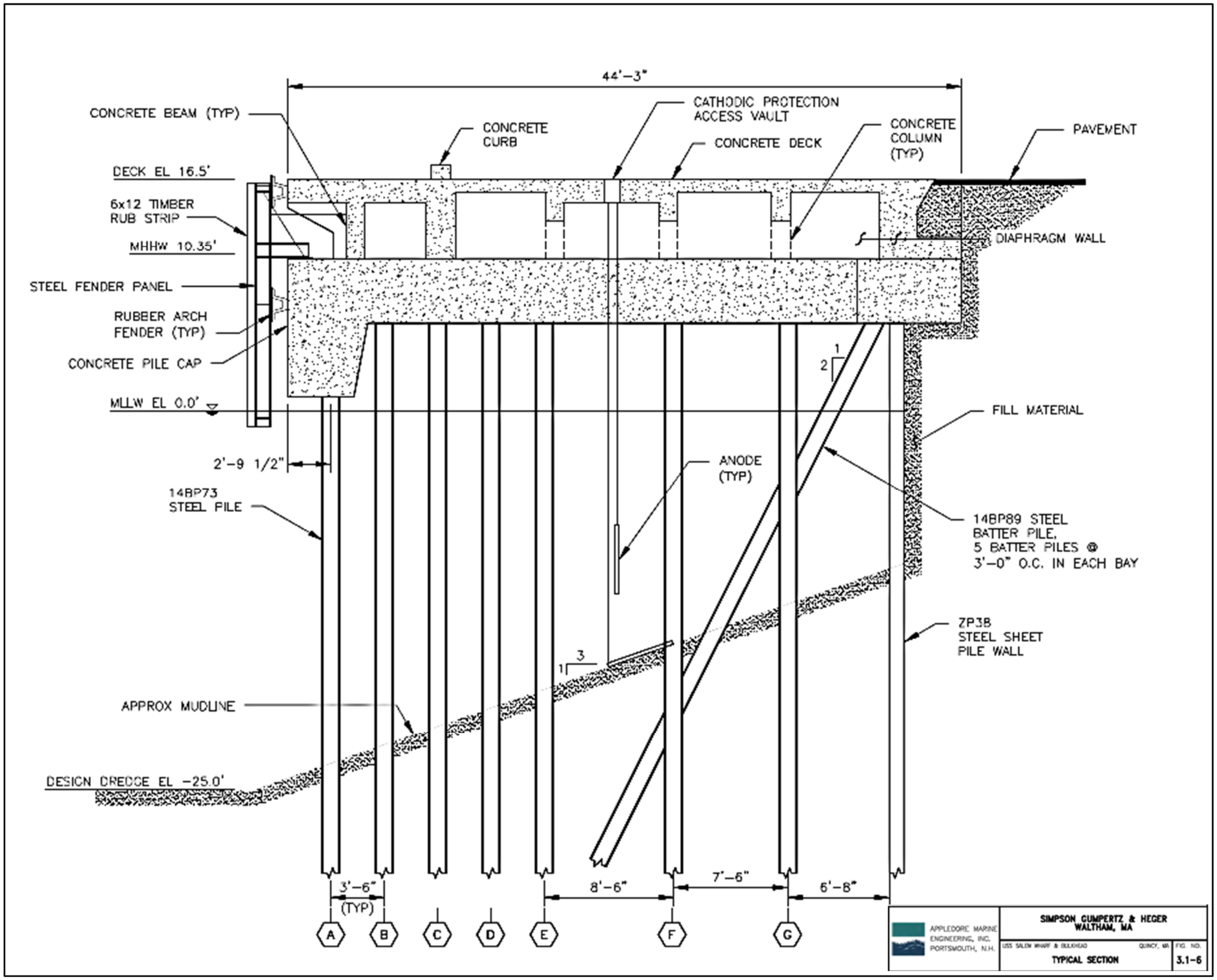

Figure 2.4- USS Salem Wharf typical section (P. Schuman, personal communication, 2016)

The wharf is approximately 710 ft. long by 45 ft. wide. The concrete superstructure of the wharf consists of a slab, supported by beams, which span east-west. The beam ends are supported on concrete bent caps. Each bent cap is supported on 7 vertical steel piles. There are 40 bents spaced at 18 ft. on center. The longitudinal reference axes, spanning east-to-west are labeled A through G and are defined by the locations of the pile lines; the transverse reference axes, spanning north-to-south are defined by the locations of the bent caps. These reference axes were used to identify the piles. In this way, a pile on the intersection of axis A and 1 was identified as Pile A1 for the purposes of the current investigation. Between bents, there are battered piles spaced at 36 ft. on center intended for lateral bracing of the structure and connected to the cap beam of the bulkhead. The bent caps are perpendicular to but integral with the cap beam of the bulkhead wall at their northern ends.

Several steel mooring bollards are tied to ropes and chains from the USS Salem. The bent cap directly below each bollard has a concrete haunch at its end. The typical haunch is presented in Figure 2.5 as documented by AMEI, and a schematic of its dimensions is presented in Figure 2.6.

Figure 2.5- Typical haunch – North view (P. Schuman, personal communication, 2016)

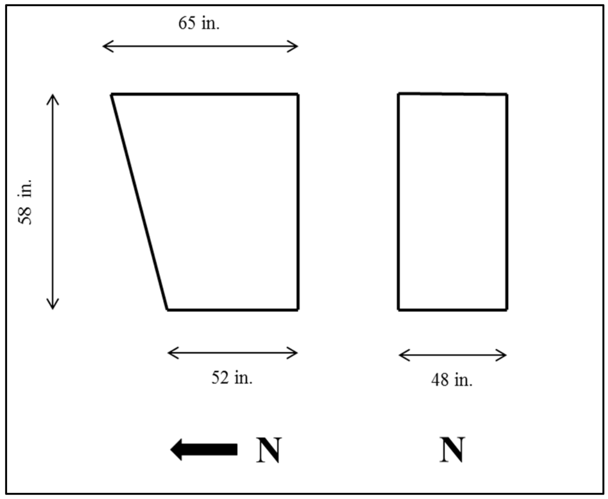

Figure 2.6- Typical haunch dimensions

As discussed in Chapter 1, the primary safety concern of the inspectors was related to the extent of corrosion in the vertical steel piles. As such, substructure collapse stemming from axial loads on these piles was considered the critical failure mode. The condition of the vertical piles as inspected by the AMEI diving teams is depicted in Figure 2.7.

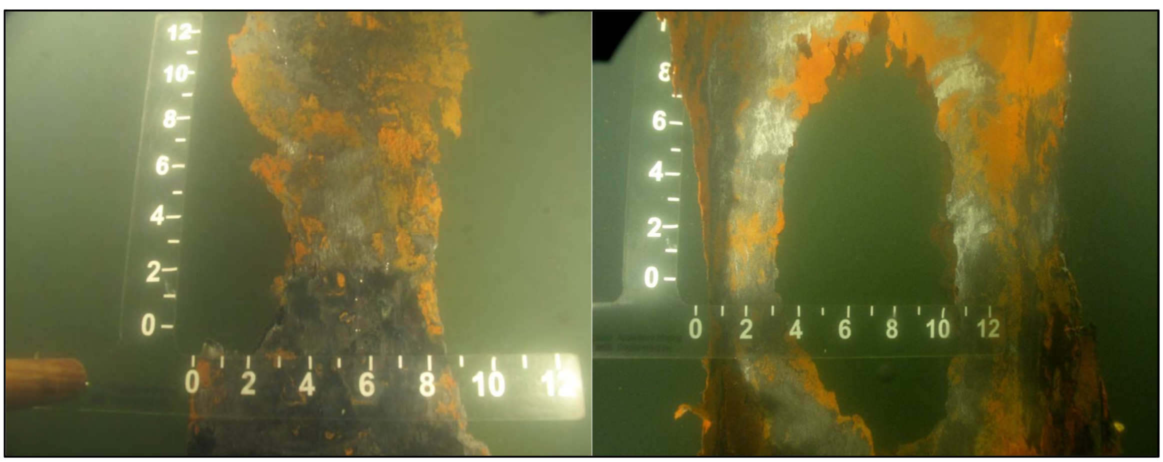

Figure 2.7- Condition of vertical piles (P. Schuman, personal communication, 2016)

Shi, et al. (2015) developed a numerical model to analyze the inelastic buckling behavior of steel piles with localized severe corrosion. The findings of this study showed that the current code provisions by the American Association of State Highway Officials (AASHTO, 2012), American Institute of Steel Construction (AISC, 2011) and American Iron and Steel Institute

(AISI, 2012) do not provide accurate predictions of the peak capacity of severely corroded piles. Moreover, this numerical framework was validated by experimental tests. As such, it was used to model the vertical piles of the USS Salem Wharf, shown in Figure 2.7.

Finally, a comprehensive underdeck photograph, provided by AMEI, of a typical span that includes the slab, bent caps, cap beam, longitudinal beams, vertical piles, battered piles and sheet piling is presented in Figure 2.8.

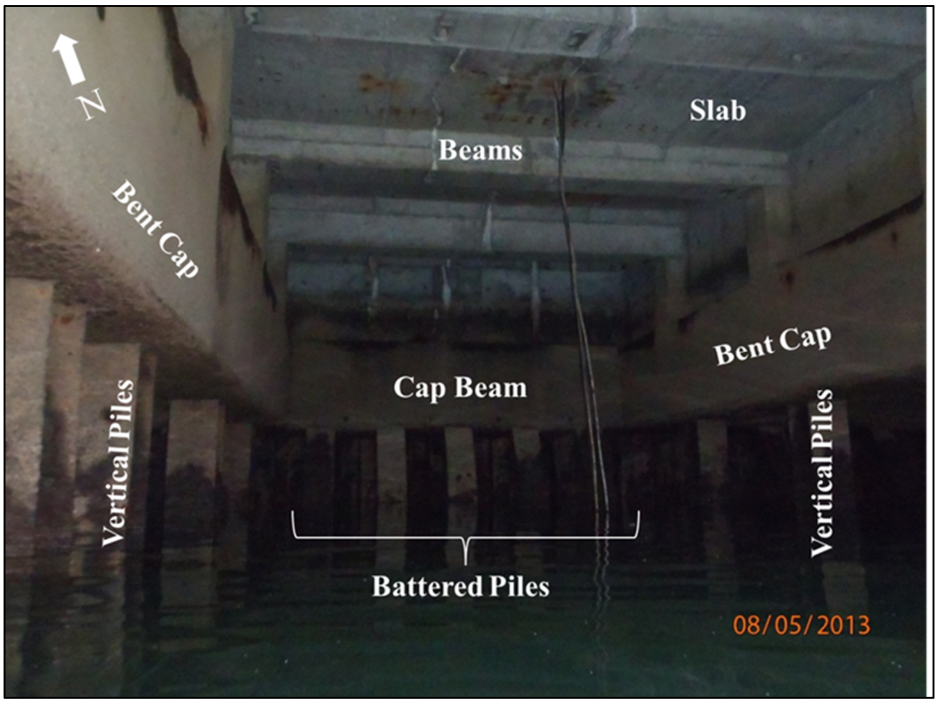

Figure 2.8- Typical underdeck configuration (P. Schuman, personal communication, 2016)

The elements depicted in Figure 2.8 were idealized and included in a non-linear finite element model in order to study the behavior and performance of the USS Salem Wharf under gravitational loads.

The existing literature pertaining to the behavior of wharf structures is predominantly focused on their performance under seismic or other types of lateral loads. This was considered a consequence of the significance of lateral loads in cases where the ship is in service. However, it was found that there is little guidance with regards to the behavior of wharves for which axial loads on the substructure are primary concerns, as is the case for the USS Salem Wharf. As such, the modeling approach used in developing the numerical framework presented in this research is not only applicable for the analysis of this wharf, but represents a technique that can be implemented by engineers to analyze similar structures.

2.3 Evaluation of Pile-Supported Marine Structures

According to the New South Wales Transport Roads and Maritime Services Guideline for Evaluation of Public Ferry Wharf Safety (2015), if a wharf structure has deteriorated, or the original design loading conditions are unknown, structural analysis should be undertaken to determine a wharf's structural capacity and to confirm the wharf's load limitations. Generally, this analysis would be comprised of a determination of the vertical live load capacity of the wharf, its lateral load capacity and loading from design vessel type and velocity. Researchers have investigated these conditions in order to develop evaluation criteria that are specific to particular wharf structures and methods that can be used for general assessments.

Bhattacharya, et al. (2008) investigated the principal mechanics of failure of pile-supported structures. These failure mechanisms include shear failure of the piles due to lateral loads, bending failure due to lateral spreading of the ground and buckling instability due to the effect of axial loads acting on the vertical piles.

In characterizing vertical pile elements for a study on the seismic dynamic damage characteristics of pile-supported wharf structures, Jiren, et al. (2015) used plastic hinges to assign the piles an elasto-plastic behavior. In this study, non-linear time history analyses were used to compare the damage characteristics found for vertical and battered pile-supported wharves under the same geographical and environmental conditions. The results of this study showed that for peak ground acceleration (PGA) of 3.56g, the performance of the battered pile structure compared favorably to that of the vertical pile structure. For a PGA of 1.02, the vertical pile structure displayed more favorable behavior.

Heidari-Torkamany, et al. (2014) also used the plastic hinges approach in developing a numerical framework to study the generation of seismic fragility curves with regards to three engineering demand parameters (EDPs), displacement ductility factor, differential settlements and residual horizontal displacements. In this study, incremental dynamic analysis (IDA) was used to estimate the seismic demand quantities. The findings indicated that the uncertainties associated with the porosity of the soil contributed most to the variance in the normalized horizontal displacements and displacement ductility factor, while the friction angle was a prominent factor in the variance of differential settlements.

However, substructure instability was not considered as a prominent failure mode in these studies. Because the representation of progressive collapse of the substructure required that the softening behavior induced by buckling of piles be incorporated, the axial load-shortening relationships of the vertical piles of the USS Salem Wharf were used in the definition of non-linear connector elements that were included in the numerical framework presented in this thesis.

To analyze the response of a pile-supported wharf structure to lateral loads for the development of fragility curves through numerical analysis, Chiou, et al. (2011) modeled the reinforced concrete deck of the wharf using shell elements. Similarly, for the seismic vulnerability assessment of another pile-supported wharf, Banayan-Kermani, et al. (2016) also adopted shell elements for modeling a concrete superstructure. These studies were not directed at the rigorous representation of substructure collapse. However, they provided guidance in their approach for the numerical modeling of the superstructure of wharves.

For the failure analysis of the Minneapolis I-35W Bridge, the National Transportation Safety Board (NTSB) enlisted the support of the Federal Highway Administration (FHWA), the State University of New York, and SIMULIA. In this study, Schultheisz, et al. (2008) developed a global finite element model of the complete bridge structure, as well as a local model to study the stresses on some of the bridges' gusset plates, as their failure was initially considered a principal factor in the structure’s collapse. For this analysis, the Riks method was used to evaluate the unstable collapse characteristics. Within this solution method, loads and displacements are solved for simultaneously and using an arc length formulation. In this way, it can handle localized or global softening stemming from instabilities of the structure. Furthermore, an independent peer review of this analysis conducted by Sandia National Laboratories (SANDIA) validated its approach, results and conclusions (Gwinn, et al., 2008). As such, in the current investigation of the USS Salem Wharf, Riks analysis method was adopted for the determination of the collapse live load of the structure.

Chapter 3 : Numerical Study of Corroded H-Piles

3.1 Introduction

Preliminary inspections of the USS Salem Wharf performed by SGH and AMEI indicated that the steel elements of the wharf's substructure had been significantly corroded. Moreover, because the vertical steel piles were considered primary supporting elements, instability of the substructure stemming from axial loads was deemed a likely critical failure mode, and primary focus was placed on their assessment.

Simpson, Gumpertz & Heger, Inc. (SGH) were contracted to conduct a visual inspection of the conditions of the vertical piles. After inspecting half of the wharf substructure, the corrosion damage in the piles was such that the procedures were halted in order to preserve the safety of the inspectors. This reinforced the notion of axial collapse of the substructure as a primary concern. As such, the gathered data was used to create a modeling matrix grouping piles with similar geometrical characteristics for their structural analysis.

The design specifications for the determination of axial capacity of compressive members, presented in Appendix F, require that cross-section degradation be assumed uniform along the length of the column. That is, the design equations are only applicable to prismatic members. As has been found in previous research, and based on the results of inspections of the wharf, corrosion of steel members is often localized, in which case, the code-based estimations may be considerably conservative. Moreover, the complete axial load-shortening behavior data of the corroded piles was a necessary input to the analysis of the complete wharf structure. As such, SGH conducted an assessment of cross-sectional conditions of the vertical steel piles, since these are the primary supporting elements of the structure. Consequently, the modeling techniques developed by Shi, et al. (2015) were implemented in ABAQUS v6.12 (SIMULIA, 2012) to generate axial load-shortening relationships for the individual piles. These axial load-shortening curves were idealized using non-linear connector elements and included in a numerical framework developed to evaluate the performance of the wharf under gravitational loads.

The field inspection data, numerical modeling results, and comparison to code-based calculations are presented in this chapter.

3.2 Pile Analysis Matrix

In this section, the data collected from the field inspections, the criteria for establishing the groups of piles for analysis, and the final pile modeling data are presented.

3.2.1 Field Data of Piles

As the effects of corrosion are amplified by the wetting-drying cycle of the piles, the inspection team was interested in measuring the cross-sectional dimensions in the severely corroded region. That is, the region defined by the high-water-mark and the low-water-mark for each pile. Illustrations of the cross-sectional and pile-length measurements are presented in Figure 3.1.

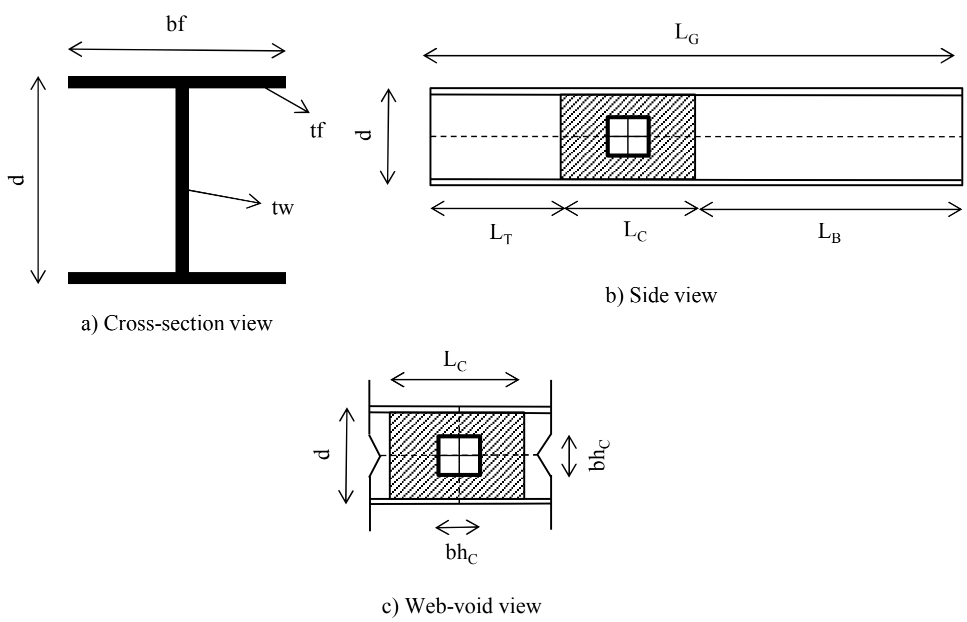

Figure 3.1- Pile dimensions

The reference axes of the structure were used to define the pile identifications. Accordingly, a pile at the intersection of longitudinal axis 'A', with transverse axis '1', is referred to as pile 'A1' herein. In this structure, longitudinal reference axes range from A to G, and transverse reference axes range from 1 to 40. Inspection of the piles was only performed for bents 1 through 20. As such, pile dimensions were obtained for piles A1 through G20. The corresponding pile dimensions are presented in Appendix A. As shown in this appendix, some piles have been modeled with square void located at the centroid of the web of the corroded region, as indicated in Figure 3.1. This represents an idealization of the voids found in the inspection, which were typically round. For reference, the pile dimensions for pile-row 1, comprised of piles A1 to G1 (seven piles) are presented in Table 3.1. Note that none of the piles presented in this table have haunches or web voids.

Table 3.1- Field inspection geometry data for pile-row 1

Pile	Length Measurements (in.)				Measurements of Remaining Section at Severely Corroded Region (in.)				
	Total Length (L_G)	Top Length (L_T)	Bottom Length (L_B)	Corroded Length (L_C)	Flange Thickness (tf_c)	Flange Width (bf_c)	Web Thickness (tw_c)	Depth (d)	Web Void Width (bh_c)
A1	438	81.0	339	18.0	0.150	4.60	0.230	13.3	N/A
B1	426	81.0	327	18.0	0.170	12.6	0.230	13.3	N/A
C1	408	81.0	309	18.0	0.205	14.6	0.250	13.3	N/A
D1	396	81.0	297	18.0	0.120	12.6	0.270	13.2	N/A
E1	378	81.0	279	18.0	0.200	14.6	0.260	13.3	N/A
F1	342	81.0	243	18.0	0.170	14.6	0.295	13.3	N/A
G1	318	81.0	219	18.0	0.165	14.6	0.285	13.3	N/A

The global lengths reported in Table 3.1 represent the equivalent unbraced lengths of the piles. These account for the minimum embedment length at which the pile could be considered fixed at its bottom according to Davisson, et al. (1965). The procedure used in calculating the effective lengths of the piles from the clear-length measurements performed in the inspections is presented in Appendix B.

The cross-section above and below the severely corroded region was considered to be un-corroded, and the assigned dimensions were those of the HP14×73 profile: $t_f = 0.250$ in., $b_f = 14.6$ in., $t_w = 0.250$ in. and $d = 13.4$ in.

3.2.2 Pile Analysis Data

The piles were modeled using three characteristic parts. These represented the top, corroded and bottom parts of the piles. In order to minimize the number of parts that were modeled, piles with similar geometries were grouped. As such, individual parts were modeled as outlined in Table 3.2.

Table 3.2- Generalized dimensions for modeling

Region	Measured Length (in.)	Modeled Length (in.)	Measured Width (in.)	Modeled Width (in.)
Top (L_G, bf)	23.0	23.0	14.6	14.6
	23.0-81.0	81.0		
Corroded (L_C, bf_C)	18.0-60.0	18.0-60.0	0.600-14.6	0.600-14.6
Bottom (L_B, bf)	213-219	220	14.6	14.6
	234-243	245		
	267-279	280		
	288-297	300		
	300-309	310		
	324-339	340		

Moreover, each of the modeled piles was assigned a modeling code as outlined in Table 3.3. The pile modeling code is comprised of three parts. These refer to the dimensions of the top, corroded and bottom regions, and are defined as follows:

- Ta: here, 'T' indicates that this part of the code refers to the top region of the pile, and 'a' represents the length of the top region. As such, if a = 1, L_B = 23.0 in.; and if a = 2, L_B = 81.0 in.
- Cxy: here, 'C' indicates that this part of the code refers to the corroded region of the pile, while 'x' and 'y' represent the length and width of the corroded region, respectively. The possible values for 'x' and 'y', and their corresponding dimensions are presented in Table 3.3.
- Bz: here, 'B' indicates that this part of the code refers to the bottom region of the pile, and 'z' represents the length of the bottom region. The possible values for 'z' and the corresponding lengths are presented in Table 3.3.

Table 3.3- Pile model identification code

T**a** = Top length

C**xy** = Corroded region; x for length; y for width

B**z** = Bottom length

General Pile Model Code

T**a**C**xy**B**z**

	1	2	3	4	5	6	7	8	9	10
a	23.0''	81.0''								
x	18.0"	20.0"	24.0"	30.0"	36.0"	42.0"	60.0"			
y	0.600"	2.60"	4.60"	6.60"	8.60"	10.6"	11.6"	12.6"	13.6"	14.6"
z	220"	245"	280''	300"	310"	340"				

While the modeling code could be repeated among different piles, the different flange and web thicknesses at the corroded region were unique. In these cases, several simulations were run for the same model, where the flange and web thicknesses at the corroded region were adjusted to accurately reflect the geometry of each pile. The final modeling information is presented for pile-row 1, comprised of pile A1 to G1 is presented in Table 3.4. This information is presented for all the modeled piles in Appendix C.

Table 3.4- Pile model identifiers and geometry data for modeling

Pile ID	Pile Model Code	Characteristic Lengths (in.)				Severe Corrosion Area Modeling Information (in.)				
		L_C	L_T	L_B	L_G	Flange Thickness (tf_C)	Flange Width (bf_C)	Web Thickness (tw_C)	Depth (d)	Web Void Width (bh_c)
A1	T2C13B6	18.0	81.0	340	439	0.150	4.60	0.230	13.3	N/A
B1	T2C18B6	18.0	81.0	340	439	0.170	12.6	0.230	13.3	N/A
C1	T2C110B5	18.0	81.0	310	409	0.205	14.6	0.250	13.3	N/A
D1	T2C18B4	18.0	81.0	300	399	0.120	12.6	0.270	13.2	N/A
E1	T2C110B3	18.0	81.0	280	379	0.200	14.6	0.260	13.3	N/A
F1	T2C110B2	18.0	81.0	245	344	0.170	14.6	0.295	13.3	N/A
G1	T2C110B1	18.0	81.0	220	319	0.165	14.6	0.285	13.3	N/A

The geometrical information presented in this section, Appendix A and Appendix C was used in the implementation of finite element analysis (FEA) models in order to determine the remaining capacity of the corroded piles and to assess their overall load-shortening response.

3.3 Description of the Finite Element Model

The numerical framework developed by Shi, et al. (2015) for the study of corroded steel H-piles was implemented utilizing the commercial finite element analysis software ABAQUS v6.12 (SIMULIA, 2012). In these models, an initial eigenvalue analysis (linear perturbation/buckle step) was performed in order to determine the elastic buckling loads and failure modes. These results were used as deformation patterns that represent the global and local imperfections of the element. Then, a displacement-controlled inelastic buckling analysis (static-Riks step) was performed to obtain the buckling and post-buckling response of each pile, while accounting for the effects of geometric imperfections and residual stresses.

3.3.1 Boundary Conditions and Loads

An illustration of the unrestrained degrees of freedom and prescribed load and displacements for the elastic buckling and inelastic buckling analyses, is presented in Figure 3.2.

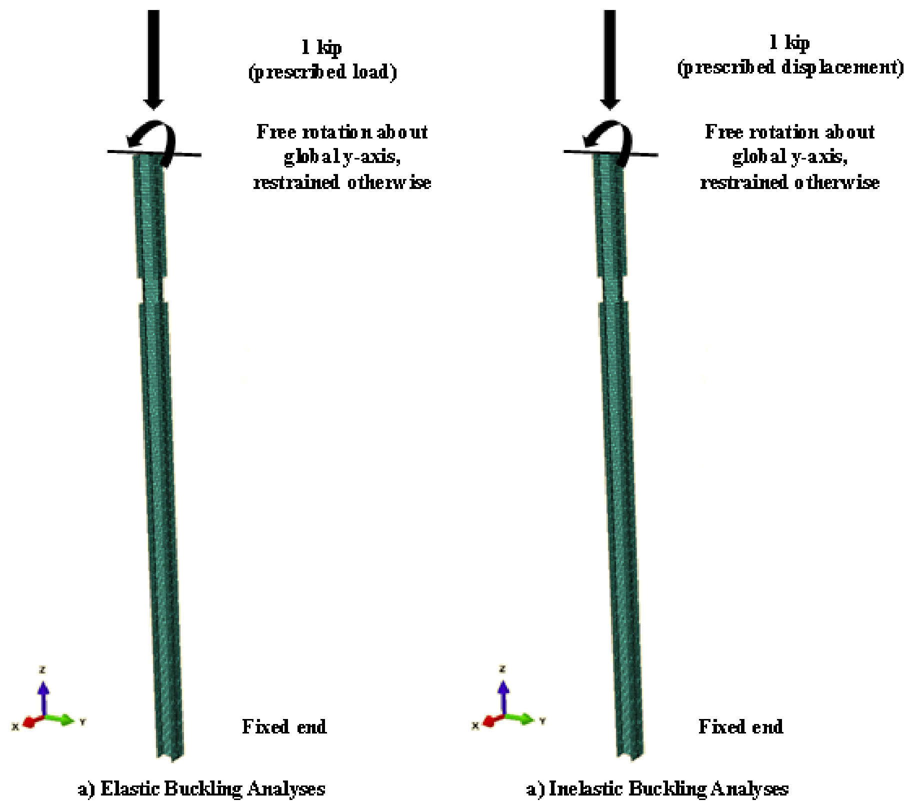

Figure 3.2- Unrestrained DOF in elastic buckling analyses

As shown in the previous figures, the bottom displacements and rotations were restrained (prescribed as zero) in all global directions, for both elastic and inelastic buckling analyses. The top displacements in the X and Z directions, and rotations about global-X and global-Z axes were restrained for both types of analysis, while rotations about the global-Y axis were free in both instances. Finally, in elastic buckling analysis, a prescribed loading of 1 kip was applied at the top end of the pile in the negative global-Z direction, while in inelastic buckling analysis a prescribed displacement of 1 in. was applied in the same direction.

3.3.2 Material Properties

The conditions of the structure at the time of inspection did not allow for material samples from the vertical piles to be taken for testing. Consequently, the mechanical properties of the HP14×73 vertical piles were conservatively taken as summarized in Table 3.5, based on the AISC Design Guide 15 (Brockenbrough, 2003), which indicated that ASTM A7 was the most common grade of steel for structural steel sections at the time the USS Salem Wharf was constructed. The steel was modeled in ABAQUS as an elastic-plastic material with strain hardening. Figure 3.3 presents the uniaxial stress-strain diagram that was implemented for the steel.

Table 3.5- Steel H-pile mechanical properties

Modulus of Elasticity	**Yield Strength**	**Yield Strain**	**Ultimate Strength**	**Ultimate Strain**
E (ksi)	Fy (ksi)	εy	Fu (ksi)	εu
29000	33	0.0011	60	0.15

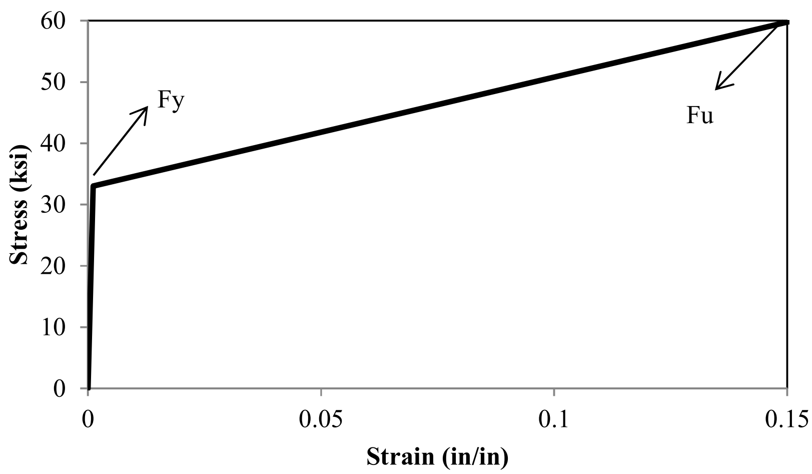

Figure 3.3- Steel H-pile material constitutive relationship

3.3.3 Residual Stresses

The distribution and magnitude of residual stresses recommended by Seif, et al. (2009) were adopted in this study. These stresses were input as initial conditions on the non-linear finite element model, and are shown in Figure 3.4.

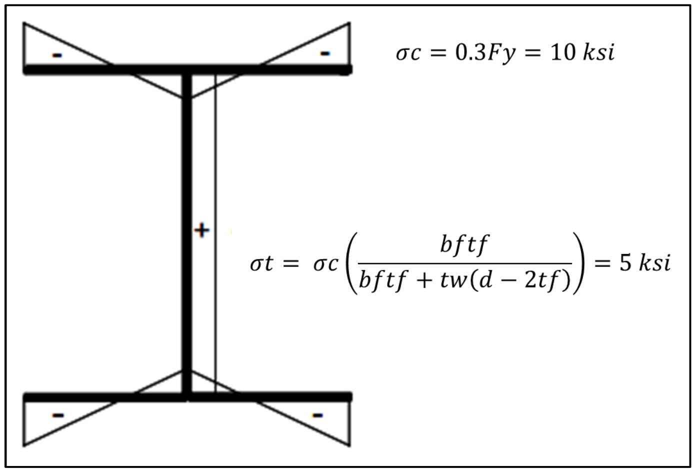

Figure 3.4- Distribution and magnitude of residual stresses on steel H-piles

3.3.4 Global and Local Imperfections

The effects of global and local imperfections were represented by scaling the deformation patterns associated with the global and local elastic buckling modes of the piles, respectively. For an axially loaded member, the magnitude of the initial out-of-straightness is L/1000 and L/1500, as recommended by AISC (2011) and AASHTO (2012), respectively. However, some researchers have found that the values for initial out-of-straightness are lower. According to Bjorhovde (1972), the average initial out-of-straightness for hot-rolled W-shapes is L/1470, while Essa, et al. (1993) give mean values of initial out-of-straightness of L/2000 and L/3300 for W-shapes with lengths of 240 and 396 in., respectively. Moreover, Shi, et al. (2014) conducted a parametric study that included the analysis of the effect of the initial out-of-straightness on the peak capacity of piles with severe localized corrosion. This study used a range of the initial out-of-straightness of L/1500 to L/480, and the findings indicated that this parameter had negligible effects on the capacity and behavior of the piles. The modeled length of the piles analyzed in this study ranged from 319 in. to 445 in. The assumed length for calculating the maximum initial out-of-straightness was 450 in. This length and an initial out-of-straightness limitation of L/1500 were applied in determining a peak initial out-of-straightness of 0.3 in, which was used to scale the global buckling deformation pattern obtained from eigenvalue analysis. A sample global buckling mode used as a deformation pattern for global imperfections is presented in Figure 3.5.

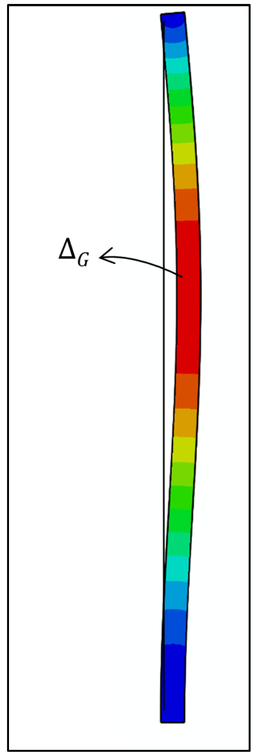

Figure 3.5- Elastic buckling mode for global imperfection

Initial local imperfections were incorporated by scaling the local buckling modes obtained from eigenvalue analysis. The peak local deformation was taken to be one tenth of the flange thickness, as suggested by Chan, et al. (2008). This resulted in a peak value of 0.025 in. A sample local buckling mode used as a deformation pattern for local imperfections is presented in Figure 3.6.

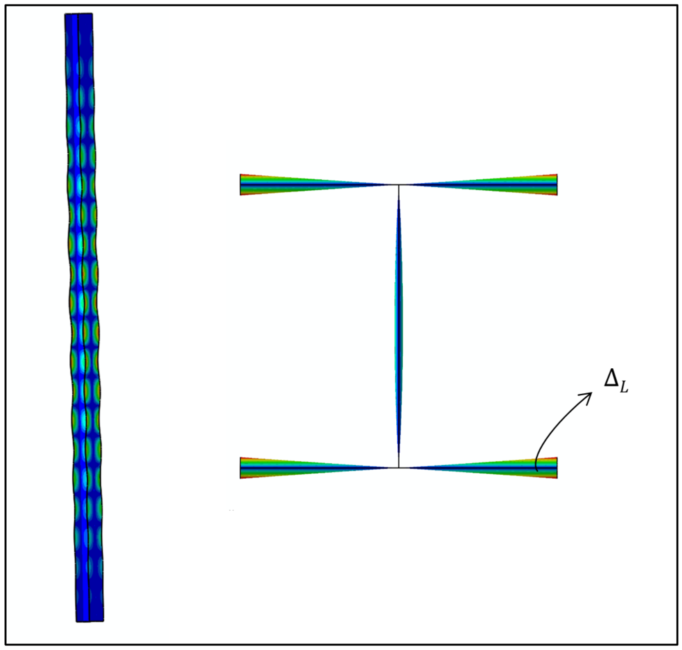

Figure 3.6- Elastic buckling mode for local imperfection

3.3.5 Element Types and Mesh Size

The general-purpose 4-node, 6 degrees of freedom per node, finite-membrane-strain element with reduced integration (S4R) was used for modeling the inelastic buckling behavior of steel H-piles in this study. While there is debate in the research community regarding the use of S4R, S4 and S8R elements, all have been used to model similar problems (Seif, et al., 2009). The primary reason for selecting S4R elements was the reduced computational time required by S4R models reported by Earls (2001).

Approximate mesh sizes of 4 in. x 4 in., 2 in. x 2 in. and 1 in. x 1 in., were implemented for the analysis of pile A1, in order to estimate the mesh sensitivity of the model and arrive at a mesh size that rendered satisfactory convergence and computational time. Since Pile A1 exhibited nearly 60% section loss in the corroded region, it was selected as an adequate case of study for inelastic buckling behavior with severe localized corrosion. Table 3.6 presents the total number of elements, nodes and computational time in seconds per processor core required to run each model on a desktop PC with an Intel Core 2 central processing unit (CPU) with an installed memory

(RAM) of 5.00 GB and a 64 bit operating system. The results of the mesh sensitivity analysis are plotted in Figure 3.7.

Table 3.6- Model characteristics for different mesh sizes

Mesh size	Element Type	No. of Nodes	No. of Elements	CPU time (s)
4 x 4	S4R	2190	2050	46
2 x 2	S4R	5242	4988	155
1 x 1	S4R	18142	17639	733

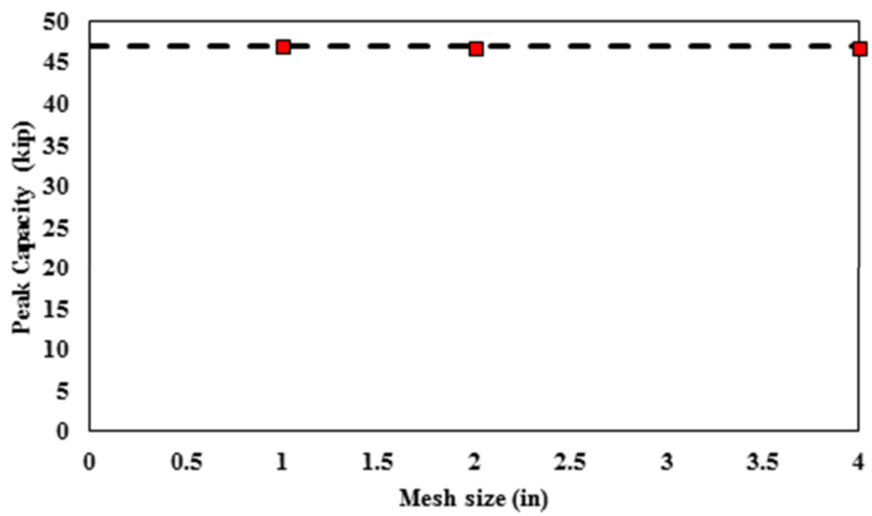

Figure 3.7- Mesh sensitivity analysis for steel H-piles

Since it rendered satisfactory convergence and computational times, a mesh size of 2 in. x 2 in. was selected for the analysis of steel H-piles in this study.

3.4 Pile Analyses Results

In this section, the load-shortening curves, deformed shapes and stress contours are presented for sample piles with varying dimensions and corrosion patterns, in order to assess the different failure modes found in the analysis of 140 vertical piles. The axial load-shortening curves for all the analyzed piles are presented in Appendix D. Additionally, correlation studies on the influence of area reduction at the severely corroded region and global length over pile capacity and elastic stiffness are presented herein.

The maximum capacity determined by finite element analysis is 244 kips, while the weakest pile showed a peak load of 1.94 kips. Moreover, the highest area loss in the 140 analyzed piles was 90%, and the lowest 36%. Lastly, the longest of the analyzed piles had an effective length of 445 in., while the shortest had an effective length of 319 in.

To represent the wide range of configurations, long and short piles with high and low percentages of area loss were selected for the specific analyses presented in this chapter. Table 3.7 lists the sample piles whose responses are specifically analyzed, along with their global length, percentage area loss, capacity and failure mode.

Table 3.7- Sample pile results

Pile ID	Area Loss (%)	L_G (in)	Capacity (kips) FEA	AISC	AISI-EWM	AISI-DSM	Failure Mode (FEA)
B4	86	445	26.0	4.00	4.00	4.00	FB[a]
B14	36	439	224	171	214	209	FLB[a]/GB
G3	46	319	244	200	262	250	FLB[a]/GB
G18	79	325	87.0	48.0	53.0	53.0	FLB[a]/GB

[a] Flange one-way bending
[b] Flange local buckling
[b] Global buckling

This table indicates that piles with different lengths could reach similar peak capacities. Additionally, it shows that piles that were close in length could have vastly different peak capacities. Moreover, for the piles in Table 3.7, code provisions rendered conservative estimations of peak capacity with respect to the values obtained through finite element analysis, with the exception of the analysis of pile G3, for which the AISI methods estimated slightly higher peak loads than finite element analysis. This was ascribed to the relatively low level of corrosion of this pile as compared to the others analyzed in this study. Additionally, the difference in estimations of peak capacity based on code provisions and those stemming from finite element analysis became larger for the cases of higher percentage area loss, as code provisions are based on the assumption of prismatic elements, and their precision was affected by the severity of damage of the corroded region. A comparison of the values obtained through finite element analysis and existing code provisions is presented in Appendix G. The axial load-shortening curve for pile B4 is presented in Figure 3.8. Its deformed shape and stress contours at different load levels are presented in Figure 3.9.

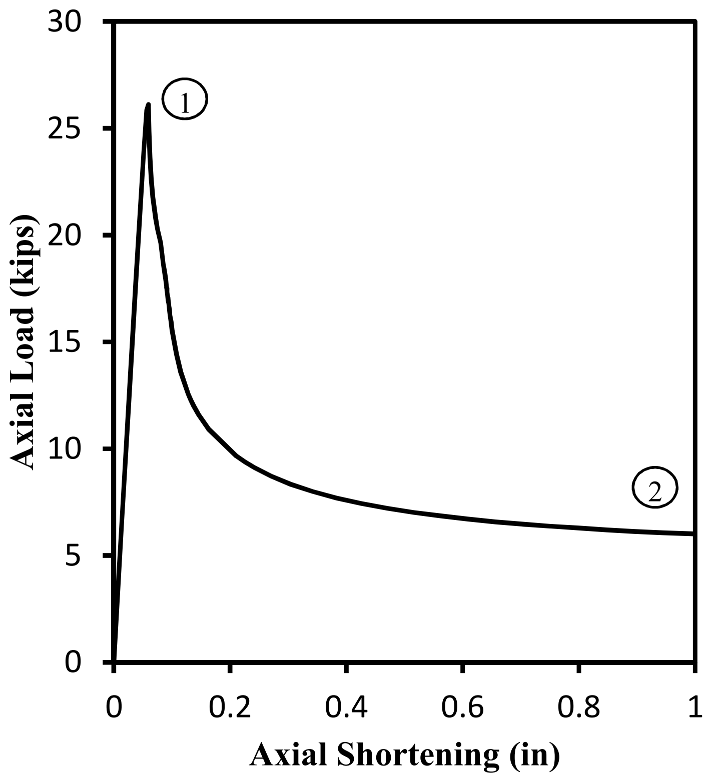

Figure 3.8- Axial load-shortening curve for pile B4

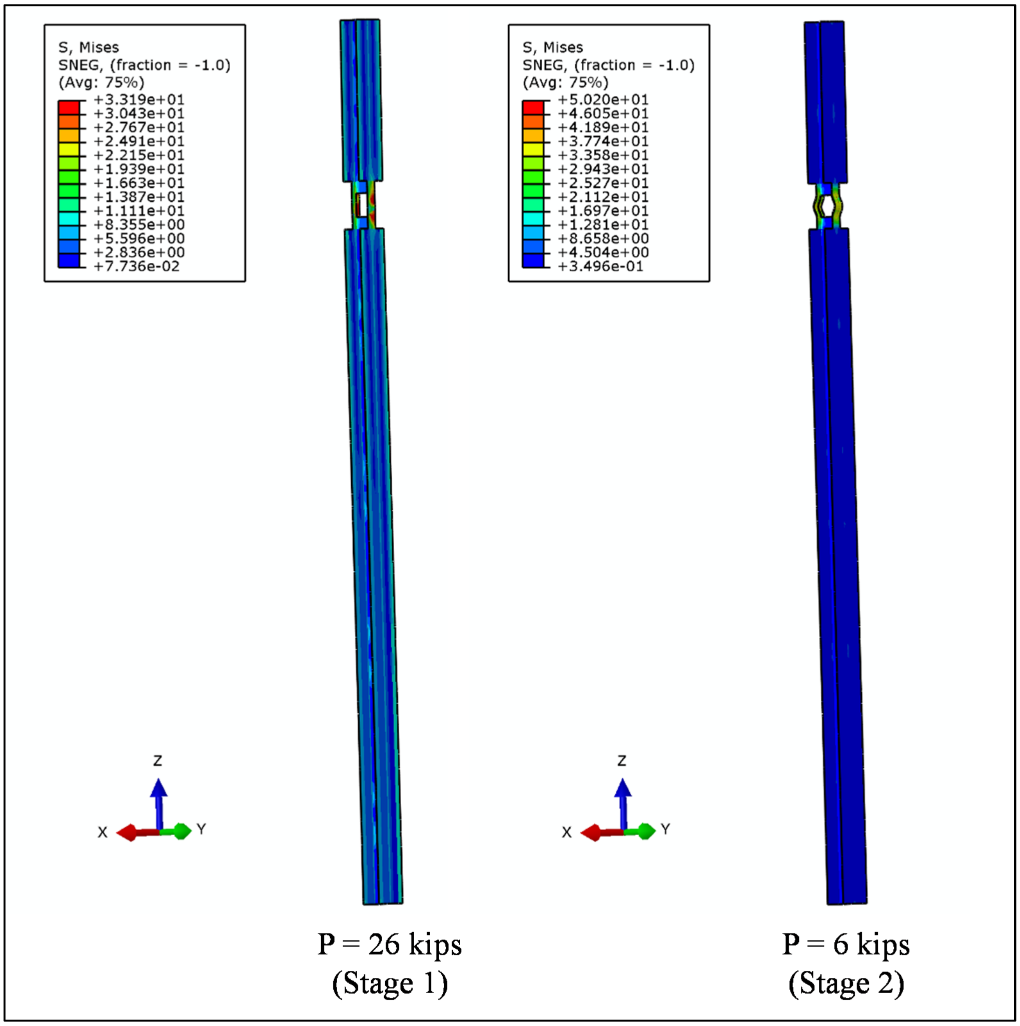

Figure 3.9- Deformed shape and stress contour for pile B4 at different load levels

In addition to the characteristics presented in Table 3.7, pile B4 had a square void with a side length of 12 in. located at the web of its corroded region. Figure 3.8 and Figure 3.9 illustrate the axial load-shortening curve and deformed shape of the pile, respectively. In these, two significant stages are highlighted. Stage 1 represents initial buckling of the pile and corresponds to the peak capacity found in the axial load-shortening curve. Stage 2 represents the residual capacity of the buckled pile and its final deformed shape. Because of severe damage at the corroded region, stresses at the initial buckling stage were concentrated in its flanges. Because of the reduced web support, the two flange ligaments adjacent to the void at the corroded region exhibited one-way bending as the flange reached the yield stress of 33 ksi, as shown in Figure

3.9. The corresponding peak capacity of the pile was 26 kips, as shown in Figure 3.8. As another consequence of the localized corrosion, the axial load-shortening curve presented no kinks, and there were no transitions to different failure modes. The final deformed shape, shown in Figure 3.9 indicates that the failure mode was flange one-way bending, with the flange having yielded and no significant stresses elsewhere. It is notable that for a pile with the maximum length used in this analysis, corrosion damage was so severe that no global buckling occurred. The axial load-shortening curve for pile B14 is presented in Figure 3.10. Its deformed shape and stress contours at different load levels are presented in Figure 3.11.

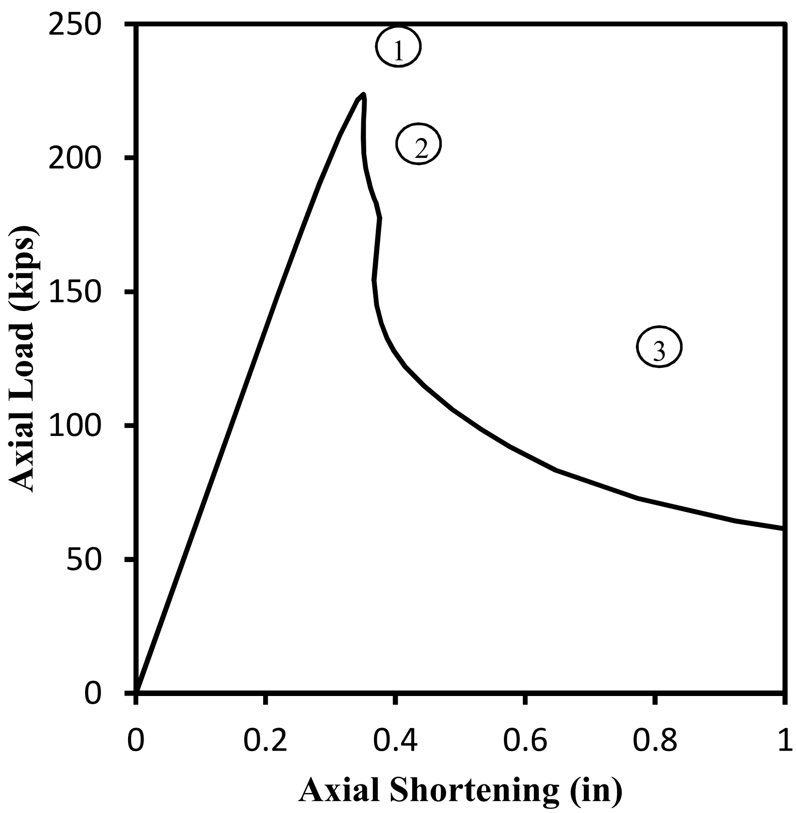

Figure 3.10- Axial load-shortening curve for pile B14

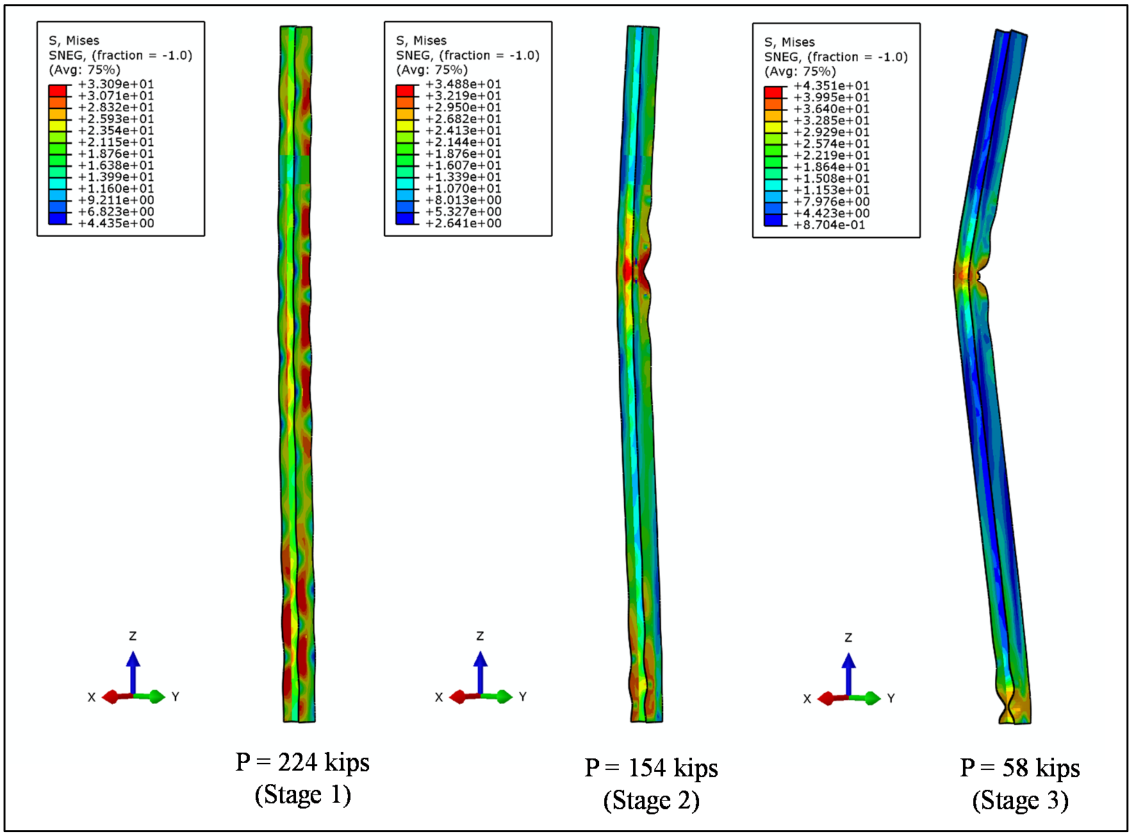

Figure 3.11- Deformed shape and stress contour for pile B14 at different load levels

Figure 3.10 and Figure 3.11 illustrate the axial load-shortening curve and deformed shape of pile B14, respectively. In these, three significant stages are highlighted. Stage 1 represents initial buckling of the pile and corresponds to the peak capacity found in the axial load-shortening curve. Stage 2 represents a transition from local to global failure modes. Lastly, stage 3 corresponds to the residual capacity of the buckled pile and its final deformed shape. The percentage area loss for this pile was 36%, which represented the minimum value for all analyzed piles. At the initial buckling stage, stresses were prevalent in the flanges, but, in contrast to pile B4, there was no significant concentration of stresses at the corroded region. Local buckling of the flange along the length of the pile was induced after yielding, as shown in Figure 3.11. The corresponding peak capacity of the pile was 224 kips, as shown in Figure 3.10. Stage 2 is highlighted by a kink in the axial load-shortening curve. At this stage, flange stresses became concentrated at the corroded region, and a combination of flange local buckling and flexural global buckling ensued, as shown in Figure 3.11. The final deformed shape, shown in Figure 3.14 indicates that the global buckling of the pile, coupled with the initial generalized buckling of the flanges, resulted in a stress concentration at the flanges of the bottom end of the piles, and localized buckling at this section. The axial load-shortening curve for pile G3 is presented in Figure 3.12. Its deformed shape and stress contours at different load levels are presented in Figure 3.13.

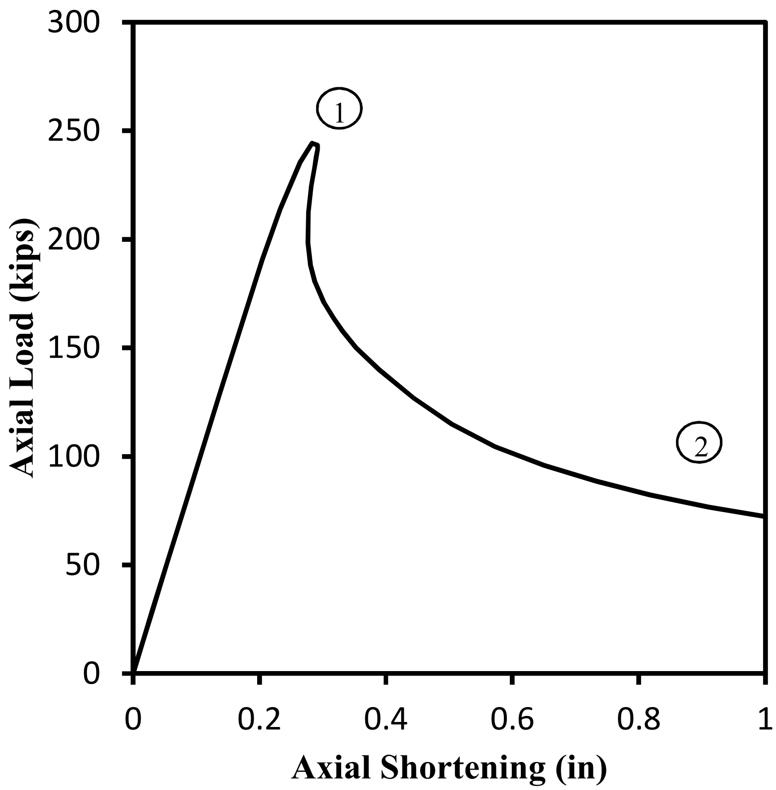

Figure 3.12- Axial load-shortening curve for pile G3

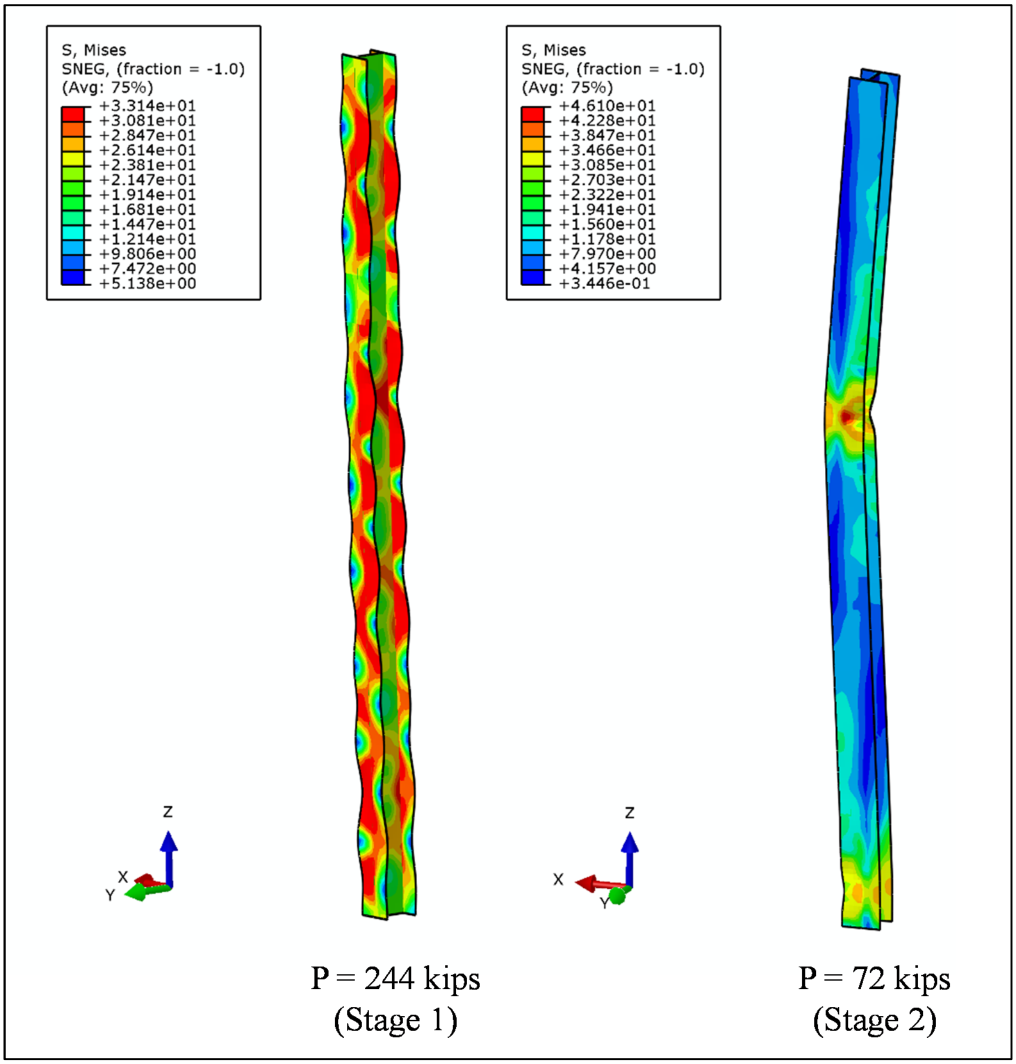

Figure 3.13- Deformed shape and stress contour for pile G3 at different load levels

Figure 3.12 and Figure 3.13 illustrate the axial load-shortening curve and deformed shape of pile G3, respectively. In these, two significant stages are highlighted. Stage 1 represents initial buckling of the pile and corresponds to the peak capacity found in the axial load-shortening curve. Stage 2 corresponds to the residual capacity of the buckled pile and its final deformed shape. Here, the higher stresses are concentrated at the severely corroded region. The percentage area loss for this pile was 46%, which is on the lower end of the spectrum for this set of analyses. This pile was also the shortest in the simulations. At the initial buckling stage, stresses were prevalent in the flanges, and were distributed along the length of the pile. This indicated that damage at the corroded region was not such that it triggered localized stresses, as in the case of pile B4. Local buckling of the flange along the length of the pile was induced after yielding, as shown in Figure 3.13. The corresponding peak capacity of the pile was 244 kips, as shown in Figure 3.12. This capacity represented the maximum calculated for all analyzed piles. Stage 2 is highlighted by the onset of a combination of localized flange local buckling at the corroded region and flexural global buckling. However, the short length of the pile and its relatively low loss of area at the corroded region contributed to this transition not being as drastic as in the case of pile B14. As such, the final deformed shape, shown in Figure 3.13 indicates that the stress concentrations at the flanges of the bottom end of the piles were not as significant as for pile B14. The axial load-shortening curve for pile G18 is presented in Figure 3.14. Its deformed shape and stress contours at different load levels are presented in Figure 3.15.

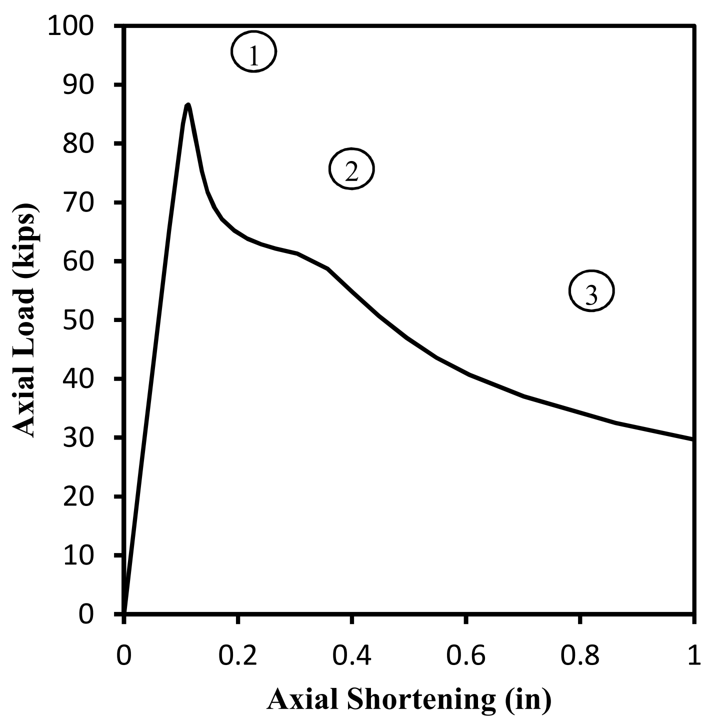

Figure 3.14- Axial load-shortening curve for pile G18

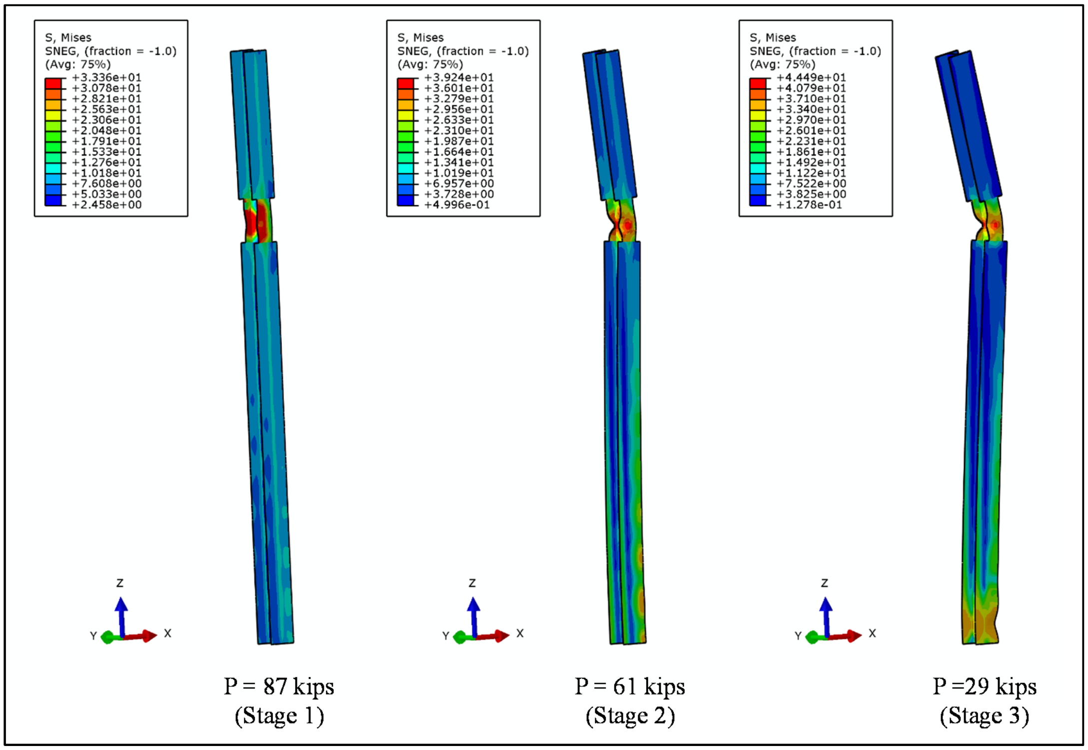

Figure 3.15- Deformed shape and stress contour for pile G18 at different load levels

Figure 3.14 and Figure 3.15 illustrate the axial load-shortening curve and deformed shape of pile B14, respectively. In these, three significant stages are highlighted. Stage 1 represents initial buckling of the pile and corresponds to the peak capacity found in the axial load-shortening curve. Stage 2 represents a transition from local to global failure modes. Lastly, stage 3 corresponds to the residual capacity of the buckled pile and its final deformed shape. The percentage area loss for this pile was 79%, which is at the higher end for all analyzed piles. This pile was also short, with a global length of 325 in. At the initial buckling stage, stresses were prevalent in the flanges, and concentrated at the corroded region because of the severe loss of cross-sectional area. Local buckling of the flange at the corroded region was induced by yielding, as shown in Figure 3.15. The corresponding peak capacity of the pile was 87 kips, as shown in Figure 3.14. Stage 2 is highlighted by a kink in the axial load-shortening curve. At this stage, the further concentration of stresses at the flanges of the corroded region induced flexural global buckling. The final deformed shape, shown in Figure 3.15 indicates that the progression of global buckling resulted in a stress concentration at the flanges of the bottom end of the piles. However, stresses at the flanges of the corroded region continued being the maximum for the member.

A correlation study was conducted in order to assess the dependence of the piles' capacities and elastic stiffnesses on their percentage area loss and global length. The dependence of the peak capacity of the analyzed piles to their percentage area loss is presented in Figure 3.16.

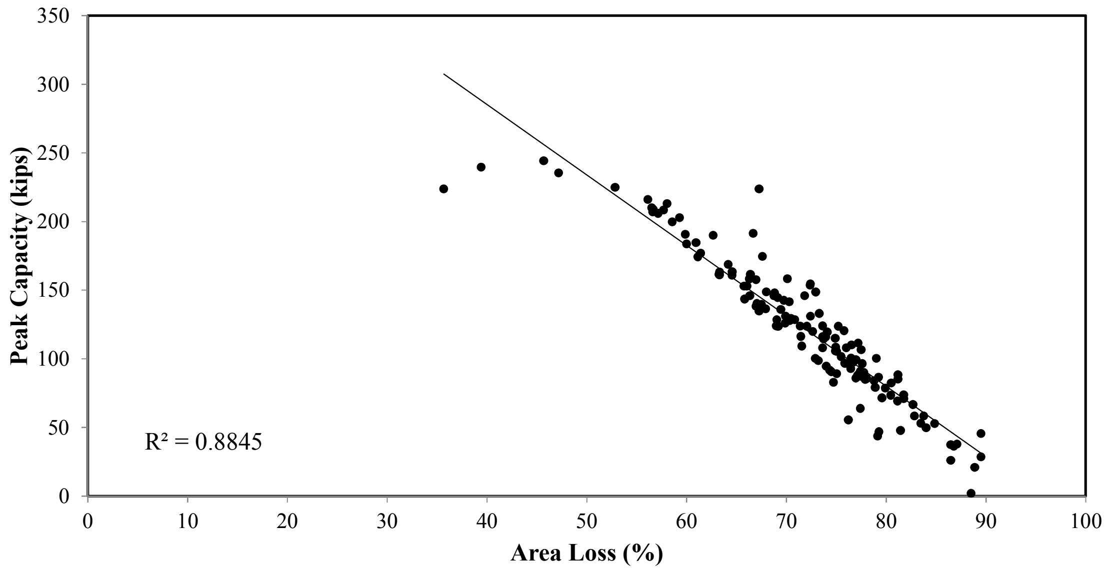

Figure 3.16- Peak capacity vs. Area loss

The peak capacity of the analyzed piles had a strong correlation to their percentage area loss. This correlation had an R^2 value of 0.88, indicating that degradation at the corroded region was the principal factor in determining the capacity of the piles. This figure illustrates why the peak loads generally corresponded to the onset of local buckling, which is dependent on the cross-sectional dimensions at the severely corroded region, instead of global buckling, where pile length is a critical factor. For the analyzed piles, the correlation of peak capacity to global length is presented in Figure 3.17.

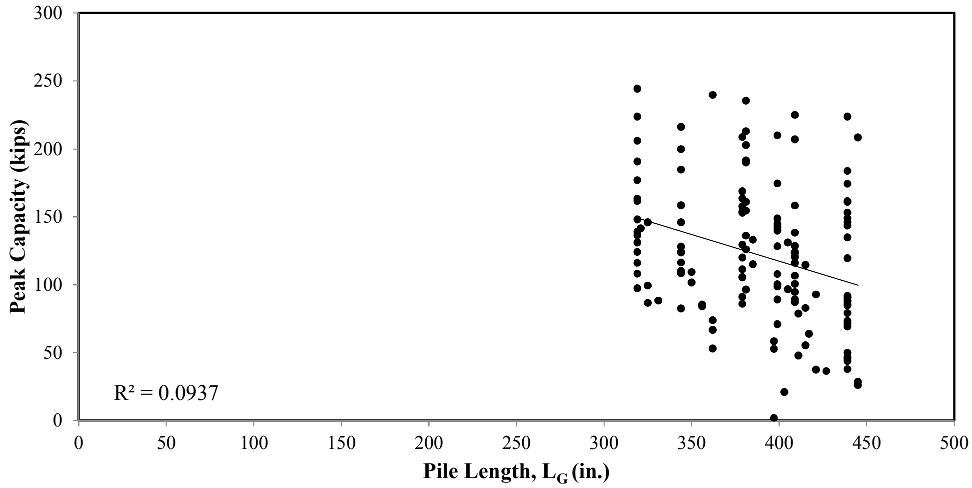

Figure 3.17- Peak capacity vs. Global length

As shown in the previous figure, pile length did not show a significant correlation with peak capacity, rendering an R^2 value of 0.09. The weak correlation between these parameters is a consequence of corrosion being considered a stochastic phenomenon (Xiao, 2004), and having a strong correlation to peak capacity, as shown in Figure 3.16. As such, since the length of the piles was intrinsically related to their location, it was considered that the location of the piles did not influence their peak capacities. Additionally, the weak correlation presented in Figure 3.17 further shows that the peak loads did not generally correspond to global buckling of the piles.

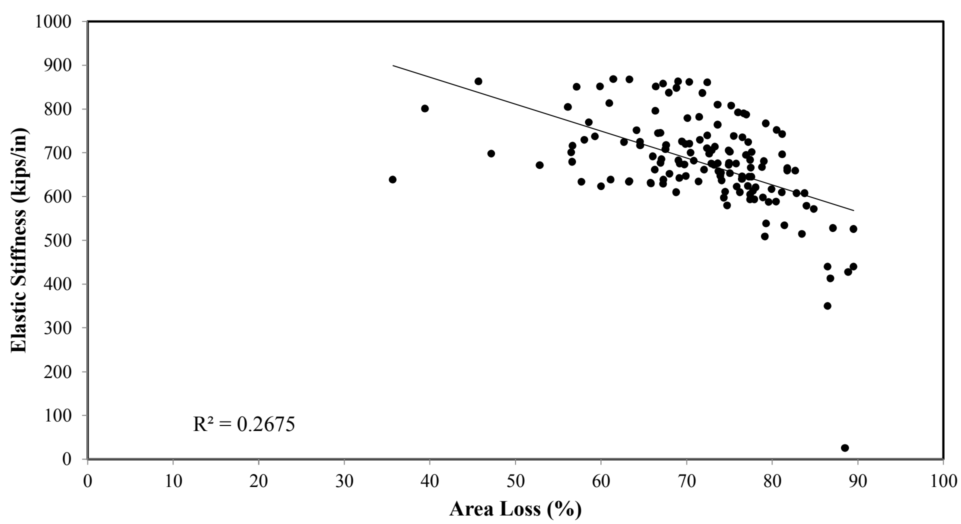

Figure 3.18- Elastic stiffness vs. Area loss

Area loss did not have a strong correlation with elastic stiffness, presenting an R^2 value of 0.27. For prismatic members, the axial elastic stiffness is inversely proportional to length. This figure indicates that, although corrosion degradation has some impact on the elastic stiffness of the piles, pile length remains a prominent factor in its relationship to this parameter. Finally, the correlation of elastic stiffness of the analyzed piles to their global lengths is presented in Figure 3.19.

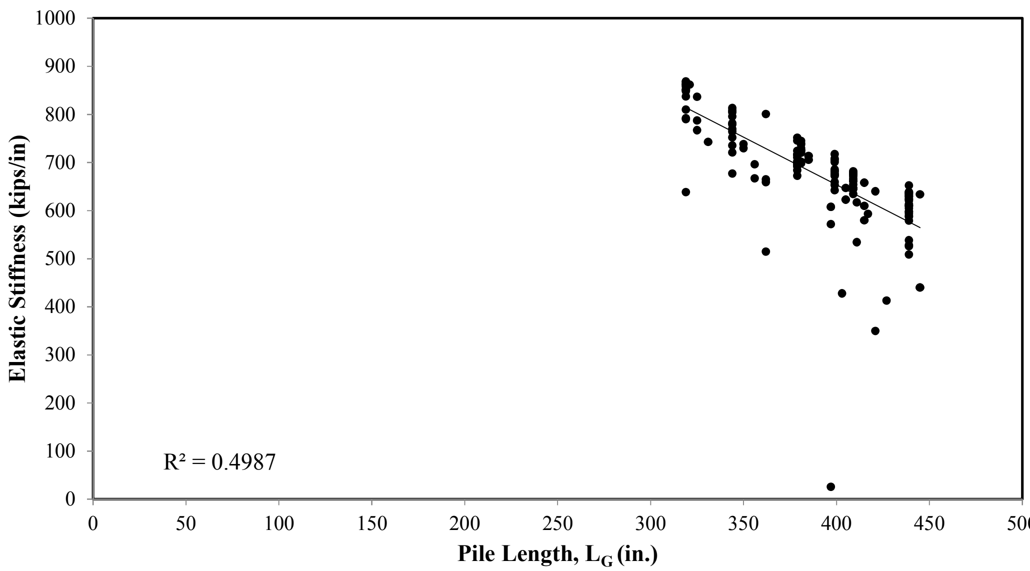

Figure 3.19- Elastic stiffness vs. Global length

Figure 3.19 shows that even as the normally direct correlation between elastic stiffness and pile length was affected by localized corrosion (R^2 value of 0.50), the distribution of pile stiffness could generally be estimated based on their length, and hence, their location.

Chapter 4 : Numerical Study of USS Salem Wharf

4.1 Introduction

The inspections of the USS Salem Wharf concluded that substructure collapse induced by gravity live loads was the primary safety concern. As such, while lateral loads are important and could be significant, this study focused on the collapse load estimation of the structure under gravity loads.

To evaluate the behavior and estimate the collapse capacity of the wharf, a non-linear finite element model was developed in ABAQUS v.6.12 (SIMULIA, 2012). The idealized model of the wharf included the concrete superstructure (slab, bent caps, and beams), supporting vertical piles, battered piles, and sheet piling. In this 3D model, frame elements were used to represent the bent caps, longitudinal beams and battered piles, while the concrete slab and sheet pile were modeled using shell elements. Frame-to-shell tie constraints were applied in the superstructure to ensure stability and avoid 'multiple structures' errors. In order to represent the corroded vertical piles, non-linear connector elements were implemented. The axial load-shortening responses of these elements were defined based on the detailed numerical analysis of the piles that was described in the previous chapter.

Additionally, a parametric study was conducted with the objective of assessing the influence of the superstructure stiffness, redundancy of supporting elements, and distribution of corroded piles on the collapse capacity and failure mode of the structure. Through the statistical analysis of the data stemming from the randomization of the distribution of corroded piles, the collapse capacity for the section of the wharf with unknown pile measurements was estimated.

A detailed description of the model geometry, boundary conditions, loads, analysis steps, element types and meshes is presented in the following sections. The results and discussion associated with the analyses are presented subsequently in the chapter.

4.2 Description of the Finite Element Model

A numerical framework was developed to predict the collapse load and failure mode of the wharf section for which vertical pile geometry information was obtained through inspection. The influence of superstructure stiffness, redundancy of supporting elements, and variability of corrosion pattern on the collapse load of the wharf was analyzed in a parametric study.

As discussed in Chapter 2, the arc length formulation used in the modified Riks analysis enables it to handle geometric and material non-linearity as well as global instabilities and softening. For the analyses presented in this chapter, collapse was identified at the onset of global softening of the structure. Because this type of analysis is able to render unstable equilibrium states, it was deemed appropriate in identifying the collapse load.

Because self-weight (dead) and uniform loads (live) were applied, and the collapse live load was to be estimated, dead and live load effects were de-coupled. An initial general static analysis step, which uses a full Newton solution method, was implemented to assess the self-weight effects and response. Since this procedure can incorporate geometric and material non-linearity and collapse was not expected under pure self-weight loads, it was deemed appropriate for this stage of analysis. Subsequently, a non-linear analysis step using the modified Riks solution method was implemented to predict the response of the wharf under a uniform live load and to predict its collapse capacity, while incorporating the deformed shape and stresses from the general static analysis as the initial state.

The Riks analysis step incrementally magnifies a prescribed uniform pressure load by a parameter known as the load proportionality factor (LPF). That is, the total applied load is equal to the specified pressure load multiplied by this factor. In the analysis configuration, a target value of LPF was set such that it was greater than the sum of the peak capacities of all of the vertical piles in the model. That is, a value that could not be reached without collapse of the structure. As such, the simulation presented positive increments of LPF until a peak load was reached, at which point the applied load decreased indicating the onset of widespread softening and collapse.

4.2.1 Structural Geometry and Sections

The modeled structural geometry and cross-sections of the slab, bent caps, cap beam, longitudinal beams, sheet pile, and battered piles are presented in this section. Front and perspective views of the structure assembly are presented in Figure 4.1 and Figure 4.2, respectively. As noted in Chapter 2, the wharf structure was modeled from bent 1 to bent 20, as that section corresponds to vertical piles that were inspected before procedures were halted for safety considerations.

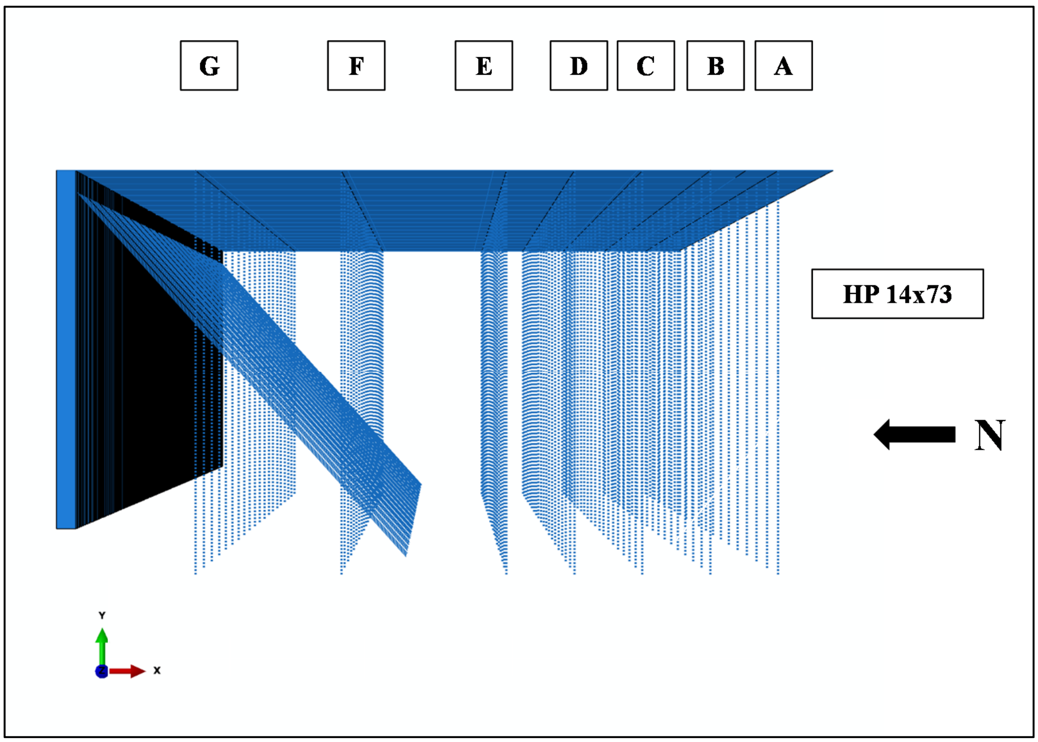

Figure 4.1- Front view of wharf model

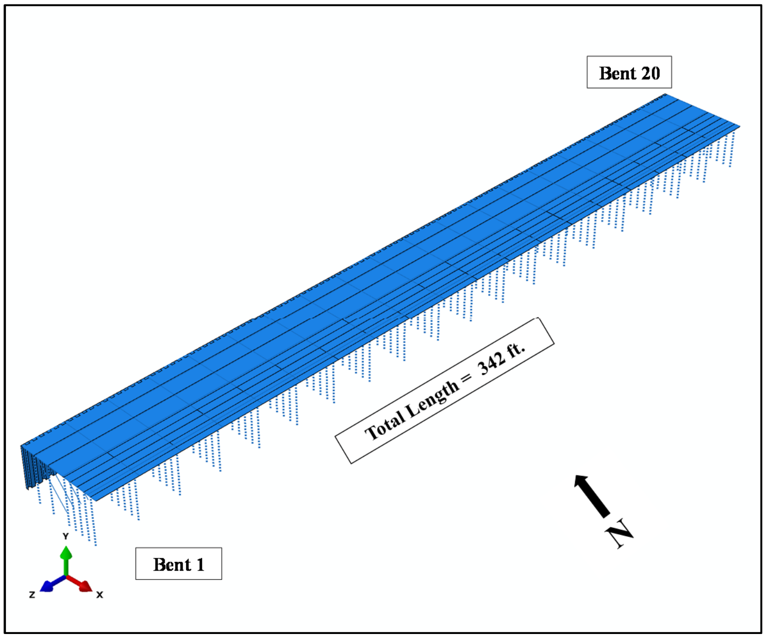

Figure 4.2- Perspective view of wharf model

The configuration of the concrete bent caps in the model is presented in Figure 4.3, below. The spacing and cross-sections of these element are indicated in this figure.

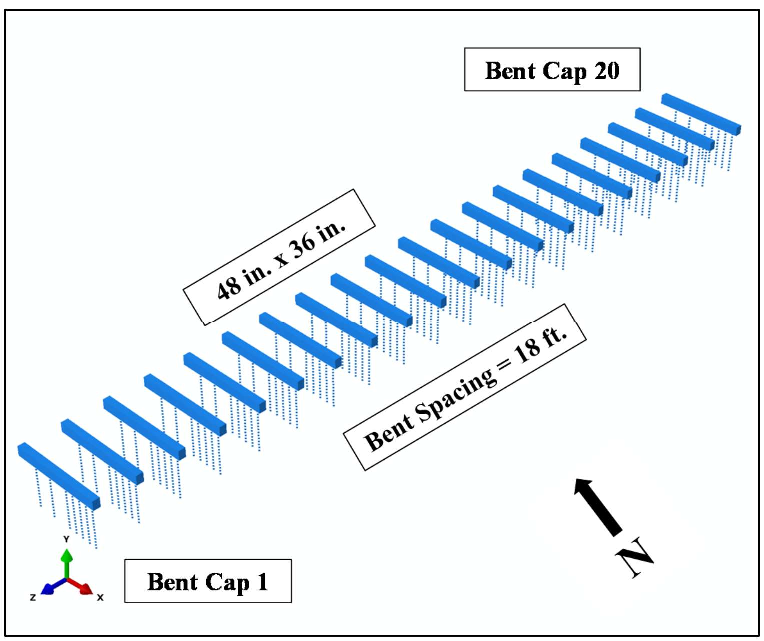

Figure 4.3- Concrete bent cap spacing and cross-section

Figure 4.4 shows the geometry of the slab. The thickness of the slab varies along the width of the wharf as shown in the figure. The slab was modeled using shell elements located at the mid-thickness of the slab. Consequently the top surface of the slab was not flush in the model. However, this difference was not expected to significantly affect the behavior.

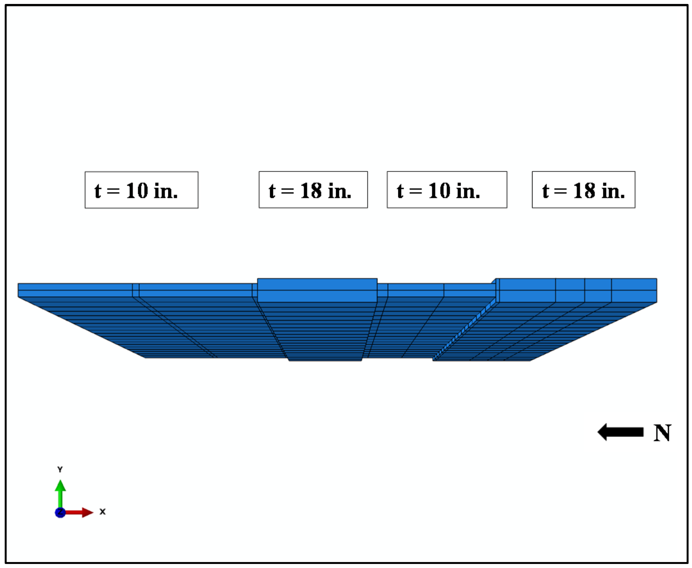

Figure 4.4- Concrete slab cross-section

The configuration of the longitudinal concrete beams and steel battered piles, are presented in Figure 4.5. Here, the corresponding cross-sections are indicated.

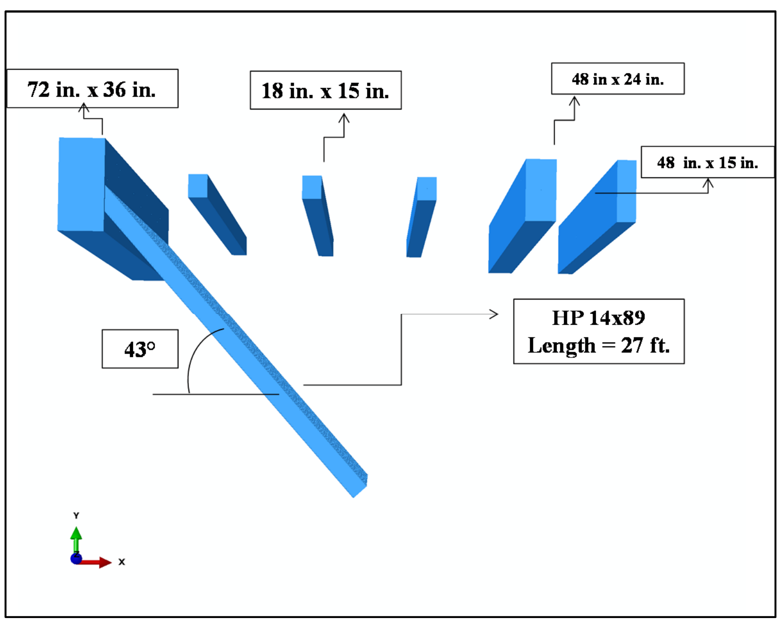

Figure 4.5- Longitudinal beams, cap beam and battered piles cross-sections

As a part of the parametric study, the effect of completely removing the battered piles from the structure was evaluated. Here, the presence of the battered piles was found to have minimal influence on the collapse live load. Thus, the battered piles were assumed to be un-corroded and the cross-sectional dimensions were taken equal to those of the original HP14×89 sections. The results of the parametric study are presented later in this chapter.

As shown in Figure 4.4, the slab was modeled by shell elements that were aligned to its centroid. In this model, the reinforcement details of the superstructure were neglected, and gross cross-sectional properties were used. To represent the differences in performance of the wharf as determined by the stiffness of its concrete superstructure, two models were created. In the first, the concrete superstructure was assumed un-cracked, with linear-elastic behavior. In the second, the linear-elastic behavior assumption was maintained, but the flexural stiffness, EI, of the superstructure was adjusted based on the $I_{cracked}/I_g$ ratios of the longitudinal beams, for which minimum reinforcement requirements were adopted. The most conservative $I_{cracked}/I_g$ ratio for the longitudinal beams was found to be 0.10. As such, in the model with a cracked superstructure, the flexural stiffness of the superstructure, EI, was scaled by this factor. The calculations of the cracked properties of the longitudinal beams followed the transformed section method and are presented in Appendix H. For both assumptions of the stiffness of the superstructure, the maximum stresses were below the rupture modulus of concrete.

The un-cracked and cracked assumptions of the superstructure render the ideal and conservative structural representations of the wharf, respectively. Moreover, because the structure used to sustain higher loads, as discussed in Chapter 2, it was considered that at least some of the concrete sections had cracked. As such, the behavior and collapse capacity determined in the model with reduced flexural stiffness were considered closer to that of the actual wharf. Finally, the perspective and section views of the sheet piles are presented in Figure 4.6.

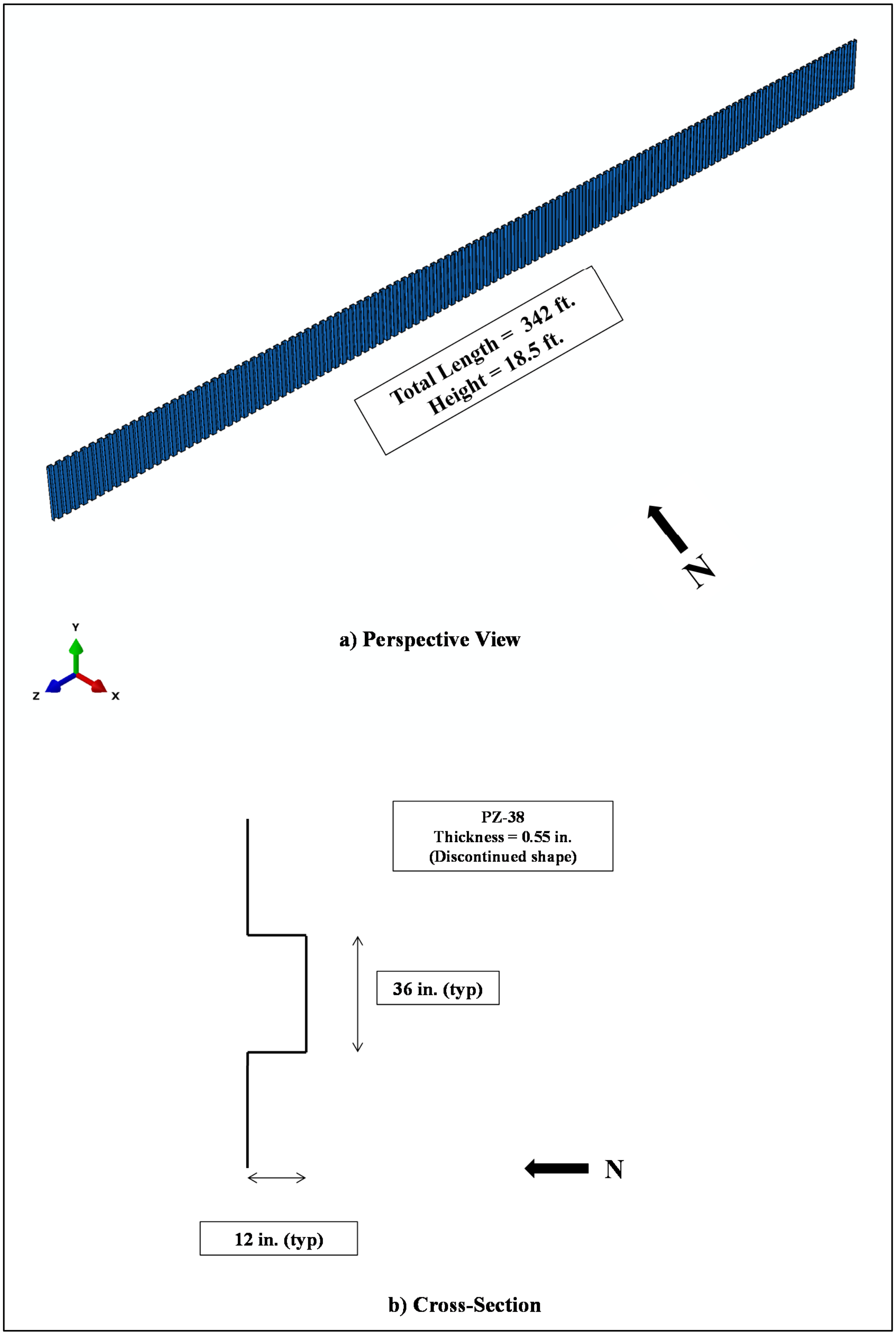

Figure 4.6- Sheet pile dimensions

The vertical piles were modeled as non-linear spring elements with load-shortening relationships determined from the analyses discussed in the previous chapter. As such, no geometry, material or cross-sectional information was defined explicitly for these members.

4.2.2 Boundary Conditions and Loads

In this 3D model, the vertical piles, battered piles and sheet pile were pinned at their bases, while three non-co-linear, non-concurrent restraints were applied to the superstructure in the XZ plane to prevent rigid body motion of the superstructure.

An illustration of the restrained degrees of freedom in the substructure and superstructure are presented in in Figure 3.2 and Figure 4.8, respectively. These boundary conditions were applied to all analysis steps.

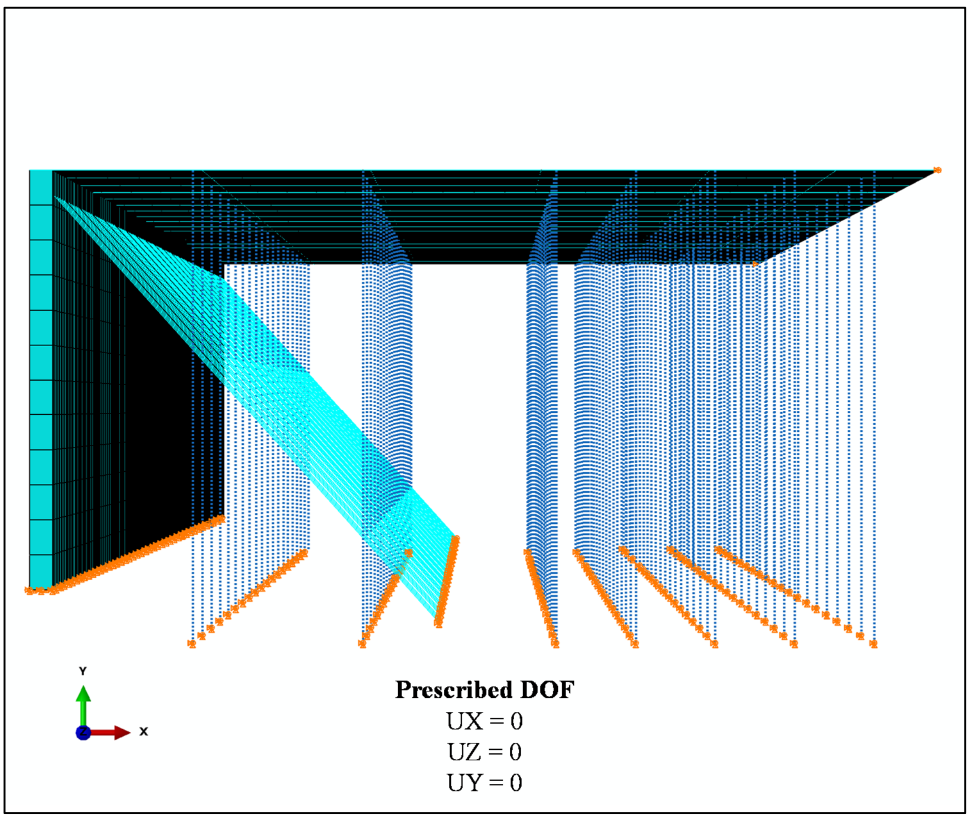

Figure 4.7- Substructure boundary conditions

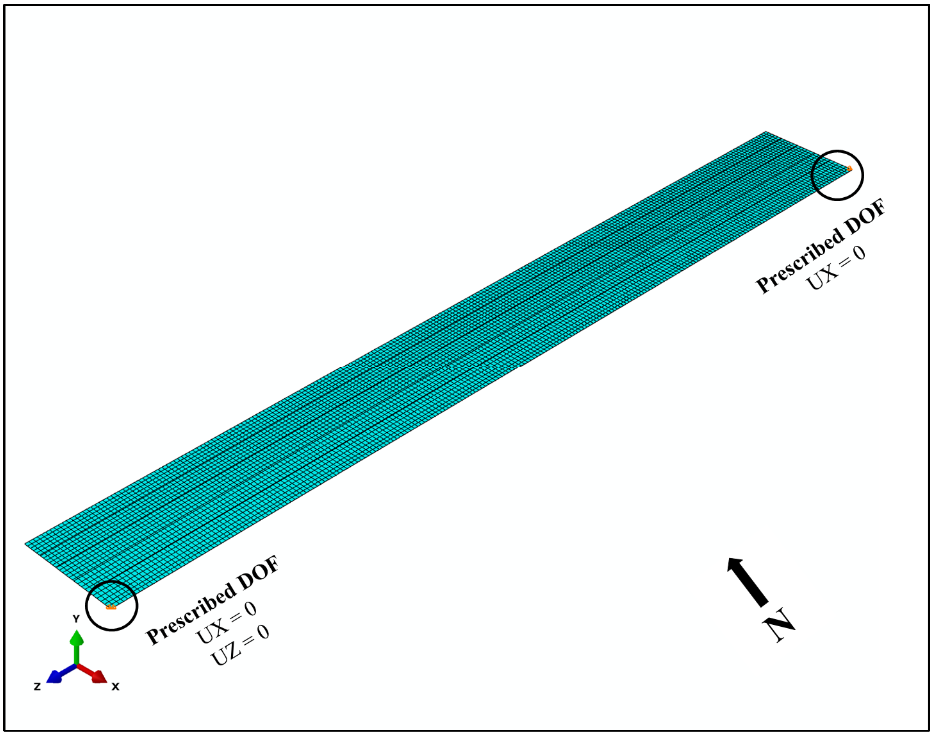

Figure 4.8- Superstructure boundary conditions

In the initial general static analysis step, only the self-weight of the structure was applied. For this, the unit weights of reinforced concrete and steel were taken as 150 lbs/ft^3 and 490 lbs/ft^3, respectively. The analysis results at the end of this step are used as initial conditions for the following Riks analysis step. Here, a reference live load pressure of 144 lbs/ft^2 was applied to the slab. At each increment of this analysis, the total applied live load was the reference pressure multiplied by the corresponding LPF. When the analysis presented a decrease of LPF, the loading history, deformed shape and stress contours were extracted, and the simulation was culminated.

4.2.3 Material Properties

The following sections describe the material models that were adopted for the steel piles, battered piles, sheet pile, concrete slab, concrete bent caps and concrete beams.

- **Steel**

Although the steel from the vertical and battered piles was not tested, the prevalent grades of steel for structural applications in the late 1950s were investigated. AISC Design Guide 15 (Brockenbrough, et al. 2003) indicates that ASTM A7 was the most common grade of steel for structural steel sections at the time the USS Salem Wharf was constructed. ASTM A7 specifies a minimum yield stress of 33 ksi and a minimum ultimate tensile strength of 60 ksi. A bi-linear elasto-plastic model was used to represent the constitutive relationship of all steel elements in the model. In the elastic region, the elastic modulus and Poisson's ratio were assumed to be 29000 ksi and 0.3, respectively. The yield stress corresponds to the minimum specified value for ASTM A7 steel. In order to define the plastic-hardening region, an ultimate plastic strain of 0.15 was assumed, while the corresponding ultimate stress was taken as the minimum specified value for ASTM A7 steel. The summary of material model data and the corresponding material model were presented in Chapter 3, as all steel structural members were assigned this material model.

- **Concrete**

Twenty-one concrete cores were sampled from the different reinforced concrete elements of the structure and 13 of these were tested under axial compression according to ASTM C39 (2012) (P. Schuman, personal communication, 2016). The measured strengths ranged from 5.7 ksi to 9.8 ksi. The core with a compressive strength of 5.7 ksi was tested according to ASTM C469 (2010), and was found to have an elastic modulus of 3000 ksi. For use in analyses, SGH recommended a compressive strength of 5.4 ksi, with elastic modulus and modulus of rupture of 4200 ksi and 0.55 ksi, respectively (P. Schuman, personal communication, 2016).

In this investigation, the compressive strength of concrete was assumed to be 4.0 ksi, with a Poisson's ratio of 0.2. The elastic modulus and modulus of rupture were calculated according to the provisions of ACI 318 (2014), rendering the values presented in Table 3.5.

Table 4.1- Concrete mechanical properties

Compressive Strength	Modulus of Elasticity	Modulus of Rupture	Poisson's Ratio
f'_c (ksi)	E (ksi)	f_t (ksi)	ν
4.0	3605	0.47	0.2

For the wharf model assuming un-cracked concrete sections, the selected concrete mechanical properties resulted in a collapse capacity reduction of nearly 4% compared to the model using the concrete mechanical properties recommended by SGH. For the wharf model with adjusted flexural stiffness, EI, this reduction was approximately 5%. As such, it was confirmed that the selected concrete mechanical properties represented a slightly conservative assumption.

4.2.4 Element Types and Mesh Size

The axial load-shortening response of the corroded vertical piles was obtained as described in Chapter 3. In the complete wharf model the uniaxial non-linear connector element provided by ABAQUS was used to represent the piles. The load-shortening relationships of the piles were represented by a simplified piecewise-linear response that was defined by five points. The points that were used to define the piecewise linear response are defined in Table 4.2, while a comparison between the detailed and idealized load-shortening curves is presented in Figure 4.9.

Table 4.2- Idealized load-shortening curve points

Point No.	P (kips)	D (in.)
1	0	0
2	P_{peak}	D_{peak}
3	$P(D=1.1 \text{ x } D_{peak})$	$1.1 \text{ x } D_{peak}$
4	$P(D=2.0 \text{ x } D_{peak})$	$2.0 \text{ x } D_{peak}$
5	P(D=0.75 in)	0.75

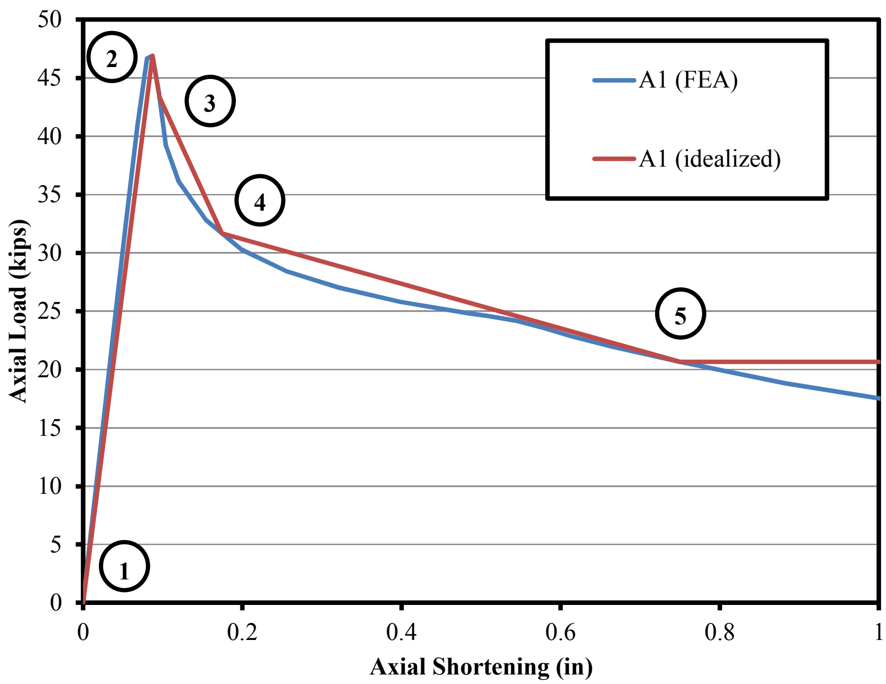

Figure 4.9- Actual vs. idealized load-shortening curve comparison

The first point of this curve corresponds to zero load and displacement. Because behavior until buckling is approximately linear, the second point corresponds to the peak capacity of the pile and its corresponding displacement. Finally, the third, fourth and fifth points were used to characterize the post-buckling behavior of each pile, and correspond to different displacement levels of the load-shortening relationship determined through finite element analysis. The idealized axial load-shortening curves for all the piles are presented in Appendix E.

The general-purpose 4-node finite-membrane-strain element with reduced integration and linear shape functions (S4R) was used for modeling the slab and sheet pile elements, while the 2-node linear frame element (B31) was used to model the bent caps, beams and battered piles. Compatibility of the element types enabled the implementation of tie constraints that served to assemble the different parts of the model, ensure consistency and avoid numerical instabilities.

A mesh sensitivity analysis was conducted in order to determine the appropriate mesh size. The models analyzed in the sensitivity analysis were based on an assumption of un-cracked concrete sections. For S4R elements, approximate mesh sizes of 36 in. x 36 in., 18 in. x 18 in. and 9 in. x 9 in., were implemented with consistent element lengths assigned to B31 elements. The collapse live load results of the mesh sensitivity analysis are shown in Figure 4.10. Here, the mesh size, h, is represented by the length of frame elements and side-length of shell elements. The number of elements per type, number of nodes and central processing unit (CPU) time required to run each model on a desktop PC with an Intel Core 2 Duo central processing unit (CPU) with an installed memory (RAM) of 5.00 GB and a 64 bit operating system are presented in Table 4.3.

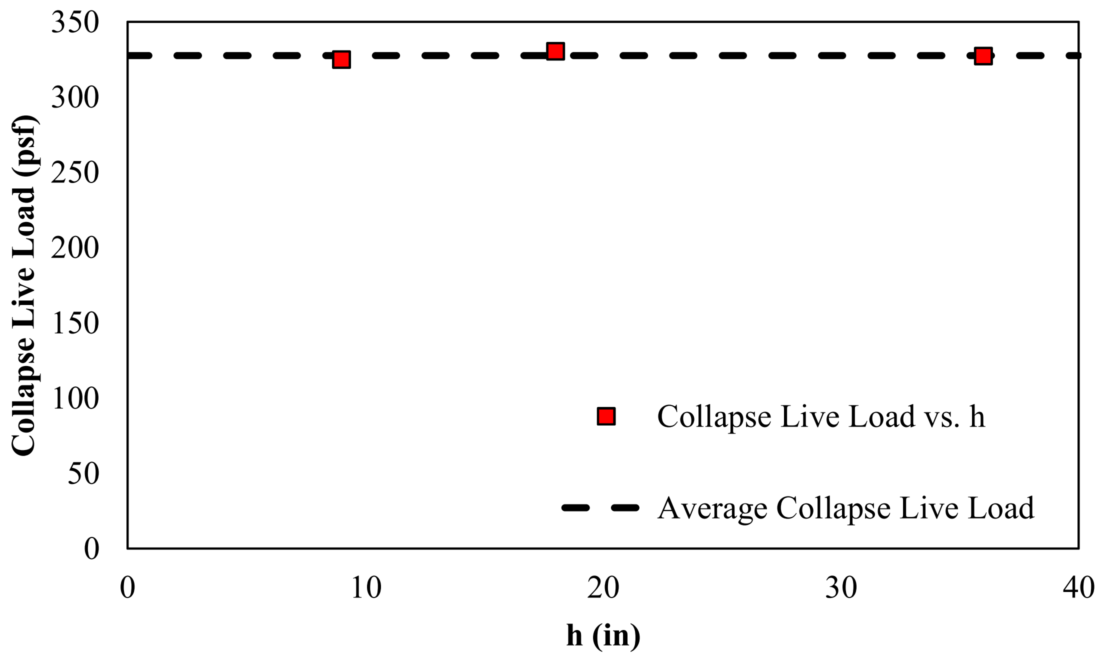

Figure 4.10- Wharf model sensitivity analysis

Table 4.3- Mesh information for sensitivity analysis

h (in.)	No. of Nodes	No. of B31 elements	No. of S4R elements	CPU time (s)	Collapse Live Load (psf)
9	49455	7373	40835	764	327
18	15368	2518	12096	109	330
36	6896	1594	4680	71	325

The maximum difference in collapse live load capacity in the sensitivity analysis was found to be 1.51%, with an average predicted capacity of 327 psf. In order to balance numerical accuracy and computational efficiency, a mesh size of 18 in. × 18 in. was selected for S4R elements, while an element size of 18 in. was assigned to B31 elements for the collapse analysis of the wharf structure and ensuing parametric study.

Table 4.4 summarizes the structural components of the model, and the element types and sizes selected for their representation within this numerical framework.

Table 4.4- Selected element type and mesh size for FE modeling

Part	Element Type	Element Size (in.)
Vertical Piles	Connector	-
Sheet Pile	S4R	18×18
Slab	S4R	18×18
Battered Piles	B31	18
Bent Cap	B31	18
Beams	B31	18

4.3 Results of Salem Wharf Analysis

The analysis results of the USS Salem Wharf from bent 1 to bent 20 are presented in this section. The numerical framework described previously was used to determine the maximum uniform pressure load that could be applied to the modeled structure, until buckling of the vertical piles concluded in collapse. The capacity and elastic stiffness distribution of the vertical piles in the model are presented in Figure 4.11 and Figure 4.12, respectively.

Capacity (kips)

	1	2	3	4	5	6	7	8	9	10	11	12	13	14	15	16	17	18	19	20
G	191	177	245	89	148	162	109	117	100	131	146	98	206	125	164	140	137	87	224	142
F	200	84	110	86	111	67	109	159	240	124	74	83	124	146	217	185	117	54	128	102
E	209	59	134	2	91	59	106	154	153	21	53	112	106	86	169	158	164	120	115	130
D	145	64	71	48	101	79	175	210	108	99	38	149	140	101	90	143	141	97	129	132
C	208	226	93	115	56	37	117	107	124	90	83	88	124	129	95	101	139	124	121	159
B	153	184	85	27	50	70	144	120	74	86	135	91	46	224	162	162	88	72	146	92
A	47	97	155	149	29	126	190	91	175	192	137	44	89	236	161	80	38	203	214	209

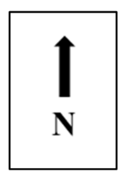

Legend:

- 75^{th} Percentile to 100^{th} Percentile
- 75th Percentile to 100th Percentile
- 75th Percentile to 100th Percentile
- 0th Percentile to 100th Percentile

Figure 4.11- Wharf model vertical pile capacity distribution

Stiffness (kip/in)

	1	2	3	4	5	6	7	8	9	10	11	12	13	14	15	16	17	18	19	20
G	852	869	863	743	849	852	792	810	788	861	837	791	851	864	868	858	838	768	639	862
F	770	668	730	697	736	660	678	780	802	808	666	753	765	796	805	814	782	515	721	739
E	717	608	714	26	684	608	673	711	692	428	572	725	703	695	752	746	717	698	706	701
D	643	594	660	535	681	617	718	702	677	673	350	706	709	676	654	674	686	623	683	647
C	680	672	640	659	611	414	647	666	635	646	580	646	662	682	655	647	678	676	676	662
B	632	624	594	440	580	610	630	637	589	621	630	614	526	639	634	636	625	588	610	598
A	539	702	740	653	440	721	725	612	639	745	726	509	605	699	726	599	528	738	730	634

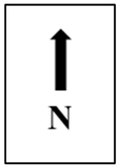

Legend:

- 75th Percentile to 100th Percentile
- 75th Percentile to 100th Percentile
- 75th Percentile to 100th Percentile
- 0th Percentile to 100th Percentile

Figure 4.12- Wharf model vertical pile elastic stiffness distribution

In Figure 4.11 and Figure 4.12, the reference axes of the structure were included in order to identify the piles, as discussed in Chapter 2. Here, each cell at the intersection of a longitudinal (A to G) to transverse (1 to 20) axis represents one of the 140 analyzed piles. A color legend was included in order to characterize the capacity and stiffness distribution of the piles in the model. Here, different colors were used to identify piles in the 25th, 50th, 75th and 100th percentile of the corresponding quantity.

To quantitatively characterize the behavior of the structure at different stages of analysis, it was necessary to identify which piles were close to reaching their peak capacity, which had already buckled, and those on the descending branches of their load-shortening relationship. For this purpose, the displacement vs. displacement-at-peak ratio (D/D_{peak}) was introduced as shown in Figure 4.14 and computed for each pile at the different stages of the simulation. In this sense, $D/D_{peak} < 1$ indicates that the pile has yet to reach its peak capacity, while $D/D_{peak} > 1$ indicates that the pile exhibits post-buckling softening behavior.

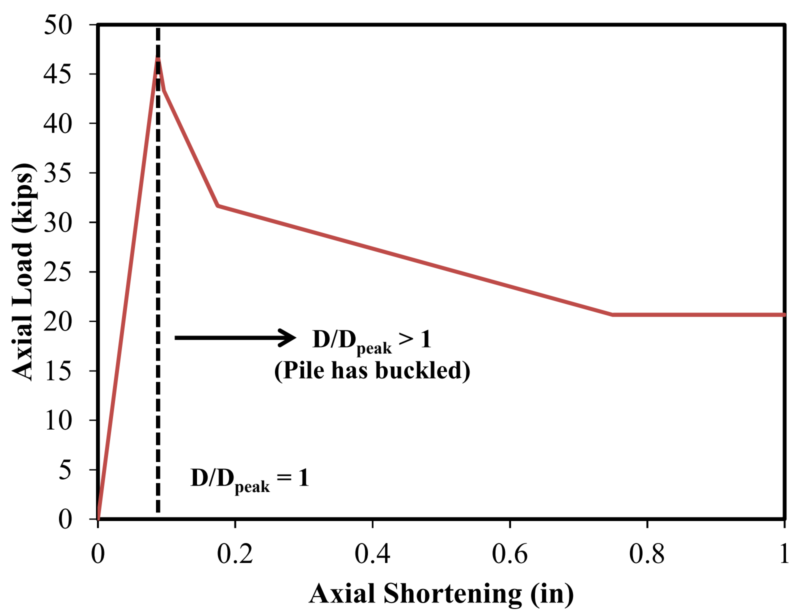

Figure 4.13- Deformed shapes after self-weight step

The deformed shapes for the models with un-cracked and cracked superstructures after the conclusion of the general static analysis step are presented in Figure 4.14. These figures include the contour of the vertical component of displacement (in inches). The distribution of D/D_{peak} for the piles in the models with un-cracked and cracked superstructures, after the introduction of self-weight effects, is presented in Figure 4.15 and Figure 4.16, respectively. The total self-weight of the structure was 6178 kips.

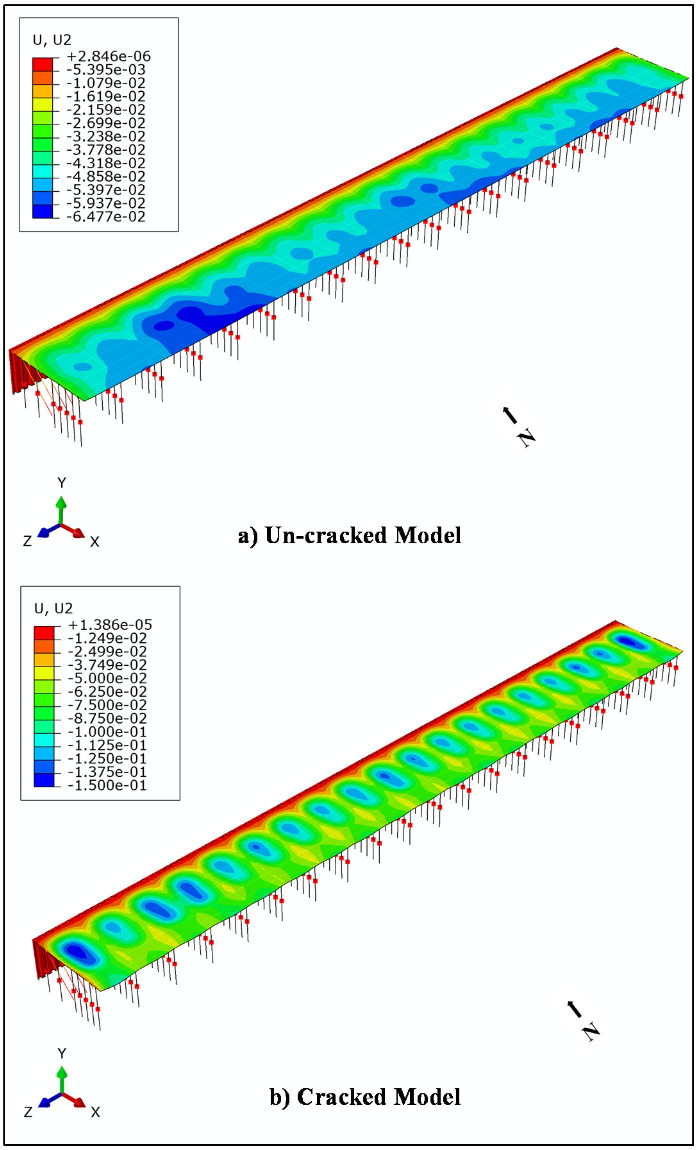

Figure 4.14- Deformed shapes after self-weight step

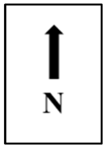

D/D_{peak}

	1	2	3	4	5	6	7	8	9	10	11	12	13	14	15	16	17	18	19	20
G	0.07	0.11	0.08	0.22	0.13	0.12	0.17	0.15	0.18	0.15	0.14	0.18	0.09	0.15	0.11	0.13	0.13	0.21	0.07	0.10
F	0.10	0.32	0.27	0.39	0.27	0.40	0.24	0.18	0.13	0.26	0.38	0.35	0.23	0.20	0.14	0.16	0.25	0.40	0.22	0.19
E	0.10	0.49	0.26	0.78	0.37	0.51	0.29	0.20	0.20	0.99	0.56	0.30	0.30	0.35	0.19	0.21	0.20	0.28	0.28	0.15
D	0.13	0.44	0.46	0.66	0.35	0.40	0.19	0.15	0.29	0.34	0.49	0.23	0.23	0.30	0.33	0.21	0.23	0.31	0.25	0.14
C	0.10	0.14	0.35	0.34	0.60	0.59	0.26	0.29	0.25	0.36	0.37	0.37	0.26	0.25	0.32	0.30	0.24	0.27	0.26	0.12
B	0.12	0.17	0.36	0.98	0.66	0.46	0.21	0.26	0.40	0.36	0.24	0.36	0.59	0.14	0.18	0.19	0.36	0.41	0.20	0.19
A	0.35	0.36	0.25	0.25	0.93	0.30	0.19	0.34	0.19	0.19	0.28	0.64	0.37	0.15	0.22	0.39	0.74	0.18	0.17	0.09

Figure 4.15- D/D_{peak} after self-weight step in un-cracked model

N

D/D_{peak}

	1	2	3	4	5	6	7	8	9	10	11	12	13	14	15	16	17	18	19	20
G	0.09	0.15	0.10	0.29	0.17	0.16	0.23	0.21	0.23	0.19	0.18	0.24	0.12	0.20	0.15	0.17	0.18	0.31	0.10	0.13
F	0.13	0.46	0.35	0.58	0.35	0.56	0.35	0.25	0.17	0.36	0.53	0.47	0.31	0.27	0.18	0.21	0.34	0.61	0.32	0.25
E	0.09	0.57	0.26	1.12	0.36	0.56	0.31	0.21	0.21	1.21	0.65	0.30	0.30	0.37	0.20	0.21	0.20	0.30	0.30	0.15
D	0.10	0.45	0.40	0.78	0.30	0.38	0.17	0.13	0.26	0.34	0.51	0.19	0.21	0.27	0.30	0.19	0.20	0.28	0.24	0.12
C	0.08	0.15	0.31	0.35	0.54	0.58	0.24	0.27	0.23	0.35	0.37	0.34	0.24	0.23	0.30	0.28	0.22	0.24	0.26	0.10
B	0.11	0.17	0.31	0.93	0.64	0.43	0.19	0.25	0.38	0.33	0.23	0.34	0.57	0.13	0.17	0.19	0.35	0.36	0.20	0.16
A	0.35	0.37	0.22	0.23	0.99	0.28	0.18	0.35	0.19	0.17	0.25	0.68	0.38	0.14	0.21	0.40	0.79	0.17	0.17	0.08

Figure 4.16- D/D_{peak} after self-weight step in cracked model

After the general static analysis step was concluded, there were several differences in the behavior of the models with un-cracked and cracked superstructures. As shown in Figure 4.13, the maximum vertical deflection in the un-cracked model was of 0.06 in., while that of the cracked model was 0.15 in. In Figure 4.15 and Figure 4.16, the highlighted cells represent piles that buckled at the end of the self-weight step. No piles buckled under the self-weight of the structure in the un-cracked model, with pile E10 being closest and having a D/D_{peak} ratio of 0.99. Pile E10 is below the 25^{th} percentile in peak capacity among the analyzed piles, with a peak capacity of 21 kips. In the cracked model, piles E4 and E10 buckled under the application of self-weight. Pile E4 is the weakest pile in the simulation, with a peak capacity of 2 kips.

For un-cracked and cracked models, the results of the general static analysis were taken as initial conditions in a static Riks analysis that increments the reference uniform live load until collapse. In this procedure, a target load was set as a stopping criterion of the calculations. That is, if the live load reached the prescribed target load, the analysis was concluded. To ensure that collapse occurred within the simulation time, a target load of 2880 psf (39398 kips) was assigned, while the sum of the peak capacities of all the supporting piles was 17064 kips. As such, the target load could not be reached and the analysis converged at the collapse live load. The live load vs. arc length plots describing the progression of the Riks analysis for the un-cracked and cracked models are presented in Figure 4.17 and Figure 4.18, respectively.

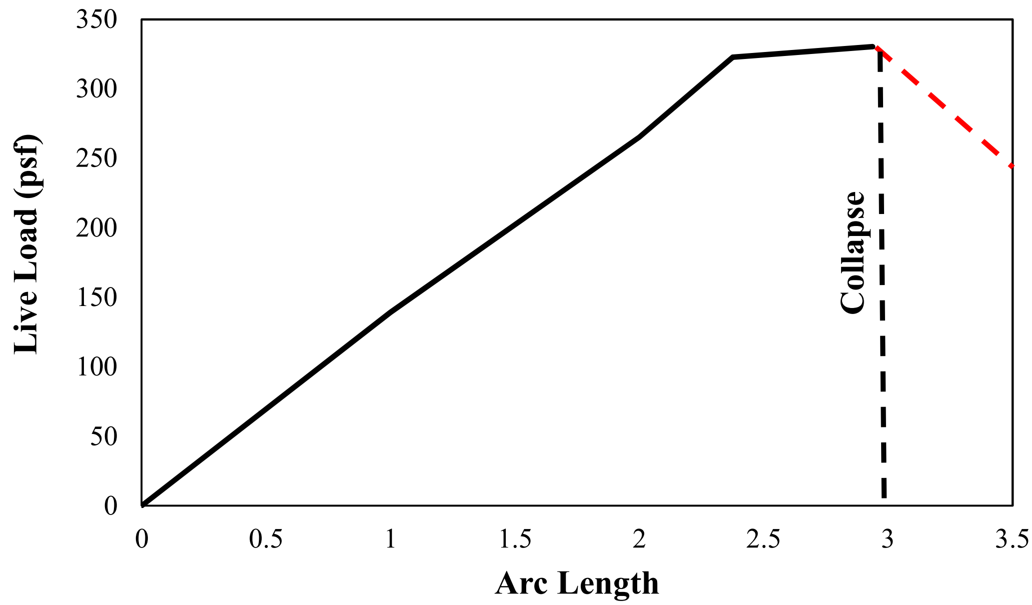

Figure 4.17- LPF vs. arc-length in un-cracked model

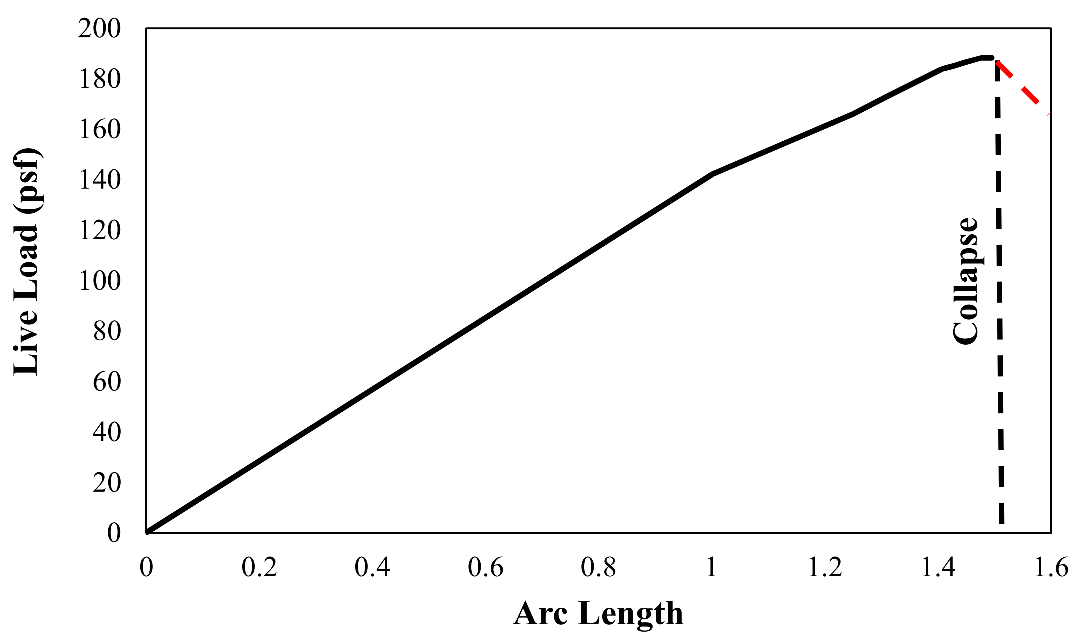

Figure 4.18- LPF vs. arc-length in cracked model

The collapse point was identified as the point where live load could no longer be increased. In the un-cracked model, the collapse live load was found to be 330 psf, while this was 186 psf in the cracked model. This showed that applying a modification factor of 0.10 to the flexural stiffness of the superstructure (representing a fully cracked superstructure) resulted in a 44% reduction in collapse live load capacity with respect to the un-cracked model. As such, the stiffness of the superstructure was considered a prominent factor in the redistribution of loads between the piles and, hence, the performance of the structure. For this reason, the influence of the superstructure stiffness is analyzed in more detail further in this chapter.

The deformed shapes of the un-cracked and cracked models of the structure at the collapse step are presented in Figure 4.19 and Figure 4.20, respectively. These figures include the contour of the vertical component of displacement (in inches).

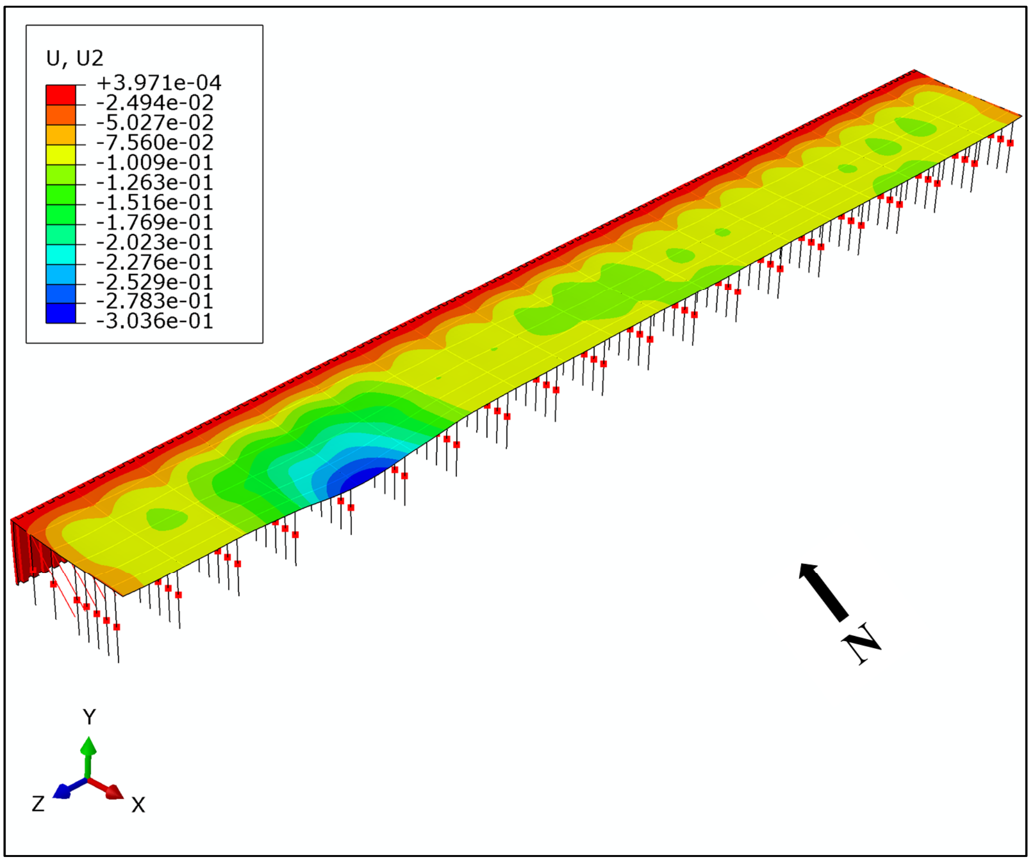

Figure 4.19- Deformed shape at collapse for un-cracked model

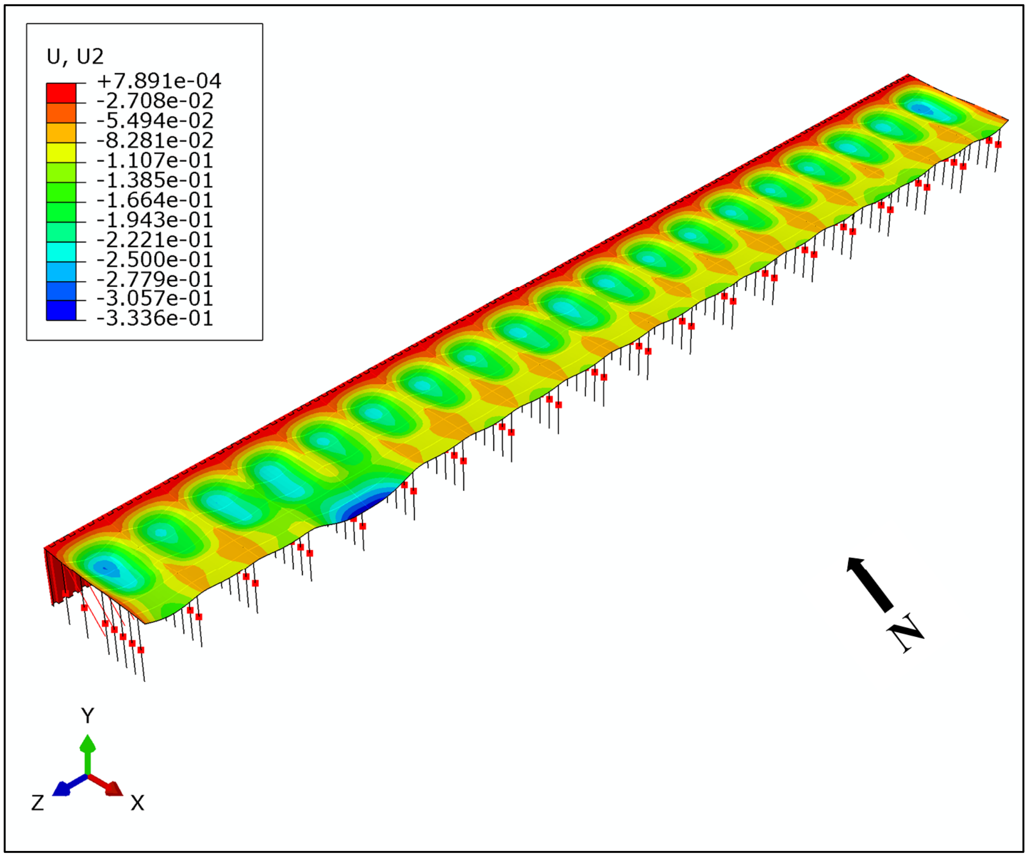

Figure 4.20- Deformed shape at collapse for cracked model

The maximum total vertical displacement immediately prior to collapse was of 0.30 in. for the un-cracked model, and 0.33 in. for the cracked model. In both models, the deformation contour indicated that the largest deflections were concentrated in the vicinity of pile A5. However, in the model with cracked concrete sections, there were also significant deflections along the mid-section of the structure. This finding showed that the seemingly rigid behavior of the superstructure in the un-cracked model made the deformed shape primarily dependant on the behavior of the piles. In contrast, the deformed shape of the cracked model was further influenced by the more flexible behavior of the superstructure.

The D/D_{peak} graphs for the un-cracked and cracked models are presented in Figure 4.21 and Figure 4.22, respectively. Here, the progression of failure of the substructure is also illustrated.

D/D_{peak}

	1	2	3	4	5	6	7	8	9	10	11	12	13	14	15	16	17	18	19	20
G	0.13	0.23	0.17	0.51	0.35	0.34	0.36	0.31	0.37	0.33	0.30	0.38	0.19	0.31	0.23	0.27	0.27	0.44	0.13	0.17
F	0.18	0.64	0.56	0.96	0.83	1.26	0.53	0.37	0.26	0.59	0.83	0.72	0.47	0.42	0.28	0.33	0.52	0.82	0.45	0.34
E	0.17	0.95	0.52	2.09	1.41	1.82	0.63	0.39	0.41	2.17	1.17	0.60	0.59	0.70	0.38	0.41	0.39	0.55	0.55	0.27
D	0.22	0.84	0.91	1.84	1.44	1.46	0.42	0.28	0.56	0.70	1.00	0.45	0.46	0.58	0.63	0.41	0.45	0.60	0.47	0.24
C	0.16	0.26	0.68	0.97	2.60	2.24	0.58	0.52	0.46	0.72	0.73	0.72	0.50	0.46	0.59	0.58	0.47	0.51	0.50	0.20
B	0.20	0.29	0.69	2.91	3.02	1.81	0.46	0.44	0.72	0.69	0.46	0.68	1.10	0.25	0.34	0.36	0.71	0.76	0.37	0.30
A	0.55	0.62	0.47	0.77	4.37	1.22	0.40	0.57	0.33	0.35	0.51	1.21	0.67	0.26	0.39	0.72	1.47	0.34	0.30	0.14

N

Legend:

- Buckled before 139 psf live load
- Buckled before 265 psf live load
- Buckled before 323 psf live load
- Buckled before 330 psf live load

Figure 4.21- D/D_{peak} at collapse in un-cracked model

D/D_{peak}

	1	2	3	4	5	6	7	8	9	10	11	12	13	14	15	16	17	18	19	20
G	0.13	0.25	0.17	0.47	0.26	0.26	0.37	0.33	0.38	0.32	0.29	0.40	0.19	0.32	0.24	0.28	0.29	0.50	0.16	0.18
F	0.18	0.76	0.58	1.00	0.53	0.91	0.56	0.41	0.28	0.64	0.89	0.77	0.51	0.45	0.30	0.35	0.55	1.00	0.52	0.36
E	0.13	0.90	0.40	2.12	0.61	0.88	0.48	0.33	0.33	2.27	1.08	0.47	0.48	0.58	0.31	0.33	0.30	0.47	0.48	0.22
D	0.14	0.69	0.60	1.56	0.66	0.59	0.26	0.20	0.40	0.60	0.82	0.30	0.32	0.42	0.45	0.29	0.30	0.42	0.36	0.16
C	0.10	0.22	0.45	0.71	1.61	0.89	0.35	0.40	0.34	0.55	0.56	0.49	0.35	0.33	0.43	0.41	0.34	0.35	0.39	0.13
B	0.14	0.24	0.44	1.94	2.38	0.68	0.27	0.35	0.54	0.48	0.33	0.49	0.82	0.18	0.25	0.27	0.58	0.52	0.29	0.21
A	0.46	0.53	0.31	0.46	4.19	0.46	0.24	0.50	0.27	0.24	0.35	0.96	0.54	0.20	0.30	0.58	1.45	0.24	0.25	0.11

N

Legend:

- Buckled under self-weight
- Buckled before 142 psf live load
- Buckled before 166 psf live load
- Buckled before 186 psf live load

Figure 4.22- D/D_{peak} at collapse in cracked model

The theoretical maximum capacity of the structure would be reached if all piles buckled prior to collapse. Although this cannot be achieved, the number of piles that can buckle prior to collapse is an indicator of the load redistribution and redundancy characteristics of the structure.

In the un-cracked model, piles B4, E4, A5 and E10 buckled before the applied live load reached 139 psf. All of these piles were below the 25th percentile with respect to their peak capacities. As live load increased to 265 psf, piles D4, B5, C5, E11 and A12 buckled. For most of these, the proximity to previously buckled piles was notable. This sequential buckling of proximate piles was considered a main characteristic of the collapse mechanism. Piles B6, E6, B13 and A17 buckled as live load reached 323 psf, and, finally, piles A6, D5, D6, E5, F6 and D11 buckled prior to collapse at 330 psf. Figure 4.21 shows that only one of the buckled piles, A17, did not have an adjacent buckled pile. These findings demonstrated that buckling of the piles generally occurred locally after an adjacent pile had buckled and the superstructure redistributed load to the adjacent piles.

The cracked model followed a similar collapse pattern. As previously mentioned, piles E4 and E10 buckled under self-weight loading, while piles A5, B4, D4, D5 and A17 buckled as live load reached 142 psf. Finally, pile C5 buckled as live load was increased to 166 psf, while piles E11 and F18 buckled as the collapse load of 186 psf was reached. Here, the mechanism was initiated by buckling of the two weakest piles in the model, and a similar collapse region as that of the un-cracked model was developed. However, because the superstructure was less stiff, the load could not be further redistributed after buckling of the noted piles. It was noted that all of the piles that buckled prior to live load reaching 139 psf in the un-cracked model, also buckled at collapse of the cracked model. This indicated a consistence of the collapse mechanisms between the models. However, because of the difference in load redistribution capacities, some of the piles that buckled in the later stages of analysis of the un-cracked model did not reach their peak loads in the cracked model prior to collapse.

Additionally, it is notable that piles in the G-line, which are among the stiffest, did not buckle in any of the models. This suggests a significant contribution of the sheet pile in carrying the applied load. The load distribution at collapse is presented in Table 4.5.

Table 4.5- Load distribution at collapse

Model	**Vertical Piles kips (%)**	**Sheet Pile kips (%)**	**Battered Piles kips (%)**	**Total (kips)**
Un-cracked	7481 (67)	3251 (29)	404 (4)	11136
Cracked	6271 (72)	2261 (26)	196 (2)	8728

As validated in Table 4.5, the presence of the sheet pile contributed to shifting the load away from the G-line, even as it has the generally stiffer piles. The influence of the sheet pile and battered piles will be further analyzed in the parametric study presented in the following section.

4.4 Parametric Study

A series of numerical analyses were conducted on the basis of the developed numerical framework in order to investigate the effects of removing sheet and battered piles, magnifying or reducing the superstructure stiffness, altering the redundancy of supporting elements and randomizing the distribution of corroded piles. The findings of this parametric study are presented in the following sections.

4.4.1 Influence of the Sheet Pile and Battered Piles

The collapse live loads obtained by removing the battered piles only, sheet pile only, and both in the model with an un-cracked superstructure are listed in Table 4.6.

Table 4.6- Load distribution at collapse for un-cracked model

Model	Collapse Live Load (psf)	Percentage of Original Capacity (%)
Battered Piles removed	321	97
Sheet Pile removed	147	45
Both Removed	75	22

In the un-cracked model, removal of the battered piles caused a 3% reduction of the collapse live load. The reactions on the battered piles at collapse of the original un-cracked model represented only 4% of the total reactions. As such, it was found that the presence of the battered piles was not a prominent factor in the resulting capacity of the structure under vertical loads.

Removal of the sheet pile, however, caused a 55% reduction in the capacity of the uncracked model, while this reduction was of 78% when both sheet and battered piles were removed. As shown in Table 4.5, the sheet piles carried 29% of the total load at collapse of the un-cracked model. As such, the presence of the sheet piles was found to be a prominent factor in the resulting capacity of the structure under vertical loads.

Deformed shapes at collapse for these models are presented in Figure 4.23 to Figure 4.25. These figures include the corresponding contours of vertical displacements (in inches).

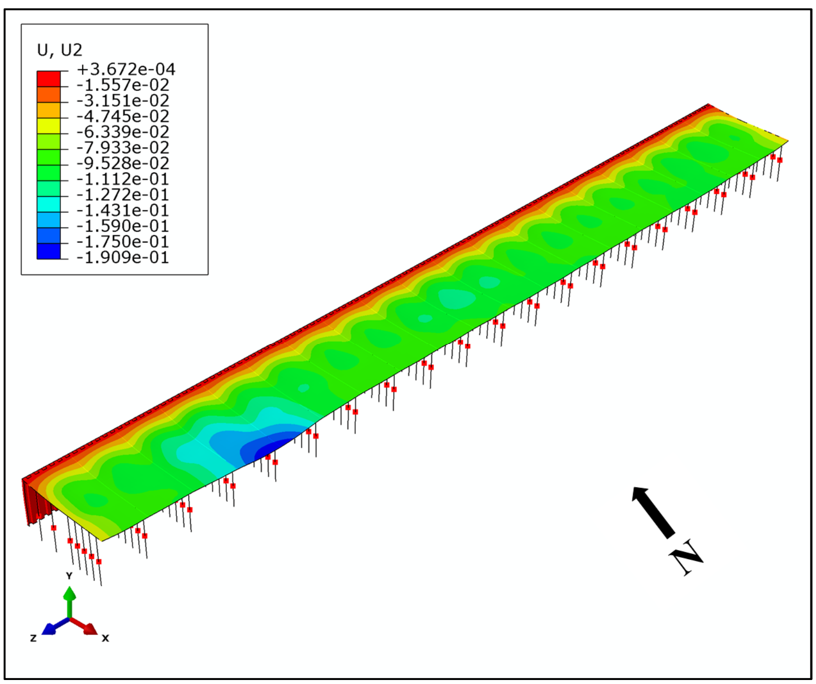

Figure 4.23- Deformed shape – battered piles removed on un-cracked model

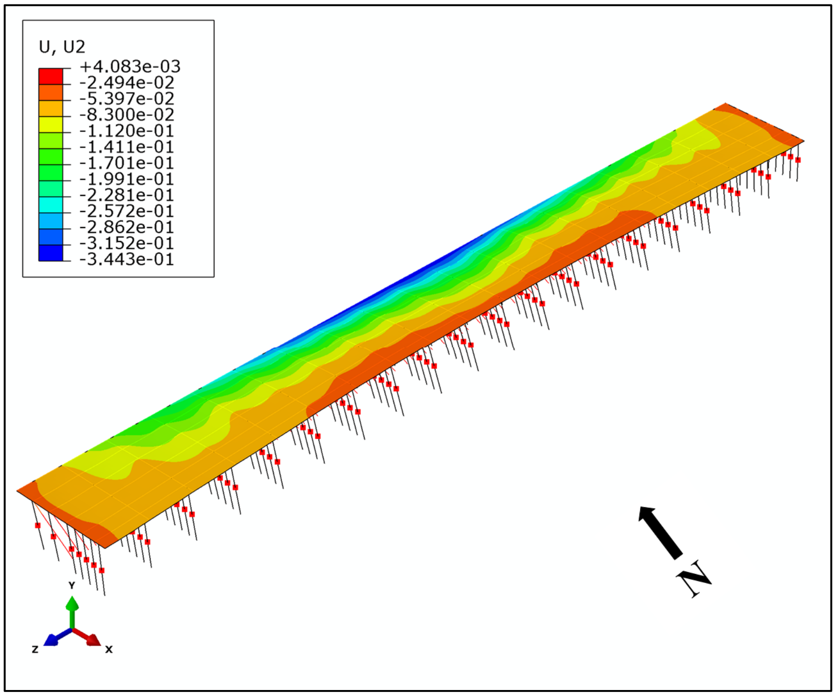

Figure 4.24- Deformed shape – sheet pile removed on un-cracked model

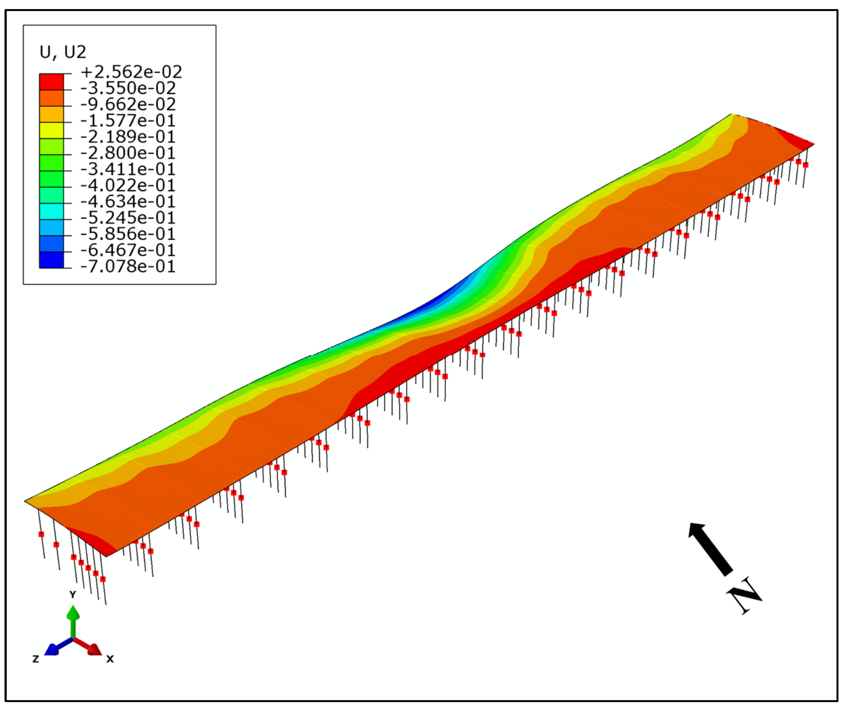

Figure 4.25- Deformed shape – battered piles and sheet pile removed on un-cracked model

Removal of the battered piles did not cause a change in the deformed shape at collapse of the un-cracked model, as shown in Figure 4.23. However, removal of the sheet pile alters the deformed shape at collapse, with the maximum vertical displacements occurring along the G-line, as shown in Figure 4.24 and Figure 4.25. As previously discussed, 30 of the 35 stiffest piles in the model are located in the F-line and G-line. Because the sheet pile represents a significant load-carrying element in the original un-cracked model, the maximum vertical displacements did not occur near the G-line. However, when the sheet pile was removed, the influence of the stiffness of the piles near this section resulted in higher loads on the piles, thus increasing the deformations of the structure along the G-line. The collapse live loads obtained in this study are listed in Table 4.7.

Table 4.7- Load distribution at collapse for cracked model

Model	Collapse Live Load (psf)	Percentage of Original Capacity (%)
Battered Piles removed	183	98
Sheet Pile removed	0	0
Both Removed	0	0

In the model with a cracked superstructure, removal of the battered piles resulted in a capacity reduction of 2%. In this model, the battered piles carried only 2% of the total applied load at collapse. This was consistent with the findings of the analysis of the un-cracked model. Removal of the sheet pile in the cracked model resulted in the general static step not reaching completion. That is, when the sheet pile was removed, the structure collapsed under its self-weight. The deformed shape at collapse of the cracked model with removed battered piles is presented in Figure 4.26. This figure includes the corresponding contour of vertical displacements (in inches).

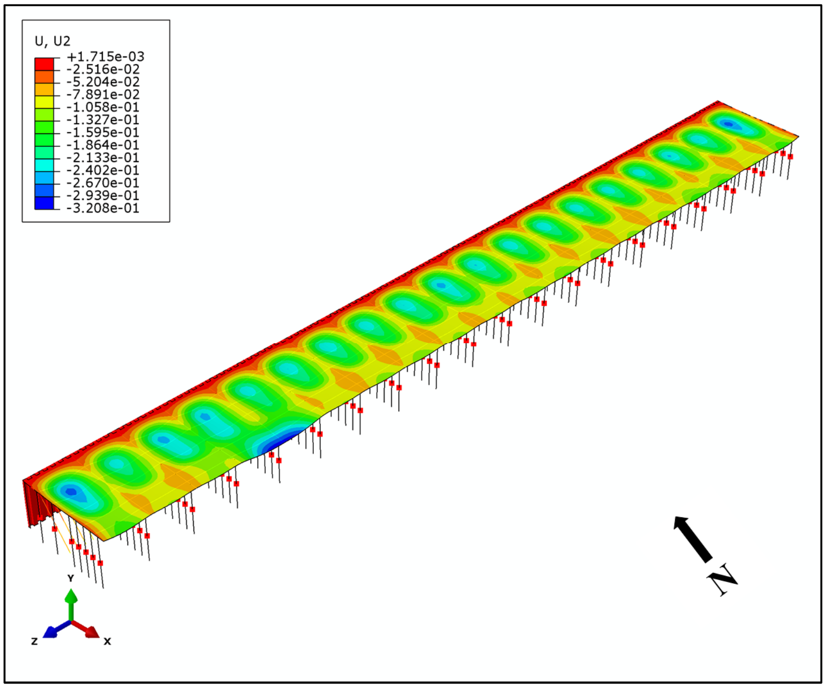

Figure 4.26- Deformed shape – battered piles removed on cracked model

Consistently with the findings of the analysis of the un-cracked model, removal of the battered piles did not alter the deformed shape of the structure at collapse. This section of the study enabled an assessment of the influence of the battered piles and sheet pile on the capacity of the wharf under gravity loads. The determination of the critical elements influencing the collapse capacity of the structure under vertical loading was relevant as it could be helpful in guiding maintenance and repair efforts. However, under different loading configurations, the importance of the structural elements could change. For example, while the battered piles did not significantly contribute to the capacity of the wharf under gravitational loads, they should be a primary factor in the lateral load capacity of the structure. When this type of loading is a concern, it is important that these elements be inspected and modeled rigorously.

4.4.2 Effect of the Superstructure Stiffness

As discussed in the case study of the wharf, there were differences in the capacity and behavior of the models with un-cracked and cracked superstructures. These were triggered by the reduction of the flexural stiffness of the superstructure in the model with a cracked superstructure, as the load redistribution capability of the structure was diminished. As such, a specific analysis of the superstructure stiffness as a factor influencing the load redistribution and collapse performance of the wharf was included in this parametric study. Here, modification factors ranging from 0.10 to 4.00 were applied to the flexural stiffness of the superstructure and evaluated with respect to the resulting collapse live loads and failure modes.

In this section, a modification factor of 1.00 represents the un-cracked model, while a factor of 0.10 corresponds to the cracked model. Modification factors of 0.50 and 0.80 were included to represent intermediate levels of stiffness of the superstructure, as not all concrete sections had necessarily cracked. Finally, modification factors of 1.50, 3.00 and 4.00 were included to study the effect of increasing the stiffness of the superstructure stiffness beyond that of the structure with un-cracked sections. The collapse loads associated with different applied values of the modification factor are listed in Table 4.8.

Table 4.8- Effect of the stiffness of the superstructure

Modification Factor	Collapse Live Load (psf)	Number of Buckled Piles at Collapse
0.10 (Cracked)	186	10
0.50	268	11
0.80	328	13
1.00 (Un-cracked)	330	20
1.50	350	21
3.00	376	22
4.00	419	22

A reduction of the superstructure stiffness by 90% resulted in a 43% loss of load carrying capacity. This represented the assumption of severe cracking in all of the concrete sections of the superstructure. Increasing the stiffness of the superstructure by 300% only resulted in a 27% increase in collapse live load with respect to the original un-cracked structure (modification factor of 1.00). A plot of the relationship between the collapse live load and the stiffness modification factor applied to the superstructure is presented in Figure 4.27.

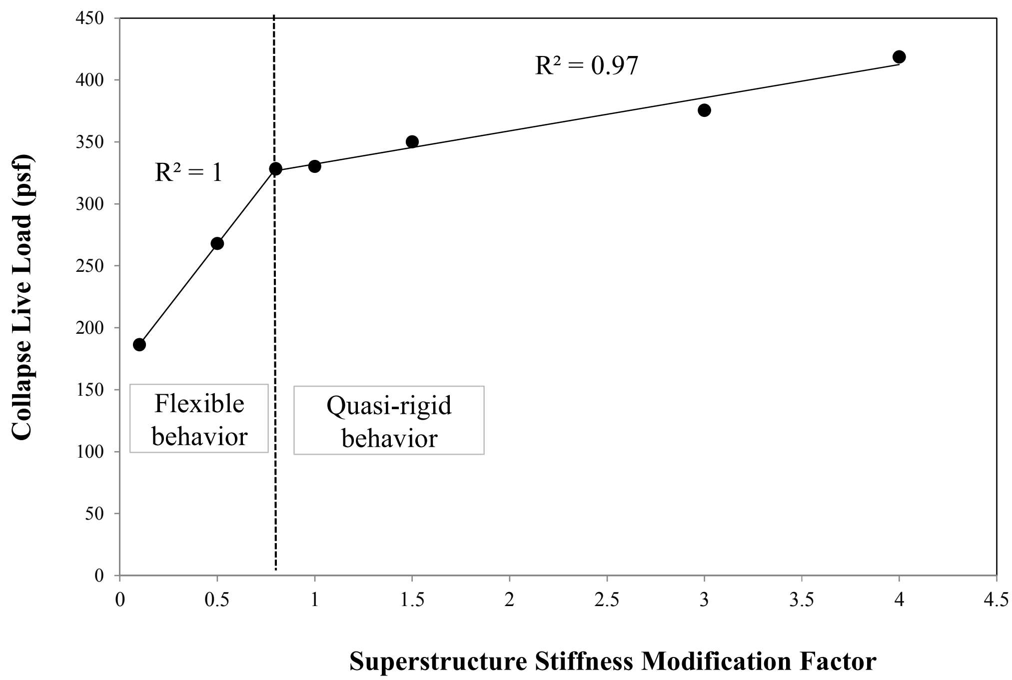

Figure 4.27- Collapse live load vs. superstructure stiffness modification factor

Figure 4.27 shows a bi-linear relationship between the collapse live load and the superstructure stiffness modification factor. Here, the initial trend-line includes the initial three points of the study (modification factors from 0.10 to 0.80), while the final trend-line includes the final five points (modification factors from 0.80 to 4.00). As shown in Figure 4.19 and Figure 4.20, the deformed shape of the un-cracked model displays a quasi-rigid behavior that enabled load redistribution, while the increased flexible behavior of the cracked model indicates the contrary. Additionally, Figure 4.27 shows that this transition begins at a stiffness level of the superstructure corresponding to a modification factor of 0.80. To illustrate the influence of the superstructure stiffness on the collapse mechanism of the structure, the corresponding D/D_{peak} plots at collapse are presented for the different modification factors in Figure 4.28 to Figure 4.32. These plots are not presented for modification factors of 1.00 and 0.10 in this section, as they are depicted in Figure 4.19 and Figure 4.20, respectively.

N

D/D_{peak}

	1	**2**	**3**	**4**	**5**	**6**	**7**	**8**	**9**	**10**	**11**	**12**	**13**	**14**	**15**	**16**	**17**	**18**	**19**	**20**
G	0.13	0.24	0.17	0.49	0.27	0.26	0.36	0.32	0.37	0.34	0.30	0.38	0.19	0.32	0.24	0.27	0.28	0.46	0.14	0.18
F	0.18	0.68	0.55	0.91	0.56	0.85	0.51	0.38	0.26	0.60	0.85	0.72	0.48	0.42	0.28	0.33	0.52	0.86	0.47	0.34
E	0.16	0.95	0.48	1.84	0.79	0.99	0.54	0.38	0.38	2.14	1.14	0.55	0.55	0.66	0.36	0.38	0.36	0.52	0.53	0.25
D	0.19	0.80	0.80	1.53	0.78	0.74	0.33	0.26	0.51	0.67	0.94	0.39	0.41	0.53	0.57	0.37	0.40	0.54	0.44	0.21
C	0.14	0.25	0.59	0.76	1.45	1.08	0.43	0.49	0.42	0.66	0.66	0.62	0.43	0.41	0.53	0.51	0.41	0.45	0.46	0.17
B	0.17	0.27	0.58	2.19	1.75	0.83	0.33	0.41	0.64	0.60	0.40	0.58	0.95	0.22	0.30	0.32	0.62	0.65	0.33	0.26
A	0.48	0.57	0.39	0.55	2.63	0.54	0.28	0.53	0.29	0.30	0.43	**1.03**	0.58	0.23	0.34	0.63	1.31	0.28	0.27	0.12

Figure 4.28- D/D_{peak} at collapse for modification factor of 0.50

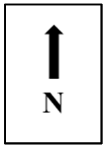

D/D_{peak}

	1	2	3	4	5	6	7	8	9	10	11	12	13	14	15	16	17	18	19	20
G	0.13	0.24	0.17	0.50	0.29	0.27	0.36	0.33	0.38	0.35	0.31	0.39	0.19	0.32	0.24	0.28	0.28	0.46	0.14	0.18
F	0.18	0.68	0.57	0.92	0.61	0.92	0.52	0.39	0.27	0.61	0.87	0.75	0.49	0.43	0.29	0.34	0.53	0.86	0.48	0.35
E	0.17	0.99	0.53	1.92	0.92	**1.15**	0.58	0.41	0.41	2.23	1.20	0.60	0.60	0.71	0.38	0.41	0.39	0.56	0.57	0.27
D	0.21	0.86	0.91	1.64	0.92	0.87	0.36	0.29	0.57	0.71	1.02	0.44	0.46	0.58	0.62	0.41	0.44	0.60	0.48	0.24
C	0.15	0.27	0.67	0.84	1.68	1.29	0.49	0.54	0.46	0.72	0.73	0.71	0.49	0.46	0.59	0.57	0.46	0.50	0.50	0.19
B	0.19	0.30	0.67	2.47	1.98	1.00	0.37	0.46	0.72	0.68	0.46	0.67	**1.08**	0.24	0.33	0.36	0.70	0.75	0.36	0.29
A	0.53	0.63	0.46	0.64	2.92	0.65	0.32	0.58	0.33	0.34	0.50	1.19	0.66	0.25	0.38	0.70	1.46	0.33	0.29	0.13

Figure 4.29- D/D_{peak} at collapse for modification factor of 0.80

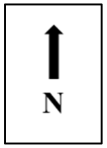

D/D_{peak}

	1	2	3	4	5	6	7	8	9	10	11	12	13	14	15	16	17	18	19	20
G	0.12	0.21	0.16	0.52	0.37	0.34	0.35	0.30	0.35	0.32	0.28	0.36	0.18	0.30	0.22	0.26	0.26	0.41	0.13	0.17
F	0.17	0.60	0.55	0.98	0.87	**1.24**	0.52	0.36	0.25	0.56	0.78	0.70	0.46	0.40	0.27	0.32	0.50	0.78	0.43	0.33
E	0.17	0.92	0.55	2.22	**1.49**	1.85	0.66	0.39	0.41	2.11	1.14	0.61	0.60	0.70	0.38	0.41	0.40	0.55	0.54	0.27
D	0.23	0.83	0.98	2.01	**1.52**	**1.51**	0.44	0.29	0.57	0.70	**1.00**	0.46	0.47	0.60	0.64	0.43	0.46	0.62	0.48	0.25
C	0.17	0.27	0.75	**1.08**	2.74	2.36	0.63	0.54	0.47	0.74	0.74	0.76	0.52	0.48	0.62	0.60	0.49	0.53	0.51	0.21
B	0.21	0.30	0.78	3.30	3.17	**1.94**	0.51	0.47	0.75	0.72	0.49	0.72	1.17	0.26	0.35	0.38	0.74	0.81	0.38	0.33
A	0.59	0.64	0.55	0.89	4.58	**1.33**	0.46	0.61	0.34	0.38	0.55	1.30	0.72	0.28	0.41	0.76	1.54	0.36	0.31	0.15

Figure 4.30- D/D_{peak} at collapse for modification factor of 1.50

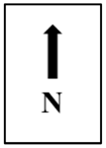

D/D_{peak}

	1	2	3	4	5	6	7	8	9	10	11	12	13	14	15	16	17	18	19	20
G	0.11	0.19	0.16	0.49	0.35	0.30	0.33	0.28	0.32	0.29	0.25	0.34	0.17	0.27	0.21	0.24	0.24	0.37	0.11	0.15
F	0.16	0.55	0.55	0.92	0.80	1.10	0.50	0.34	0.24	0.51	0.71	0.67	0.44	0.38	0.25	0.30	0.48	0.72	0.38	0.31
E	0.18	0.91	0.59	2.13	1.36	1.67	0.68	0.40	0.41	2.03	1.11	0.63	0.62	0.71	0.39	0.42	0.41	0.55	0.53	0.29
D	0.24	0.85	**1.10**	1.96	1.39	1.39	0.47	0.31	0.59	0.71	1.01	0.49	0.50	0.63	0.67	0.45	0.49	0.64	0.48	0.27
C	0.18	0.28	0.87	1.08	2.50	2.20	0.69	0.61	0.50	0.77	0.79	0.82	0.57	0.52	0.66	0.65	0.52	0.57	0.52	0.24
B	0.24	0.33	0.93	3.38	2.89	1.83	0.58	0.54	0.82	0.79	0.54	0.80	1.30	0.29	0.39	0.42	0.81	0.90	0.40	0.38
A	0.69	0.73	0.66	0.93	4.17	1.28	0.53	0.72	0.39	0.43	0.63	1.46	0.82	0.32	0.47	0.85	1.70	0.41	0.34	0.19

Figure 4.31- D/D_{peak} at collapse for modification factor of 3.00

N

D/D_{peak}

	1	2	3	4	5	6	7	8	9	10	11	12	13	14	15	16	17	18	19	20
G	0.11	0.19	0.16	0.49	0.35	0.30	0.33	0.27	0.31	0.28	0.25	0.33	0.16	0.27	0.20	0.24	0.24	0.36	0.11	0.15
F	0.16	0.54	0.56	0.92	0.81	1.10	0.51	0.34	0.23	0.49	0.70	0.67	0.44	0.37	0.25	0.30	0.47	0.70	0.37	0.31
E	0.18	0.92	0.62	2.17	1.38	1.70	0.71	0.42	0.41	2.03	1.12	0.64	0.63	0.73	0.39	0.43	0.42	0.55	0.53	0.29
D	0.25	0.87	1.16	2.02	1.41	1.43	0.50	0.32	0.61	0.72	1.03	0.51	0.52	0.65	0.69	0.46	0.50	0.66	0.48	0.28
C	0.19	0.29	0.93	1.13	2.54	2.27	0.74	0.64	0.52	0.80	0.81	0.86	0.59	0.54	0.69	0.68	0.54	0.59	0.54	0.25
B	0.26	0.35	1.00	3.54	2.95	1.90	0.62	0.58	0.86	0.83	0.57	0.84	1.37	0.31	0.42	0.44	0.85	0.94	0.42	0.41
A	0.74	0.78	0.72	0.98	4.26	1.33	0.58	0.77	0.41	0.46	0.67	1.55	0.86	0.34	0.50	0.90	1.79	0.44	0.36	0.20

Figure 4.32- D/D_{peak} at collapse for modification factor of 4.00

The previous figures show the progression of the collapse mechanism as stiffness of the superstructure was increased. In these, the highlighted cells represent buckled piles, while bolded cells represent buckled piles that had not reached their peak capacity for the previous modification factor. The behavior assessment based on the bi-linear relationship presented in Figure 4.27 was validated as the number of buckled piles increased with the stiffening of the superstructure, indicating enhanced load redistribution. Consistently with the analyses of un-cracked and cracked models, progressive buckling of proximate piles was displayed, as new buckled piles were generally adjacent to those which had previously reached their capacity. Finally, the progression of the number of buckled piles presented in Table 4.8 confirmed the suggested transition point for the behavior of the superstructure.

For a modification factor of 0.10 (cracked concrete sections), the number of buckled piles at collapse was 10. Increasing the modification factor to 0.50 only resulted in one additional pile reaching its peak capacity. This showed that flexible behavior of the superstructure at these stiffness levels, hindered the structure's capability to redistribute the load away from buckled piles, resulting in lower collapse loads and fewer piles reaching their peak capacity. For a modification factor of 1.00, the number of buckled piles reached 20, indicating that the behavior of the superstructure had transitioned into a quasi-rigid behavior mode that enabled further load redistribution and increased capacity. However, as the modification factor was further increased, the maximum number of buckled piles only reached 22, indicating an inherent limit to the load redistribution capabilities of the wharf superstructure.

4.4.3 Effect of the Redundancy of Supporting Elements

The large number of vertical piles provided a high degree of static indeterminacy of the structure. As such, there were multiple paths for load redistribution. This was particularly relevant since the superstructure had the capacity to redistribute load to adjacent piles after one or a small number of piles buckled in a localized region. As such, the effect of the number of piles and the distance between pile-rows was studied as a parameter influencing the capacity of the structure, and presented in this section. For this study, three models were created in which the structural redundancy of the substructure was decreased by removal of pile-rows, as presented in Figure 4.33 to Figure 4.35.

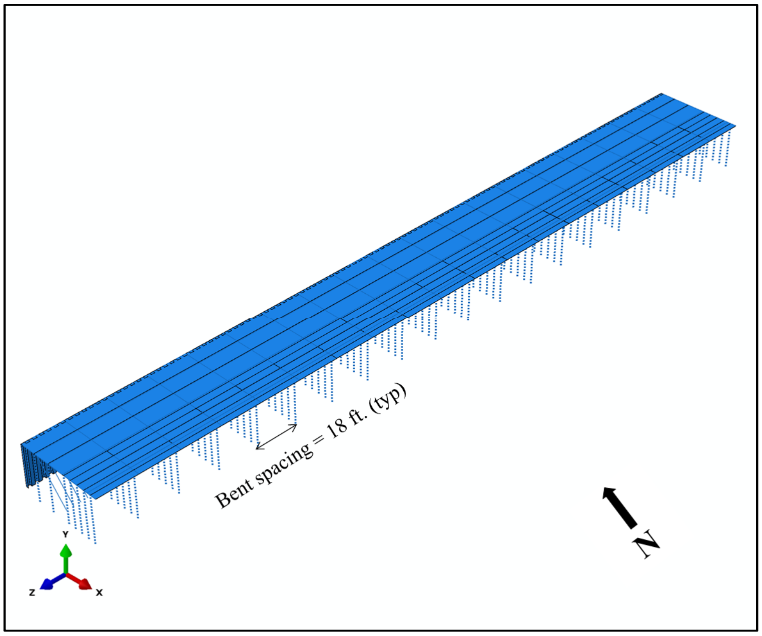

Figure 4.33- Redundancy study: 18 ft. spacing

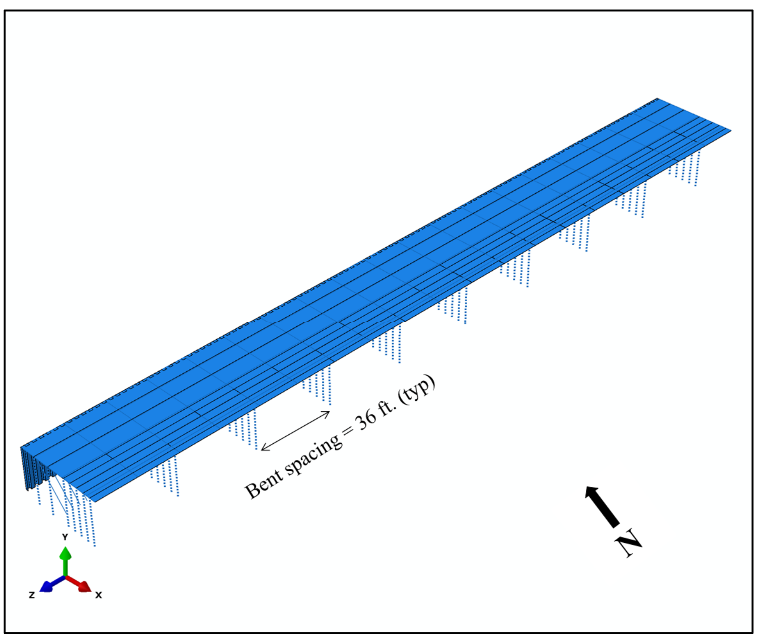

Figure 4.34- Redundancy study: 36 ft. spacing

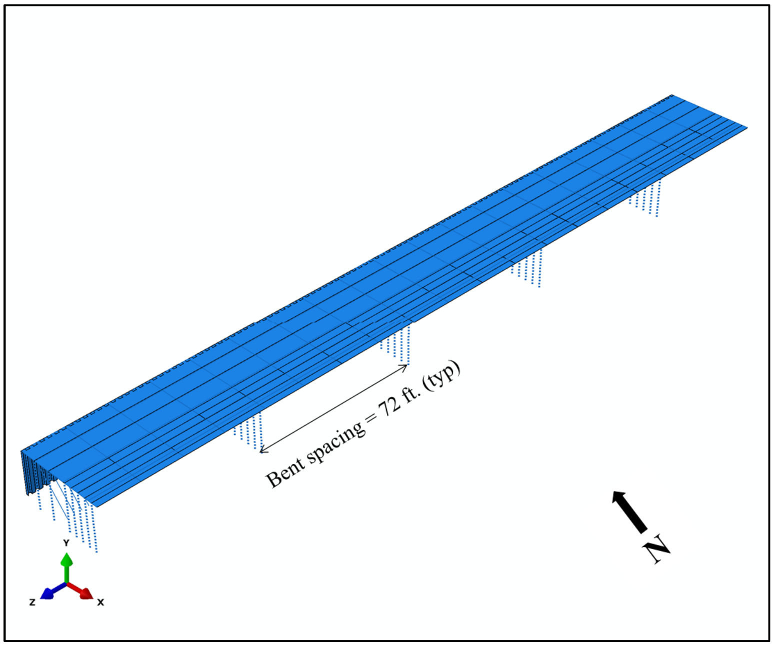

Figure 4.35- Redundancy study: 72 ft. spacing

As shown in the previous figures, three different spans between pile-rows were evaluated. The first model corresponds to the original structural configuration, with an 18 ft. span and 140 total piles. In the second, the removal of pile-rows results in a span of 36 ft. and 70 total piles. Finally, the span of the third model was of 72 ft., and included 35 vertical piles.

The cumulative capacity and stiffness of the vertical piles in the original structural configuration was maintained in order to evaluate the effect of the removal of piles on the load redistribution capability of the wharf, while keeping a constant strength and stiffness contribution from the vertical piles in each model. That is, the axial forces in the simplified axial load vs. shortening relationships of the remaining piles were multiplied by a factor equal to ΣP_0 / $\Sigma P_{reduced}$. Where ΣP_0 is the sum of the capacities of all of the piles in the original wharf model, while $\Sigma P_{reduced}$ is the sum of the pile capacities in the model with the reduced number of piles. This has the effect of ensuring that the total vertical load carrying capacity of the remaining piles is equal to that of the original wharf while the total stiffnesses are comparable. This allows investigation of the influence of the pile redundancy on the wharf capacity independently from the cumulative capacity of the piles. The ratio of the cumulative capacity of vertical piles in the original structural configuration to that of the model with 36 ft. span length was 1.90. This ratio was 3.92 for the model with 72 ft. pile spacing. An illustration of the corresponding scaling of the load-shortening relationships of the piles for the models with 36 ft. and 72 ft. is presented in Figure 4.36.

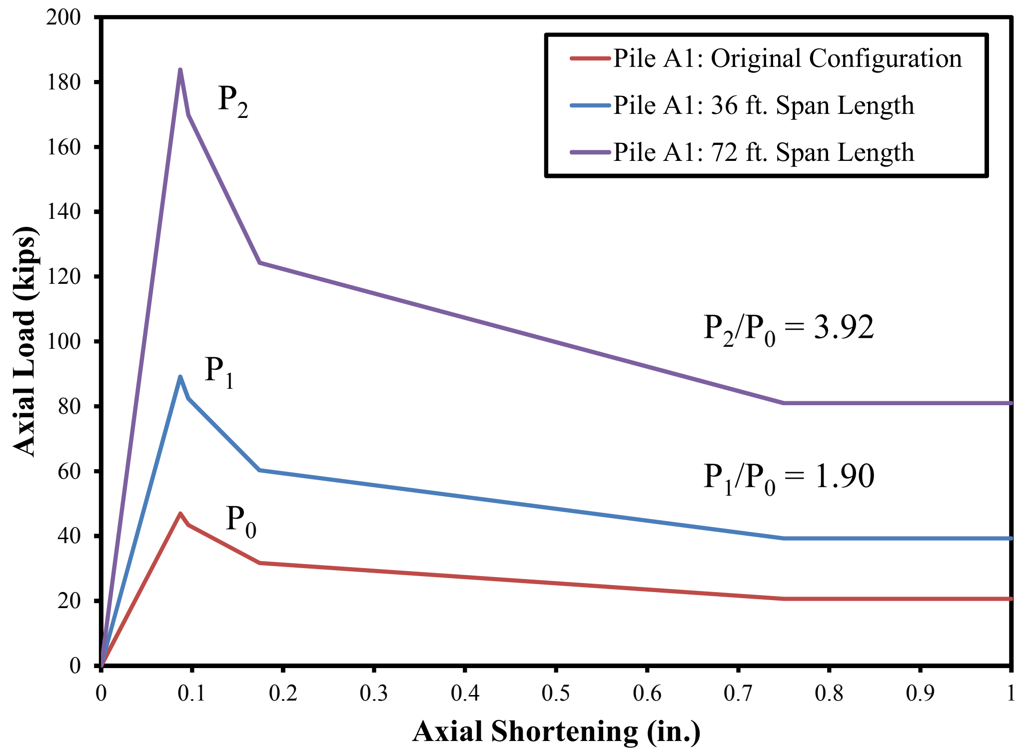

Figure 4.36- Scaling of pile A1 load-shortening relationship

As shown in Figure 4.36, the load-shortening relationship of each pile was scaled using the corresponding ratio of the cumulative capacity of vertical piles. This enabled the strength and stiffness contribution from the vertical piles to be constant, even as the number of piles was decreased.

Because increasing the span length affected the load redistribution capabilities of the wharf not only by decreasing the degree of static indeterminacy, but by the reduction of flexural stiffness of the superstructure, the analysis was conducted for un-cracked and cracked assumptions of the concrete elements. As some of the models could reach collapse under self-weight loads, only the Riks step was performed in these simulations. These rendered the maximum uniform load that could be carried by each structural configuration, without accounting for self-weight effects. The self-weight of the structure, previously determined to be 6178 kips, corresponds to a uniformly distributed load of 452 psf.

The collapse loads found for the different configurations analyzed in this study are presented in Table 4.9. The relationship of these loads and the corresponding span lengths for the un-cracked and cracked models is presented in Figure 4.37.

Table 4.9- Effect of redundacy of supporting elements

Model	Span Length (ft.)	Collapse Load (psf)
Un-cracked	18	690
	36	649
	72	517
Cracked	18	502
	36	410
	72	185

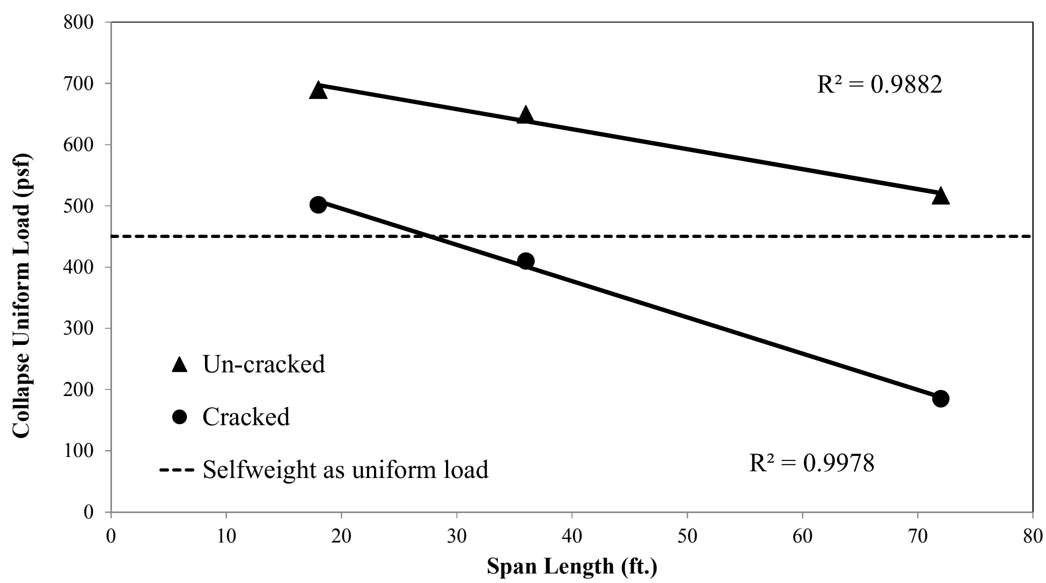

Figure 4.37- Collapse live load vs. span length

The collapse loads presented in Table 4.9 do not include self-weight effects. In the models with un-cracked superstructures, increasing the span length to 72 ft. resulted in a 25% reduction of capacity with respect to the original configuration. This reduction was found to be 63% in the models with a cracked superstructure. The difference is reflected in the slopes of the trend-lines presented in Figure 4.37. In this figure it is shown that while the un-cracked models had sufficient superstructure stiffness to redistribute loads even as the number of piles decreased, the cracked models were dependent on a high number of closely positioned piles to render their load redistribution capabilities. When the number of piles was reduced, and the distance between them increased, the performance of the structure was severely compromised. In Figure 4.37, the dotted line represents the self-weight of the structure as a uniform load of 452 psf. Here it is seen that increasing the span length to 36 ft. induces collapse of the cracked models at loads lower than the estimated self-weight.

These findings showed that the collapse load of the structure was affected by the reduction of the number of piles even as the cumulative strength and stiffness of the substructure was maintained. Additionally, it was found that the influence of the degree of static indeterminacy of the structure on its load redistribution capability was magnified in cases of low stiffness of the superstructure. Finally, the behavior of the un-cracked models displayed in Figure 4.37 demonstrated that if sufficient superstructure stiffness can be achieved, the total number of piles may be reduced without significantly hindering the performance of the wharf.

4.4.4 Effect of the Distribution of Corroded Piles

As previously discussed, the inspection of the wharf could only be performed from bent 1 to bent 20, for safety considerations. Consequently, the extent of corrosion on the piles in bents 21 to 40 was not assessed. In order to achieve a comprehensive evaluation of the performance of the structure, it was necessary to estimate the capacity of the section of the wharf for which piles were not inspected. Because the correlation studies presented in Chapter 3 indicated no influence of the pile's location on their degree of corrosion degradation, the effect of randomizing the distribution of corroded piles was analyzed in this study.

A pile's elastic stiffness, however, was influenced by its location, as discussed in Chapter 3. In order to study the effects of different distributions of corroded piles in a manner that appropriately represented the variability in pile capacity while maintaining the stiffness distribution of the original structural configuration, the order of pile rows was randomized. In this way, the distribution of pile capacities within the structure was randomized, while the stiffness distribution was similar to that of the original structure.

Because of the influence of the stiffness of the superstructure on the load redistribution capability and performance of the wharf, this procedure was conducted for three levels of superstructure stiffness. The first corresponds to the structure with un-cracked concrete sections and gross-cross-sectional properties. The second represents the superstructure as being fully cracked, by the application of a stiffness modification factor of 0.10, as determined in Appendix H. The third represents an intermediate level of the superstructure stiffness, and approximately corresponds to a level of loading such that

$$\frac{w_{applied}}{w_{cracking}} = 1.30 \tag{4-1}$$

in the longitudinal beams idealized with simply supported boundary conditions. The stiffness modification factor for this case was 0.50, and was determined based on the effective moment of inertia of the longitudinal beams for the load level shown in Equation (4-1). These calculations are also presented in Appendix H.

The number of permutations for 20 pile rows is 2.43×10^{18}. For the purposes of this study, this was considered an infinitely large population. As such, the minimum number of simulations such that the mean of the resulting collapse loads was approximately that of the total population was calculated.

According to Montgomery, et al. (1998), for sample sizes greater than 30 ($n > 30$), the sample variance, s^2, approximates the population variance σ^2. As such, to calculate te minimum required number of simulations necessary to perform hypotheses testing on the means, the variance after 100 simulations was input, along with a 95% confidence level and a margin of error of 10 psf into Equation (4-2), presented by (Montgomery, et al., 1998), and given as

$$n = \left(\frac{z_{\alpha/2}\sigma}{E} \right)^2, \tag{4-2}$$

where z is the upper $100_{\alpha/2}$ percentage point of the standard normal distribution, α is 5% for a 95% confidence level, σ is the population standard deviation and E is the selected margin of error.

In Equation 4.1, the calculated sample size represents the required number of simulations such that there is 95% confidence in the mean of the resulting collapse loads being within 10 psf of the mean of the total population of collapse loads. This equation is approximately valid independently of the underlying probability distribution of the population. Specifically, it could be used to determine the sample size for populations that are not normally distributed (Montgomery, 1998). The minimum number of simulations was determined to be 160 for the model with un-cracked concrete sections (superstructure stiffness modification factor of 1.00), 168 for the model with an applied superstructure stiffness modification factor of 0.50, and 147 for the model with an applied superstructure stiffness modification factor of 0.10 (fully cracked concrete sections).

To generate a comprehensive data set, 1000 different random configurations were generated for each model. In these analyses, the reported collapse loads did not include self-weight effects. That is, only the Riks method was implemented in order to obtain collapse load results in all the simulations, as some models could reach collapse under self-weight. Subsequently, the fit of the distribution of collapse loads to a normal distribution was studied.

The corresponding cumulative distribution functions (CDF) are compared to those of a normal distribution with the same mean and standard deviation. These plots are presented in Figure 4.38 to Figure 4.40.

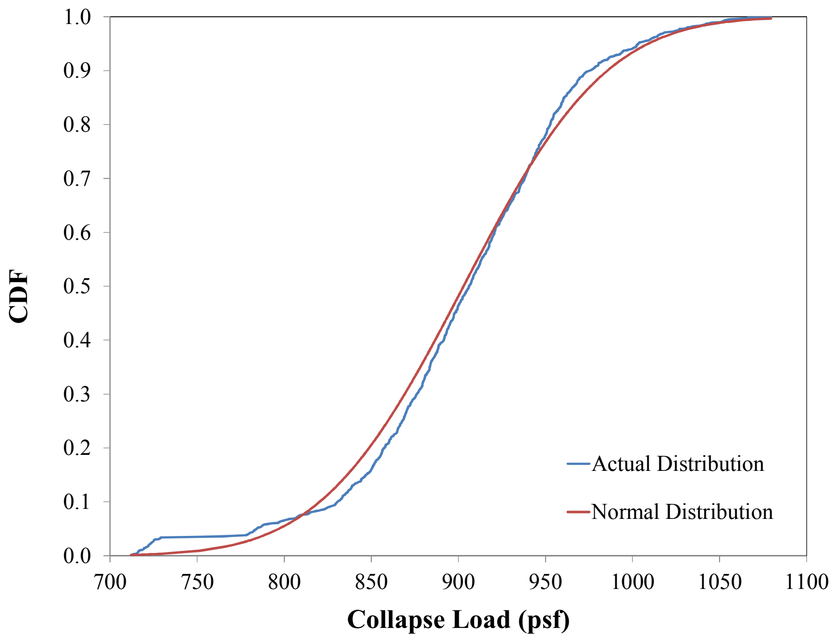

Figure 4.38- CDF for model with un-cracked concrete sections

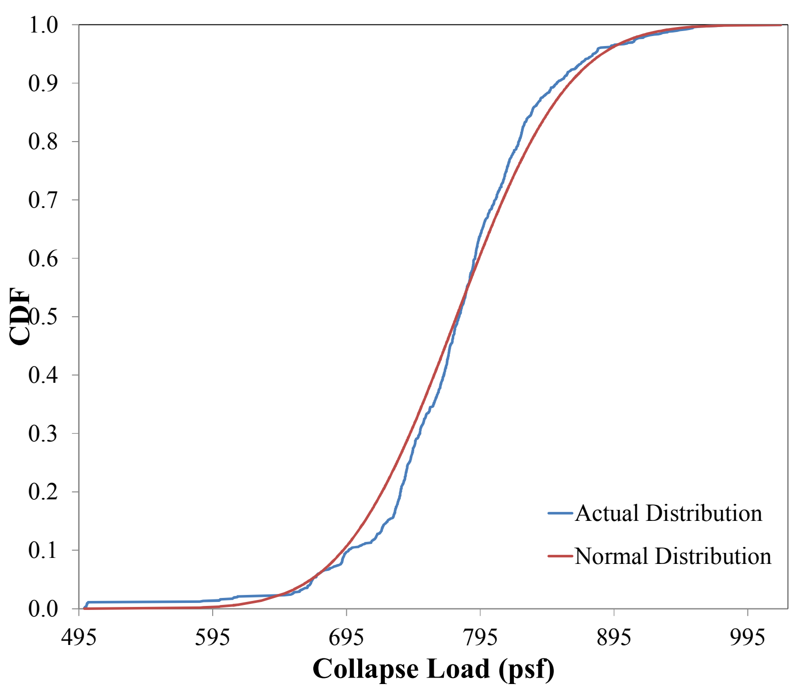

Figure 4.39- CDF for model with stiffness modification factor of 0.50

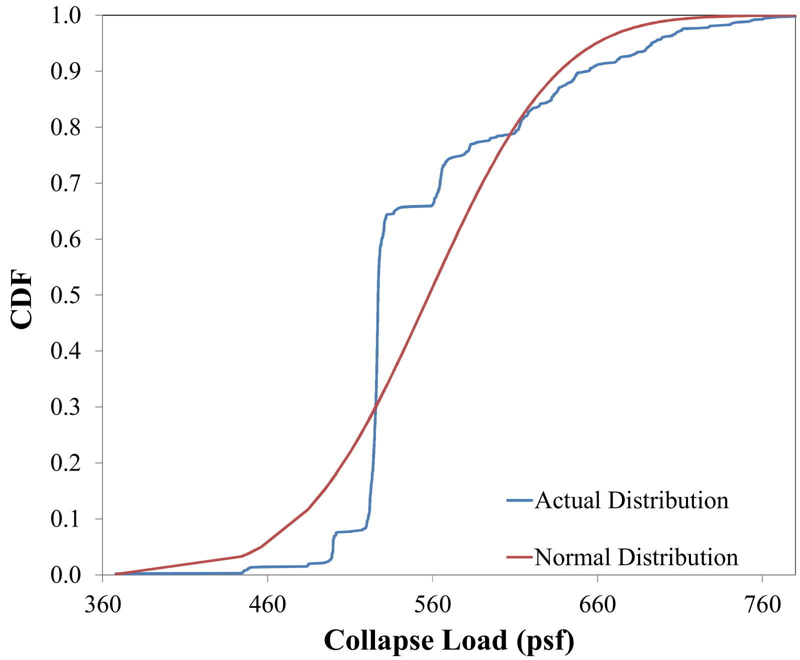

Figure 4.40- CDF for model with fully cracked concrete sections

The qualitative assessment of these plots indicates that the fit of the collapse load distributions to a normal distribution worsens as the stiffness of the superstructure decreases. For the model with un-cracked concrete sections and that with an applied superstructure stiffness modification factor of 0.50, the data shows a reasonable fit to a normal distribution. In contrast, qualitative analysis gives the conclusion that the collapse loads for the model with fully cracked concrete sections do not follow a normal distribution.

Furthermore, the goodness-of-fit test based on the chi-square distribution was conducted as presented by Montgomery, et al. (1998). The test statistic for this method is presented in Equation (4-3), and given as

$$X_0^2 = \sum_{i=1}^{k} \frac{(O_i - E_i)^2}{E_i}, \tag{4-3}$$

where k is the number of bins in the histogram, O_i is the number of occurrences of values within the i[th] bin and E_i is the expected number of occurrences of values within the i[th] bin according to the hypothesized probability distribution. In the present study, this was the normal distribution.

If the population followed a normal distribution, then X_0^2 would fit a chi-square distribution with k–p–1 degrees of freedom. In this case, if Equation (4-4) is met, the hypothesis that the data follow a normal distribution could not be negated. This condition is given by

$$X_0^2 < X_{\alpha,k-p-1}^2 , \tag{4-4}$$

where p corresponds to the number of parameters determined through the sample and α corresponds to 5% for a 95% confidence level.

In this test, two parameters were determined using the sample. These were the sample mean and standard deviation. As such, p = 2.

For the capacity distribution of the models with un-cracked concrete sections, the histogram consisted of 8 bins (k = 8). The corresponding value of $X_{0.05,5}^2$ was 11.07. However, X_0^2 was found to be 80. As such, it was concluded that the capacity distribution does not follow a normal distribution.

For the capacity distribution of the models with a superstructure stiffness modification factor of 0.50, the histogram consisted of 12 bins (k = 12). The corresponding value of $X_{0.05,9}^2$ was 16.92. However, X_0^2 was found to be 157. As such, it was concluded that the capacity distribution does not follow a normal distribution.

For the capacity distribution of the models with fully cracked concrete sections (superstructure stiffness modification factor of 0.10), the histogram consisted of 9 bins (k = 9). The corresponding value of $X_{0.05,6}^2$ was 14.07. However, X_0^2 was found to be 555. As such, it was concluded that the capacity distribution does not follow a normal distribution. The histograms employed for this goodness-of-fit test are presented in Figure 4.41.

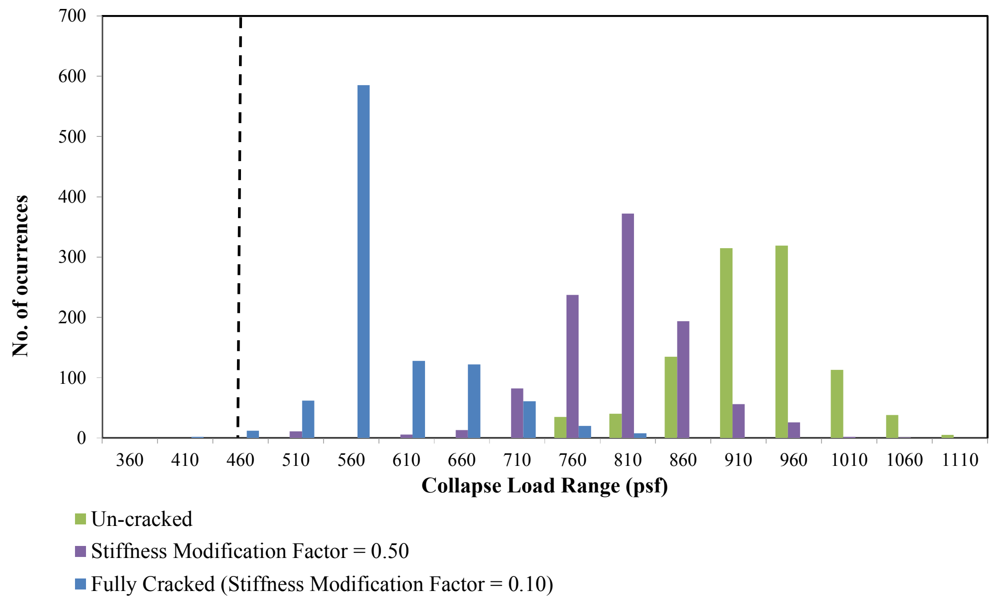

Figure 4.41- Capacity Histograms

As shown in these histograms, the collapse load generally exceeds the self-weight represented as a uniform load. The simulations for the model with fully cracked concrete sections rendered 13 instances where the collapse load was below 452 psf. That is, the simulations rendered a 1.3% probability of failure of the structure under its self-weight. For the higher levels of superstructure stiffness, there were no instances of collapse of the structure under its self-weight. Additionally, the histograms also reflect the worsening of the fit of the distributions to a normal distribution for lower levels of stiffness of the superstructure, as highlighted by the peak in the 560 psf bin of the histogram for the fully cracked models. The statistical information with regards the collapse loads found for the corresponding simulations is presented in Table 4.10.

Table 4.10- Sample statistical information for simulations

Superstructure Stiffness Modification Factor	Number of Simulations	Minimum Collapse Load (psf)	Maximum Collapse Load (psf)	Mean Collapse Load (psf)	Standard Deviation (psf)
1.00	1000	712	1080	902	65
0.50	1000	499	1020	777	66
0.10	1000	368	787	558	62

As previously mentioned, the mean collapse loads presented in Table 4.10 do not account for self-weight. As such, the corresponding mean collapse live loads were determined by deducting the self-weight represented as a 452 psf uniform load from the mean collapse loads presented in the table. Doing this, the mean collapse live loads were determined to be 450 psf for the model with un-cracked concrete sections (superstructure stiffness modification factor of 1.00), 325 psf for the model with a superstructure stiffness modification factor of 0.50, and 106 psf for the model with fully cracked concrete sections (superstructure stiffness modification factor of 0.10).

Even as the populations were not characterized as normally distributed, the mean and standard deviation values found in this study could be considered to approximate those of their respective populations. Analyses of the structure under the assumption of gross, un-cracked sections were included throughout this chapter to represent the ideal performance of the current configuration. However, for safety considerations, the applicable values for assessment of the performance and behavior of the wharf were those corresponding to the models under the assumption of cracked concrete sections. As such, the collapse live load estimation for the section of the wharf with unknown vertical pile distribution was determined to be 40 psf, representing the mean value of collapse live loads minus one standard deviation. In the analyses where the concrete sections were assumed to be fully-cracked (stiffness modification factor of 0.10), the collapse load was below 40 psf in 2% of the simulations. For the assumptions of higher superstructure stiffness, the collapse live loads were never below 40 psf.

Chapter 5 : Summary, Conclusions, and Recommended Future Work

This chapter summarizes the primary conclusions of the numerical studies that were conducted in order (i) to develop a numerical framework to predict the collapse load of highly redundant structures with stiff superstructures under vertical (gravity) loads considering the instability of severely corroded steel H-piles as the predominant failure mode, and (ii) to investigate the influence of sheet and battered piles, stiffness of the superstructure, redundancy of supporting elements and distribution of corroded piles on the performance of wharf structures.

5.1 Summary and Conclusions

A numerical framework was developed to conduct the structural evaluation of the USS Salem Wharf under gravity loads and to perform a parametric study to assess the principal factors influencing the performance of highly redundant structural systems with stiff superstructures.

Because the vertical steel piles were considered critical elements of the structure, and they had suffered severe localized corrosion, the numerical framework developed by Shi, et al. (2015) was used to determine the axial load-shortening relationships, peak capacities, and failure modes of the individual piles.

Furthermore, as collapse of the substructure caused by gravity loads on the structure was the primary safety concern, a non-linear finite element model that incorporated the softening behavior of the heavily corroded sub-structural elements was developed in ABAQUS v.6.12 (SIMULIA, 2012). This model incorporated geometric and material non-linearity, and used the modified Riks method to compute the maximum uniform live load that could be applied prior to collapse. The field data necessary for the development of this numerical framework and implementation of this case study were provided by Simpson Gumpertz & Heger, Inc. (SGH), along with their sub-consultant, Appledore Marine Engineering, Inc. (AMEI). Inspection data were available for the piles under the first half of the wharf (from pile lines 1 to 20). These data were used to model half of the structure and to study in detail the collapse behavior of that half of the structure including a parametric study. Further, a random distribution of pile lines was used to investigate the influence of the stochastic nature of corrosion (which is a natural process) on the possible collapse load.

This numerical framework was used as the basis for a parametric study performed to assess the critical parameters defining the behavior of similar wharf structures. Moreover, it intended to provide information regarding the performance of the part of the USS Salem Wharf for which pile geometry information was not available. The main parameters included in this study were the presence of sheet and battered piles, stiffness of the superstructure, redundancy of supporting elements and distribution of corroded piles. The findings of these studies resulted in the following conclusions:

- The peak capacity of the corroded steel piles did not correlate well to the pile lengths although the capacities were often governed by global buckling which is correlated to pile slenderness and, in-turn, length. Since the length of the piles was inherently related to their location, it was concluded that the peak capacity of the piles was not significantly affected by their location.
- The collapse live loads estimated for the un-cracked and cracked assumptions of the concrete superstructure of the USS Salem Wharf were 330 psf and 186 psf, respectively. These results were obtained through analyses that included the pile geometry information provided by SGH and their sub-consultant, AMEI.
- The deformed shape at collapse of the model with an un-cracked superstructure was found to be primarily dependent on the displacements of the piles. In contrast, the deformed configuration at collapse of the model with a cracked superstructure indicated that the deflected shape of the wharf at failure was also influenced by the flexible behavior of the

superstructure between adjacent pile lines. The maximum vertical deflection was in the vicinity of pile A5 in both cases.

- In the model with an un-cracked superstructure, 20 piles reached their peak capacity at collapse, while only 10 piles did so in the model with a cracked superstructure. As such, it was found that more piles are required to buckle to initiate failure of a stiffer structure. This indicates that increasing the stiffness of the superstructure enhanced the load redistribution capabilities of the structure.
- The collapse mechanism was found to be similar for un-cracked and cracked assumptions of the concrete superstructure. This was characterized by progressive buckling of proximate piles, which placed emphasis on the influence of the total number of piles and the distance between them.
- While their importance for the lateral load capacity of the structure is recognized, the impact of removing the battered piles on the collapse live load for the models with un-cracked and cracked superstructures under gravitational loads was negligible. In contrast, removing the sheet pile from the model with an un-cracked superstructure resulted in a 55% reduction of the load-carrying capacity of the wharf. For the model with a cracked superstructure, this resulted in the prediction that the structure would collapse under its self-weight.
- The removal of both sheet and battered piles resulted in a 78% reduction of the collapse live load in the model with an un-cracked superstructure, which also resulted in collapse under self-weight effects for the cracked model. Additionally, removal of the sheet pile influenced the deformed shape at collapse of the model with an un-cracked superstructure. Its removal caused the maximum deflections to shift from the A-line (south) to the G-line (north) of the wharf.

- The stiffness of the superstructure influenced the behavior and performance of the structure through its effects on the wharf's load redistribution capability. A bi-linear relationship between superstructure stiffness and capacity was identified.
- For a modification factor of 0.10 applied to the superstructure stiffness based on un-cracked concrete sections, the maximum collapse live load was found to be 186 psf. Collapse was caused by nine of the piles buckling in a localized region and the deformed shape at collapse indicated flexible behavior of the superstructure. Between the 0.80 and 1.00 modification factors, it was found that the deformed shape at collapse transitioned from flexural to a quasi-rigid behavior of the superstructure. Furthermore, the number of buckled piles at collapse increased from 11 corresponding to a modification factor of 0.80, to 20, corresponding to a modification factor of 1.00.
- Applying a modification factor of 4 to the superstructure stiffness based on un-cracked concrete sections resulted in only a 27% increase of the collapse load, which indicated a limit in the load redistribution capabilities of the wharf superstructure.
- The collapse load of the structure was affected by the reduction of the number of piles even as the cumulative strength and stiffness of the substructure was maintained.
- It was found that the influence of the degree of static indeterminacy of the structure on its load redistribution capability was magnified in cases of low stiffness of the superstructure.
- It was concluded that if sufficient superstructure stiffness can be achieved, the total number of piles may be reduced without significantly hindering the performance of the wharf.
- By randomizing the order of pile-rows and altering the distribution of corroded piles, mean collapse live loads of 450 psf, 325 psf and 106 psf were found for the models with applied superstructure stiffness modification factors of 1.00 (un-cracked concrete), 0.50 and 0.10 (fully cracked concrete), respectively. These values correspond to 1000 simulations performed for each assumption of the superstructure stiffness. Additionally, they provide an

indication of the performance of the part of the wharf for which pile deterioration information is unknown. Because the probability distributions found for the collapse loads did not fit a normal probability distribution, the maximum live load for this section of the structure is recommended to be 40 psf, representing the mean minus one standard deviation of the collapse load distribution for the condition of fully cracked concrete sections in the superstructure. For the corresponding set of 1000 simulations, only 2% of the analyses resulted in collapse live loads below 40 psf.

5.2 Research Limitations and Recommendations for Future Work

The numerical studies presented herein focused on collapse stemming from instabilities in the substructure of the wharf. The principal limitations and assumptions of this research are:

- The geometrical information of the vertical steel piles was only available for piles in bents 1 to 20.
- The performance of the USS Salem Wharf was evaluated only under gravitational loads.
- The degree of deterioration of the battered piles was not accounted for.
- The reinforcement details of the concrete elements of the superstructure were not considered. Instead, gross sections were used. Models assuming un-cracked and cracked conditions of the superstructure were generated. In these analyses, the superstructure stresses at collapse did not exceed the modulus of rupture of concrete.
- In the study of the influence of the redundancy of supporting elements, the stiffness of the superstructure was affected by the increase in span lengths. While the analyses were performed for un-cracked and cracked assumptions of the concrete superstructure, these parameters were not de-coupled.

Based on the principal assumptions and limitations of the current study, there are several avenues that could be pursued to further investigate this subject. As such, the main recommendations for future research are the following:

- The performance of the USS Salem Wharf when subject to lateral loads should be investigated. In these cases it is recommended that the corrosion degradation effects on battered piles be accounted for.
- The investigation of the performance of similar structures for different load configurations, such as patch loads, moving loads, concentrated loads and lateral loads is recommended.
- The investigation of the performance of similar structures with a primary focus on shear, bending and dynamic failure mechanisms is recommended.
- In this study, idealizations were made in the modeling of the concrete superstructure. If these elements are considered critical, a more rigorous representation of them with respect to their geometry, material properties and reinforcement detailing is recommended.

References

AASHTO. (2012). Bridge Design Specifications (LRFD). American Association of State Highway and Transportation Officials.

ACI318. (2014). Building Code Requirement for Structural Concrete. American Concrete Institute.

AISC. (2011). Steel Construction Manual. American Institute of Steel Construction.

AISI. (2012). North American Specification for the Design of Cold-Formed Steel Structural Members. Washington, DC: American Iron and Steel Institute.

ASTM C39-12a (2012). Standard Test Method for Compressive Strength of Cylindrical Concrete Specimens. American Society for Testing and Materials.

ASTM C469-10 (2010). Standard Test Method for Static Modulus of Elasticity and Poisson's Ratio of Concrete in Compression. American Society for Testing and Materials.

Banayan-Kermani, A., Bargi, K. and Heidary-Torkamani, H. (2016). *Seismic Performance Assessment of Pile-Supported Wharves Retrofitted by Carbon Fibre-Reinforced Polymer Composite Considering Ageing Effect*. Advances in Structural Engineering, 19(4), 581-598.

Bedard, M. (2008). Use of New Industrial Coatings for the U.S. Navy Waterfront Structures (Master's Thesis). Monterey, CA: Naval Postgraduate School.

Bhattacharya, S., Dash, S. and Adhikari, S. (2008). *On the Mechanics of Failure of Pile-Supported Structures in Liquefiable Deposits during Earthquakes*. Current Science, 94(5), 605-6011.

Bjorhovde, R. (1972). Deterministic and Probabilistic Approaches to the Strength of Steel Columns (Doctoral Dissertation). Bethlehem, PA: Lehigh University.

Brockenbrough, R.L. (2003). AISC Rehabilitation and Retrofit Guide – A Reference of Historical Shapes and Specifications. AISC Steel Design Series, 15.

Chan, T. M., and Gardner, L. (2008). *Compressive resistance of hot-rolled elliptical hollow sections*. Eng. Struct., 30(2), 522–532.

Chiou, J.S., Chiang, C.H., Yang, H.H., and Hsu, S.Y. (2011). *Developing Fragility Curves for a Pile-Supported Wharf*. Soil Dynamics and Earthquake Engineering, 31, 830-840.

Collins Engineers. (2010). Underwater Bridge Inspection (Report No. FHWA-NHI-10-027). Federal Highway Administration, U.S. Department of Transportation.

Davisson, M. T. and Robinson, K. E. (1965). *Bending and Buckling of Partially Embedded Piles*. Proceedings of the 6th International Conference on Soil Mechanics and Foundation Engineering, 243-246. Montreal, Canada.

Dwakarish, G.S., Akhil, M.S. (2015). *Review on the Role of Ports in the Development of a Nation*. Aquatic Procedia, Vol. 4, 295-301.

Earls, C.J. (2001). *Constant Moment Behavior of High-Performance Steel I-Shaped Beams*. Journal of Construction Steel Research, 57, 711–728.

Essa, H. S., and Kennedy, L. (1993). Distortional Buckling of Steel Beams. Structural

Engineering Report. No. 185, Department of Civil Engineering, Alberta, Canada: University of Alberta.

Galambos, T. (1998). Guide to Stability Design Criteria for Metal Strutures (5th ed.). John Wiley and Sons, Inc.

Gwinn, K.W., Wellman, G.W. and Redmond, J.M. Peer Review of the National Transportation Safety Board Structural Analysis of the I-35W Bridge Collapse. SANDIA Report SAND2008-6206. Albuquerque, New Mexico.

Hanson, K. (2013). Military Ocean Terminals Play Strategic Role in Defense. Extracted from: https://www.army.mil/article/113348/169636.

Heidary-Torkamani, H., Bargi, K., Amirabadi, R. and Mccllough, N.J. (2014). *Fragility Estimation and Sensitivity Analysis of an Idealized Pile-Supported Wharf with Batter Piles*. Soil Dynamics and Earthquake Engineering, 61-62, 92-106.

Jiren, L., Bo, S. and Jianyu, C. (2015). *Seismic Dynamic Damage Characteristics of Vertical and Batter Pile-Supported Wharf Structure Systems*. Journal of Engineering Science and Technology Review. Vol. 8(5), 180-189.

Karagah, H. (2015). FRP-Confined Grout Systems for Underwater Rehabilitation of Corroded Steel Bridge Piles. (Ph.D Dissertation). Houston, Texas. Univesity of Houston.

Montgomery, D. C., Tunger, G. C. and Hubele, N. F. (1998). Engineering Statistics. John Wiley and Sons, Inc.

National Transportation Safety Board (2008). Collapse of I-35W Highway Bridge. Highway Accident Report NTSB/HAR-208/03. Washington, D.C.

Naval Facilities Engineering Command (1992). Corrosion Control. Publication NAVFAC MO-307. NAVFAC, U.S. Department of Defense. New South Wales Government (2015). Guidelines for Evaluation of Public Ferry Wharf Safety. Roads and Maritime Services.

Seif, M. and Schafer, B. W. (2009). *Finite Element Comparison of Design Methods for Locally Slender Steel Beams and Columns.* Proceedings of the Annual Stability Conference, 69-90. Phoenix, AZ.

Shi, C., Karagah, H., Belarbi, A. and Dawood, M. (2015). *Inelastic Buckling Behavior of Steel H-Piles with Localized Severe Corrosion*. Journal of Bridge Engineering, 31(3), 04015069.

Shi, C., Karagah, H., Dawood, M., and Belarbi, A. (2014). *Numerical Investigation of H-shaped Short Steel Piles with Localized Severe Corrosion*. Engineering Structures, 73, 114-124.

Karagah, H., Shi, C., Dawood, M., and Belarbi, A. (2015). *Experimental Investigation of H-shaped Short Steel Columns with Localized Corrosion*. Thin Walled Structures, 87, 191-199.

Schultheisz, C.R., Kushner, A.S., Nakamura, T., Ocel, J., Wright, W. and Li, M. (2008). "Minneapolis I-35W Bridge Collapse – Engineering Evaluations and Finite Element Analyses". From: http://www.simulia.com/download/pdf2010/Schultheisz_SCC2010.pdf

SIMULIA. (2012). ABAQUS User's Manual Version 6.12. Providence, RI: Dassault Systemes Simulia Corporation.

United States Naval Shipbuilding Museum (2016). Extracted from: http://www.uss-salem.org

Xiao, Y. (2004). A two-dimensional stochastic model for prediction of localized corrosion. (Master's Thesis). Athens, OH: Ohio University.

Ziemian, R. D. (2010). Guide to Stability Design Criteria for Metal Structures (6^{th} ed.). John Wiley and Sons, Inc.

APPENDIX A : Unbraced Length of Partially Embedded Piles

The equivalent unbraced length of the partially embedded vertical piles of the USS Salem Wharf was determined based on the clear lengths found in the inspection and the method proposed by Davisson, et al. (1965). In this method, the equivalent unbraced length (L_G) of the pile is given by

$$L_G = L_U + L_S \text{ ,} \tag{A-1}$$

where L_u is the clear length of the pile, and L_S is the effective depth of fixity. That is, the embedment length at which the bottom of the pile can be assumed to be fixed.

The effective depth of fixity, L_S, is given by

$$L_s = S_R \times R, \tag{A-2}$$

where S_R is a non-dimensional parameter dependent on the assumed boundary conditions, clear and relative stiffness of pile and soil. In this method, the pile is assumed to be fixed at the bottom and free at the top. R is a parameter relating the pile and soil stiffness, and is given by

$$R = \sqrt[4]{\frac{EpIp}{k}} \text{ ,} \tag{A-3}$$

where E_p and I_p are the elastic modulus and weak-axis moment of inertia of the pile, respectively. Additionally, k is the modulus of horizontal subgrade reaction, and is given by

$$k = 67S_U \text{ ,} \tag{A-4}$$

where S_u is the undrained shear strength of the soil taken determined to be 1200 psf (Personal communication, P. Schuman, 2016). The final non-dimensional parameter, J_R, represents the clear length of the pile, and is given by

$$J_R = \frac{L_U}{R} \text{ .} \tag{A-5}$$

The relationship between S_R and J_R is presented in Figure A.1, as given by Davisson, et al. (1965). This figure has been re-produced from the original for clarity. A summary of the computations performed to determine the equivalent unbraced length for each pile-line (A to G) is presented in Table A.1.

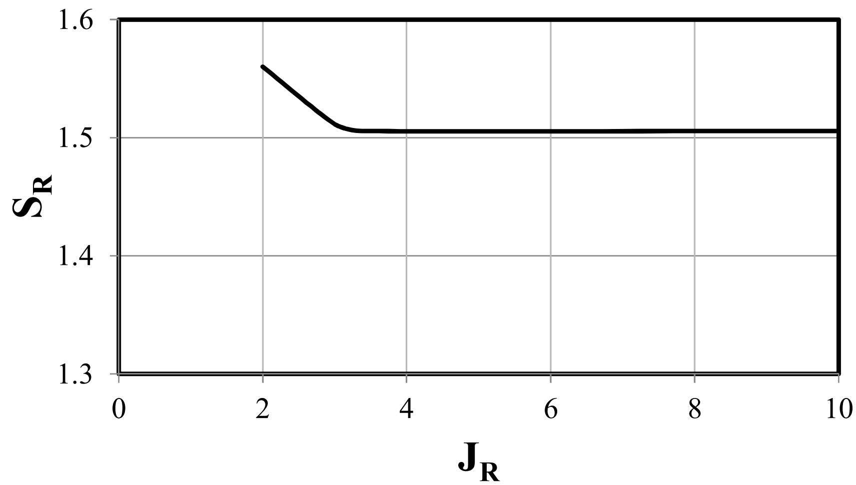

Figure A.1- Depth of fixity for buckling in soils for constant subgrade modulus (Davisson, et al. 1965)

Table A.1- Equivalent unbraced lengths for partially embedded piles

Line	L_U (ft.)	R (ft.)	J_R	S_R	L_S (ft.)	L_G (ft.)
A	29.0	5.1	5.7	1.5	7.6	36.5
B	27.8	5.1	5.5	1.5	7.6	35.5
C	26.5	5.1	5.2	1.5	7.6	34.0
D	25.3	5.1	5.0	1.5	7.6	33.0
E	24.0	5.1	4.7	1.5	7.6	31.5
F	21.0	5.1	4.2	1.5	7.6	28.5
G	19.0	5.1	3.8	1.5	7.6	26.5

APPENDIX B : Pile Field Inspection Data

The geometry information gathered through inspection of 140 vertical piles of the USS Salem Wharf is presented in Table B.1.

Table B.1- Field inspection geometry data

Pile	Length Measurements (in.)				Measurements of Remaining Section at Severely Corroded Region (L_C) (in.)				
	Total Length (L_G)	Top Length (L_T)	Bottom Length (L_B)	Corroded Length (L_C)	Flange Thickness (t_{fc})	Flange Width (b_{fc})	Web Thickness (t_{wc})	Depth (d_c)	Web Void Width (b_{hc})
A1	438	81.0	339	18.0	0.150	4.60	0.230	13.3	N/A
B1	426	81.0	327	18.0	0.170	12.6	0.230	13.3	N/A
C1	408	81.0	309	18.0	0.205	14.6	0.250	13.3	N/A
D1	396	81.0	297	18.0	0.120	12.6	0.270	13.2	N/A
E1	378	81.0	279	18.0	0.200	14.6	0.260	13.3	N/A
F1	342	81.0	243	18.0	0.170	14.6	0.295	13.3	N/A
G1	318	81.0	219	18.0	0.165	14.6	0.285	13.3	N/A
A2*	380	23.0	339	18.0	0.145	10.6	0.130	13.2	N/A
B2	426	81.0	327	18.0	0.190	12.6	0.285	13.3	N/A
C2	408	81.0	309	18.0	0.235	14.6	0.245	13.3	N/A
D2	396	72.0	288	36.0	0.115	6.60	0.250	13.2	N/A
E2	378	72.0	270	36.0	0.125	4.60	0.190	13.2	N/A
F2	342	75.0	237	30.0	0.125	8.60	0.180	13.2	N/A
G2	318	81.0	219	18.0	0.165	14.6	0.260	13.3	N/A
A3*	380	23.0	339	18.0	0.170	8.60	0.225	13.3	N/A
B3	426	81.0	327	18.0	0.120	10.6	0.165	13.2	N/A
C3	408	75.0	303	30.0	0.135	8.60	0.205	13.2	N/A
D3	396	81.0	297	18.0	0.125	6.60	0.170	13.2	N/A
E3	378	78.0	276	24.0	0.190	8.60	0.185	13.3	N/A
F3	342	78.0	240	24.0	0.190	6.60	0.270	13.3	N/A
G3	318	81.0	219	18.0	0.290	14.6	0.240	13.4	N/A
A4	438	81.0	339	18.0	0.170	10.6	0.245	13.3	N/A
B4	426	78.0	324	24.0	0.120	4.60	0.135	13.2	12.0
C4	408	78.0	306	24.0	0.175	10.6	0.145	13.3	N/A
D4	396	75.0	291	30.0	0.165	4.60	0.185	13.3	N/A
E4	378	72.0	270	36.0	0.110	0.600	0.175	13.2	N/A
F4	342	75.0	237	30.0	0.175	6.60	0.130	13.3	N/A
G4	318	75.0	213	30.0	0.175	6.60	0.130	13.3	N/A
A5	438	78.0	336	24.0	0.100	4.60	0.100	13.2	8.00
B5	426	81.0	327	18.0	0.185	4.60	0.130	13.3	3.00

(Table B.1 continued)

Pile	Length Measurements (in.)				Measurements of Remaining Section at Severely Corroded Region (L_C) (in.)				
	Total Length (L_G)	Top Length (L_T)	Bottom Length (L_B)	Corroded Length (L_C)	Flange Thickness (t_{fc})	Flange Width (b_{fc})	Web Thickness (t_{wc})	Depth (d_c)	Web Void Width (b_{hc})
C5	408	78.0	306	24.0	0.200	4.60	0.245	13.3	N/A
D5	396	81.0	297	18.0	0.165	8.60	0.125	13.3	N/A
E5	378	81.0	279	18.0	0.125	10.6	0.165	13.2	N/A
F5	342	81.0	243	18.0	0.200	6.60	0.180	13.3	N/A
G5	318	81.0	219	18.0	0.165	10.6	0.240	13.3	N/A
A6*	380	23.0	339	18.0	0.160	14.6	0.135	13.3	N/A
B6	426	81.0	327	18.0	0.125	6.60	0.180	13.2	N/A
C6	408	72.0	300	36.0	0.120	4.60	0.130	13.2	N/A
D6	396	75.0	291	30.0	0.115	8.60	0.175	13.2	N/A
E6	378	72.0	270	36.0	0.125	4.60	0.175	13.2	N/A
F6	342	72.0	234	36.0	0.115	6.60	0.165	13.2	N/A
G6	318	81.0	219	18.0	0.170	12.6	0.220	13.3	N/A
A7*	380	23.0	339	18.0	0.165	14.6	0.240	13.3	N/A
B7	426	81.0	327	18.0	0.160	14.6	0.200	13.3	N/A
C7	408	81.0	309	18.0	0.135	10.6	0.205	13.2	N/A
D7	396	81.0	297	18.0	0.215	10.6	0.180	13.3	N/A
E7	378	81.0	279	18.0	0.125	10.6	0.205	13.2	N/A
F7	342	81.0	243	18.0	0.175	6.60	0.230	13.3	N/A
G7	318	81.0	219	18.0	0.125	8.60	0.225	13.2	N/A
A8	438	81.0	339	18.0	0.135	14.6	0.115	13.2	N/A
B8	426	81.0	327	18.0	0.180	8.60	0.185	13.3	5.00
C8**	408	81.0	309	18.0	0.245	6.60	0.120	13.3	1.00
D8	396	81.0	297	18.0	0.240	14.6	0.175	13.3	N/A
E8	378	81.0	279	18.0	0.135	10.6	0.230	13.2	N/A
F8	342	81.0	243	18.0	0.195	8.60	0.230	13.3	N/A
G8	318	81.0	219	18.0	0.135	10.6	0.210	13.2	N/A
A9	438	81.0	339	18.0	0.190	14.6	0.210	13.3	N/A
B9	426	81.0	327	18.0	0.120	8.60	0.160	13.2	N/A
C9	408	81.0	309	18.0	0.120	10.6	0.270	13.2	N/A
D9	396	81.0	297	18.0	0.115	13.6	0.190	13.2	N/A
E9	378	81.0	279	18.0	0.120	12.6	0.320	13.2	N/A
F9	342	72.0	234	36.0	0.400	11.6	0.280	13.5	N/A
G9	318	78.0	216	24.0	0.120	10.6	0.180	13.2	N/A
A10*	380	23.0	339	18.0	0.215	10.6	0.195	13.3	N/A
B10	426	81.0	327	18.0	0.170	6.60	0.185	13.3	N/A
C10	408	81.0	309	18.0	0.130	12.6	0.120	13.2	N/A
D10	396	81.0	297	18.0	0.140	14.6	0.125	13.2	N/A
E10	378	69.0	267	42.0	0.100	2.60	0.140	13.2	N/A

(Table B.1 continued)

Pile	Length Measurements (in.)				Measurements of Remaining Section at Severely Corroded Region (L_C) (in.)				
	Total Length (L_G)	Top Length (L_T)	Bottom Length (L_B)	Corroded Length (L_C)	Flange Thickness (t_{fc})	Flange Width (b_{fc})	Web Thickness (t_{wc})	Depth (d_c)	Web Void Width (b_{hc})
F10	342	81.0	243	18.0	0.170	8.60	0.180	13.3	N/A
G10	318	81.0	219	18.0	0.185	10.6	0.150	13.3	N/A
A11*	380	23.0	339	18.0	0.170	14.6	0.120	13.3	N/A
B11	426	81.0	327	18.0	0.170	14.6	0.155	13.3	N/A
C11	408	78.0	306	24.0	0.110	8.60	0.265	13.2	N/A
D11	396	60.0	276	60.0	0.120	4.60	0.135	13.2	N/A
E11	378	72.0	270	36.0	0.115	6.60	0.130	13.2	N/A
F11	342	72.0	234	36.0	0.130	6.60	0.165	13.2	N/A
G11	318	78.0	216	24.0	0.185	8.60	0.215	13.3	N/A
A12	438	81.0	339	18.0	0.175	4.60	0.215	13.3	8.00
B12**	426	81.0	327	18.0	0.190	6.60	0.170	13.3	4.00
C12	408	81.0	309	18.0	0.125	12.6	0.125	13.2	N/A
D12	396	81.0	297	18.0	0.210	8.60	0.165	13.3	N/A
E12	378	81.0	279	18.0	0.180	8.60	0.135	13.3	N/A
F12	342	81.0	243	18.0	0.125	6.60	0.190	13.2	N/A
G12	318	81.0	219	18.0	0.120	10.6	0.185	13.2	N/A
A13	438	81.0	339	18.0	0.125	10.6	0.165	13.2	N/A
B13	426	81.0	327	18.0	0.100	4.60	0.100	13.2	6.00
C13	408	81.0	309	18.0	0.135	12.6	0.195	13.2	N/A
D13	396	81.0	297	18.0	0.175	14.6	0.140	13.3	N/A
E13	378	81.0	279	18.0	0.120	12.6	0.175	13.2	N/A
F13	342	81.0	243	18.0	0.135	10.6	0.210	13.2	N/A
G13	318	81.0	219	18.0	0.185	14.6	0.285	13.3	N/A
A14*	380	23.0	339	18.0	0.295	14.6	0.205	13.4	N/A
B14	426	81.0	327	18.0	0.350	14.6	0.270	13.5	N/A
C14	408	81.0	309	18.0	0.185	12.6	0.120	13.3	N/A
D14	396	81.0	297	18.0	0.140	14.6	0.130	13.2	N/A
E14	378	81.0	279	18.0	0.125	12.6	0.135	13.2	N/A
F14	342	81.0	243	18.0	0.170	14.6	0.170	13.3	N/A
G14	318	81.0	219	18.0	0.155	14.6	0.160	13.3	N/A
A15*	380	23.0	339	18.0	0.190	14.6	0.155	13.3	N/A
B15	426	81.0	327	18.0	0.195	14.6	0.165	13.3	N/A
C15	408	81.0	309	18.0	0.125	14.6	0.145	13.2	N/A
D15	396	81.0	297	18.0	0.115	14.6	0.150	13.2	N/A
E15	378	81.0	279	18.0	0.170	14.6	0.205	13.3	N/A
F15	342	81.0	243	18.0	0.220	14.6	0.225	13.3	N/A
G15	318	81.0	219	18.0	0.190	14.6	0.175	13.3	N/A
A16	438	81.0	339	18.0	0.135	10.6	0.125	13.2	2.00

(Table B.1 continued)

Pile	Length Measurements (in.)				Measurements of Remaining Section at Severely Corroded Region (L_C) (in.)				
	Total Length (L_G)	Top Length (L_T)	Bottom Length (L_B)	Corroded Length (L_C)	Flange Thickness (t_{fc})	Flange Width (b_{fc})	Web Thickness (t_{wc})	Depth (d_c)	Web Void Width (b_{hc})
B16	426	81.0	327	18.0	0.190	14.6	0.175	13.3	N/A
C16	408	81.0	309	18.0	0.125	10.6	0.180	13.2	N/A
D16	396	81.0	297	18.0	0.165	10.6	0.225	13.3	N/A
E16	378	81.0	279	18.0	0.205	12.6	0.145	13.3	N/A
F16	342	81.0	243	18.0	0.205	14.6	0.180	13.3	N/A
G16	318	81.0	219	18.0	0.145	14.6	0.210	13.2	N/A
A17	438	81.0	339	18.0	0.120	4.60	0.125	13.2	N/A
B17	426	81.0	327	18.0	0.175	6.60	0.195	13.3	N/A
C17	408	81.0	309	18.0	0.170	14.6	0.160	13.3	N/A
D17	396	81.0	297	18.0	0.135	14.6	0.235	13.2	N/A
E17	378	81.0	279	18.0	0.135	14.6	0.275	13.2	N/A
F17	342	81.0	243	18.0	0.130	14.6	0.175	13.2	N/A
G17	318	81.0	219	18.0	0.140	14.6	0.210	13.2	N/A
A18*	380	23.0	339	18.0	0.215	14.6	0.185	13.3	N/A
B18	426	81.0	327	18.0	0.125	6.60	0.205	13.2	N/A
C18	408	81.0	309	18.0	0.165	14.6	0.135	13.3	N/A
D18	396	78.0	294	24.0	0.125	10.6	0.190	13.2	N/A
E18	378	81.0	279	18.0	0.145	10.6	0.210	13.2	N/A
F18	342	72.0	234	36.0	0.125	4.60	0.180	13.2	N/A
G18	318	78.0	216	24.0	0.135	8.60	0.160	13.2	N/A
A19*	380	23.0	339	18.0	0.215	14.6	0.205	13.3	N/A
B19	426	81.0	327	18.0	0.200	8.60	0.245	13.3	N/A
C19	408	81.0	309	18.0	0.190	8.60	0.145	13.3	N/A
D19	396	81.0	297	18.0	0.125	14.6	0.225	13.2	N/A
E19	378	78.0	276	24.0	0.135	8.60	0.230	13.2	N/A
F19	342	81.0	243	18.0	0.230	6.60	0.250	13.3	N/A
G19	318	81.0	219	18.0	0.190	10.6	0.225	13.3	N/A
A20	438	78.0	336	24.0	0.265	10.6	0.260	13.4	N/A
B20	426	81.0	327	18.0	0.180	6.6	0.235	13.3	N/A
C20	408	81.0	309	18.0	0.155	12.6	0.250	13.3	N/A
D20	396	78.0	294	24.0	0.160	10.6	0.230	13.3	N/A
E20	378	81.0	279	18.0	0.130	12.6	0.230	13.2	N/A
F20	342	78.0	240	24.0	0.135	10.6	0.180	13.2	N/A
G20	318	80.0	218	20.0	0.175	10.6	0.200	13.3	N/A

* indicates haunch

** indicates void in web

APPENDIX C : Pile Analysis Data

The geometry information used for the numerical analysis of 140 vertical piles of the USS Salem Wharf is presented in Table C.1.

Table C.1- Geometry data for modeling

Pile ID	**Pile Model Code**	**Characteristic Lengths (in.)**				**Severe Corrosion Area Modeling Information (in.)**				
		L_C	L_T	L_B	L_G	Flange Thickness (tf_C)	Flange Width (bf_C)	Web Thickness (tw_C)	Depth (d)	Web Void Width (bh_c)
A1	T2C13B6	18.0	81.0	340	439	0.150	4.60	0.230	13.3	N/A
B1	T2C18B6	18.0	81.0	340	439	0.170	12.6	0.230	13.3	N/A
C1	T2C110B5	18.0	81.0	310	409	0.205	14.6	0.250	13.3	N/A
D1	T2C18B4	18.0	81.0	300	399	0.120	12.6	0.270	13.2	N/A
E1	T2C110B3	18.0	81.0	280	379	0.200	14.6	0.260	13.3	N/A
F1	T2C110B2	18.0	81.0	245	344	0.170	14.6	0.295	13.3	N/A
G1	T2C110B1	18.0	81.0	220	319	0.165	14.6	0.285	13.3	N/A
A2*	T1C16B6	18.0	23.0	340	381	0.145	10.6	0.130	13.2	N/A
B2	T2C18B6	18.0	81.0	340	439	0.190	12.6	0.285	13.3	N/A
C2	T2C110B5	18.0	81.0	310	409	0.235	14.6	0.245	13.3	N/A
D2	T2C54B4	36.0	81.0	300	417	0.115	6.60	0.250	13.2	N/A
E2	T2C53B3	36.0	81.0	280	397	0.125	4.60	0.190	13.2	N/A
F2	T2C45B2	30.0	81.0	245	356	0.125	8.60	0.180	13.2	N/A
G2	T2C110B1	18.0	81.0	220	319	0.165	14.6	0.260	13.3	N/A
A3*	T1C15B6	18.0	23.0	340	381	0.170	8.60	0.225	13.3	N/A
B3	T2C16B6	18.0	81.0	340	439	0.120	10.6	0.165	13.2	N/A
C3	T2C45B5	30.0	81.0	310	421	0.135	8.60	0.205	13.2	N/A
D3	T2C14B4	18.0	81.0	300	399	0.125	6.60	0.170	13.2	N/A
E3	T2C35B3	24.0	81.0	280	385	0.190	8.60	0.185	13.3	N/A
F3	T2C34B2	24.0	81.0	245	350	0.190	6.60	0.270	13.3	N/A
G3	T2C110B1	18.0	81.0	220	319	0.290	14.6	0.240	13.4	N/A
A4	T2C16B6	18.0	81.0	340	439	0.170	10.6	0.245	13.3	N/A
B4**	T2C33B6	24.0	81.0	340	445	0.120	4.60	0.135	13.2	12.0
C4	T2C36B5	24.0	81.0	310	415	0.175	10.6	0.145	13.3	N/A
D4	T2C43B4	30.0	81.0	300	411	0.165	4.60	0.185	13.3	N/A
E4	T2C51B3	36.0	81.0	280	397	0.110	0.60	0.175	13.2	N/A
F4	T2C44B2	30.0	81.0	245	356	0.175	6.60	0.130	13.3	N/A
G4	T2C44B1	30.0	81.0	220	331	0.175	6.60	0.130	13.3	N/A
A5**	T2C33B6	24.0	81.0	340	445	0.100	4.60	0.100	13.2	8.00
B5**	T2C13B6	18.0	81.0	340	439	0.185	4.60	0.130	13.3	3.00

(Table C.1 continued)

Pile ID	Pile Model Code	Characteristic Lengths (in.)				Severe Corrosion Area Modeling Information (in.)				
		L_C	L_T	L_B	L_G	Flange Thickness (tf_C)	Flange Width (bf_C)	Web Thickness (tw_C)	Depth (d)	Web Void Width (bh_c)
C5	T2C33B5	24.0	81.0	310	415	0.200	4.60	0.245	13.3	N/A
D5	T2C15B4	18.0	81.0	300	399	0.165	8.60	0.125	13.3	N/A
E5	T2C16B3	18.0	81.0	280	379	0.125	10.6	0.165	13.2	N/A
F5	T2C14B2	18.0	81.0	245	344	0.200	6.60	0.180	13.3	N/A
G5	T2C16B1	18.0	81.0	220	319	0.165	10.6	0.240	13.3	N/A
A6*	T1C110B6	18.0	23.0	340	381	0.160	14.6	0.135	13.3	N/A
B6	T2C14B6	18.0	81.0	340	439	0.125	6.60	0.180	13.2	N/A
C6	T2C53B5	36.0	81.0	310	427	0.120	4.60	0.130	13.2	N/A
D6	T2C45B4	30.0	81.0	300	411	0.115	8.60	0.175	13.2	N/A
E6	T2C53B3	36.0	81.0	280	397	0.125	4.60	0.175	13.2	N/A
F6	T2C54B2	36.0	81.0	245	362	0.115	6.60	0.165	13.2	N/A
G6	T2C18B1	18.0	81.0	220	319	0.170	12.6	0.220	13.3	N/A
A7*	T1C110B6	18.0	23.0	340	381	0.165	14.6	0.240	13.3	N/A
B7	T2C110B6	18.0	81.0	340	439	0.160	14.6	0.200	13.3	N/A
C7	T2C16B5	18.0	81.0	310	409	0.135	10.6	0.205	13.2	N/A
D7	T2C16B4	18.0	81.0	300	399	0.215	10.6	0.180	13.3	N/A
E7	T2C16B3	18.0	81.0	280	379	0.125	10.6	0.205	13.2	N/A
F7	T2C14B2	18.0	81.0	245	344	0.175	6.60	0.230	13.3	N/A
G7	T2C15B1	18.0	81.0	220	319	0.125	8.60	0.225	13.2	N/A
A8	T2C110B6	18.0	81.0	340	439	0.135	14.6	0.115	13.2	N/A
B8**	T2C15B6	18.0	81.0	340	439	0.180	8.60	0.185	13.3	5.00
C8**	T2C14B5	18.0	81.0	310	409	0.245	6.60	0.120	13.3	1.00
D8	T2C110B4	18.0	81.0	300	399	0.240	14.6	0.175	13.3	N/A
E8	T2C16B3	18.0	81.0	280	379	0.135	10.6	0.230	13.2	N/A
F8	T2C15B2	18.0	81.0	245	344	0.195	8.60	0.230	13.3	N/A
G8	T2C16B1	18.0	81.0	220	319	0.135	10.6	0.210	13.2	N/A
A9	T2C110B6	18.0	81.0	340	439	0.190	14.6	0.210	13.3	N/A
B9	T2C15B6	18.0	81.0	340	439	0.120	8.60	0.160	13.2	N/A
C9	T2C16B5	18.0	81.0	310	409	0.120	10.6	0.270	13.2	N/A
D9	T2C19B4	18.0	81.0	300	399	0.115	13.6	0.190	13.2	N/A
E9	T2C18B3	18.0	81.0	280	379	0.120	12.6	0.320	13.2	N/A
F9	T2C57B2	36.0	81.0	245	362	0.400	11.6	0.280	13.5	N/A
G9	T2C36B1	24.0	81.0	220	325	0.120	10.6	0.180	13.2	N/A
A10*	T1C16B6	18.0	23.0	340	381	0.215	10.6	0.195	13.3	N/A
B10	T2C14B6	18.0	81.0	340	439	0.170	6.60	0.185	13.3	N/A
C10	T2C18B5	18.0	81.0	310	409	0.130	12.6	0.120	13.2	N/A
D10	T2C110B4	18.0	81.0	300	399	0.140	14.6	0.125	13.2	N/A
E10	T2C62B3	42.0	81.0	280	403	0.100	2.60	0.140	13.2	N/A

(Table C.1 continued)

Pile ID	Pile Model Code	Characteristic Lengths (in.)				Severe Corrosion Area Modeling Information (in.)				
		L_C	L_T	L_B	L_G	Flange Thickness (tf_C)	Flange Width (bf_C)	Web Thickness (tw_C)	Depth (d)	Web Void Width (bh_c)
F10	T2C15B2	18.0	81.0	245	344	0.170	8.60	0.180	13.3	N/A
G10	T2C16B1	18.0	81.0	220	319	0.185	10.6	0.150	13.3	N/A
A11*	T1C110B6	18.0	23.0	340	381	0.170	14.6	0.120	13.3	N/A
B11	T2C110B6	18.0	81.0	340	439	0.170	14.6	0.155	13.3	N/A
C11	T2C35B5	24.0	81.0	310	415	0.110	8.60	0.265	13.2	N/A
D11	T2C73B3	60.0	81.0	280	421	0.120	4.60	0.135	13.2	N/A
E11	T2C54B3	36.0	81.0	280	397	0.115	6.60	0.130	13.2	N/A
F11	T2C54B2	36.0	81.0	245	362	0.130	6.60	0.165	13.2	N/A
G11	T2C35B1	24.0	81.0	220	325	0.185	8.60	0.215	13.3	N/A
A12**	T2C13B6	18.0	81.0	340	439	0.175	4.60	0.215	13.3	8.00
B12**	T2C14B6	18.0	81.0	340	439	0.190	6.60	0.170	13.3	4.00
C12	T2C18B5	18.0	81.0	310	409	0.125	12.6	0.125	13.2	N/A
D12	T2C15B4	18.0	81.0	300	399	0.210	8.60	0.165	13.3	N/A
E12	T2C15B3	18.0	81.0	280	379	0.180	8.60	0.135	13.3	N/A
F12	T2C14B2	18.0	81.0	245	344	0.125	6.60	0.190	13.2	N/A
G12	T2C16B1	18.0	81.0	220	319	0.120	10.6	0.185	13.2	N/A
A13	T2C16B6	18.0	81.0	340	439	0.125	10.6	0.165	13.2	N/A
B13**	T2C13B6	18.0	81.0	340	439	0.100	4.60	0.100	13.2	6.00
C13	T2C18B5	18.0	81.0	310	409	0.135	12.6	0.195	13.2	N/A
D13	T2C110B4	18.0	81.0	300	399	0.175	14.6	0.140	13.3	N/A
E13	T2C18B3	18.0	81.0	280	379	0.120	12.6	0.175	13.2	N/A
F13	T2C16B2	18.0	81.0	245	344	0.135	10.6	0.210	13.2	N/A
G13	T2C110B1	18.0	81.0	220	319	0.185	14.6	0.285	13.3	N/A
A14*	T1C110B6	18.0	23.0	340	381	0.295	14.6	0.205	13.4	N/A
B14	T2C110B6	18.0	81.0	340	439	0.350	14.6	0.270	13.5	N/A
C14	T2C18B5	18.0	81.0	310	409	0.185	12.6	0.120	13.3	N/A
D14	T2C110B4	18.0	81.0	300	399	0.140	14.6	0.130	13.2	N/A
E14	T2C18B3	18.0	81.0	280	379	0.125	12.6	0.135	13.2	N/A
F14	T2C110B2	18.0	81.0	245	344	0.170	14.6	0.170	13.3	N/A
G14	T2C110B1	18.0	81.0	220	319	0.155	14.6	0.160	13.3	N/A
A15*	T1C110B6	18.0	23.0	340	381	0.190	14.6	0.155	13.3	N/A
B15	T2C110B6	18.0	81.0	340	439	0.195	14.6	0.165	13.3	N/A
C15	T2C110B5	18.0	81.0	310	409	0.125	14.6	0.145	13.2	N/A
D15	T2C110B4	18.0	81.0	300	399	0.115	14.6	0.150	13.2	N/A
E15	T2C110B3	18.0	81.0	280	379	0.170	14.6	0.205	13.3	N/A
F15	T2C110B2	18.0	81.0	245	344	0.220	14.6	0.225	13.3	N/A
G15	T2C110B1	18.0	81.0	220	319	0.190	14.6	0.175	13.3	N/A
A16**	T2C16B6	18.0	81.0	340	439	0.135	10.6	0.125	13.2	2.00

(Table C.1 continued)

Pile ID	Pile Model Code	Characteristic Lengths (in.)				Severe Corrosion Area Modeling Information (in.)				
		L_C	L_T	L_B	L_G	Flange Thickness (tf_C)	Flange Width (bf_C)	Web Thickness (tw_C)	Depth (d)	Web Void Width (bh_c)
B16	T2C110B6	18.0	81.0	340	439	0.190	14.6	0.175	13.3	N/A
C16	T2C16B5	18.0	81.0	310	409	0.125	10.6	0.180	13.2	N/A
D16	T2C16B4	18.0	81.0	300	399	0.165	10.6	0.225	13.3	N/A
E16	T2C18B3	18.0	81.0	280	379	0.205	12.6	0.145	13.3	N/A
F16	T2C110B2	18.0	81.0	245	344	0.205	14.6	0.180	13.3	N/A
G16	T2C110B1	18.0	81.0	220	319	0.145	14.6	0.210	13.2	N/A
A17	T2C13B6	18.0	81.0	340	439	0.120	4.60	0.125	13.2	N/A
B17	T2C14B6	18.0	81.0	340	439	0.175	6.60	0.195	13.3	N/A
C17	T2C110B5	18.0	81.0	310	409	0.170	14.6	0.160	13.3	N/A
D17	T2C110B4	18.0	81.0	300	399	0.135	14.6	0.235	13.2	N/A
E17	T2C110B3	18.0	81.0	280	379	0.135	14.6	0.275	13.2	N/A
F17	T2C110B2	18.0	81.0	245	344	0.130	14.6	0.175	13.2	N/A
G17	T2C110B1	18.0	81.0	220	319	0.140	14.6	0.210	13.2	N/A
A18*	T1C110B6	18.0	23.0	340	381	0.215	14.6	0.185	13.3	N/A
B18	T2C14B6	18.0	81.0	340	439	0.125	6.60	0.205	13.2	N/A
C18	T2C110B5	18.0	81.0	310	409	0.165	14.6	0.135	13.3	N/A
D18	T2C36B4	24.0	81.0	300	405	0.125	10.6	0.190	13.2	N/A
E18	T2C16B3	18.0	81.0	280	379	0.145	10.6	0.210	13.2	N/A
F18	T2C53B2	36.0	81.0	245	362	0.125	4.60	0.180	13.2	N/A
G18	T2C35B1	24.0	81.0	220	325	0.135	8.60	0.160	13.2	N/A
A19*	T1C110B6	18.0	23.0	340	381	0.215	14.6	0.205	13.3	N/A
B19	T2C15B6	18.0	81.0	340	439	0.200	8.60	0.245	13.3	N/A
C19	T2C15B5	18.0	81.0	310	409	0.190	8.60	0.145	13.3	N/A
D19	T2C110B4	18.0	81.0	300	399	0.125	14.6	0.225	13.2	N/A
E19	T2C35B3	24.0	81.0	280	385	0.135	8.60	0.230	13.2	N/A
F19	T2C14B2	18.0	81.0	245	344	0.230	6.60	0.250	13.3	N/A
G19	T2C16B1	18.0	81.0	220	319	0.190	10.6	0.225	13.3	N/A
A20	T2C36B6	24.0	81.0	340	445	0.265	10.6	0.260	13.4	N/A
B20	T2C14B6	18.0	81.0	340	439	0.180	6.60	0.235	13.3	N/A
C20	T2C18B5	18.0	81.0	310	409	0.155	12.6	0.250	13.3	N/A
D20	T2C36B4	24.0	81.0	300	405	0.160	10.6	0.230	13.3	N/A
E20	T2C18B3	18.0	81.0	280	379	0.130	12.6	0.230	13.2	N/A
F20	T2C36B2	24.0	81.0	245	350	0.135	10.6	0.180	13.2	N/A
G20	T2C26B1	20.0	81.0	220	321	0.175	10.6	0.200	13.3	N/A

* indicates haunch

** indicates void in web

APPENDIX D : Pile Load-Shortening Curves

The axial load-shortening curves for the piles determined through finite element analysis are presented in Figure D.1 to Figure D.5.

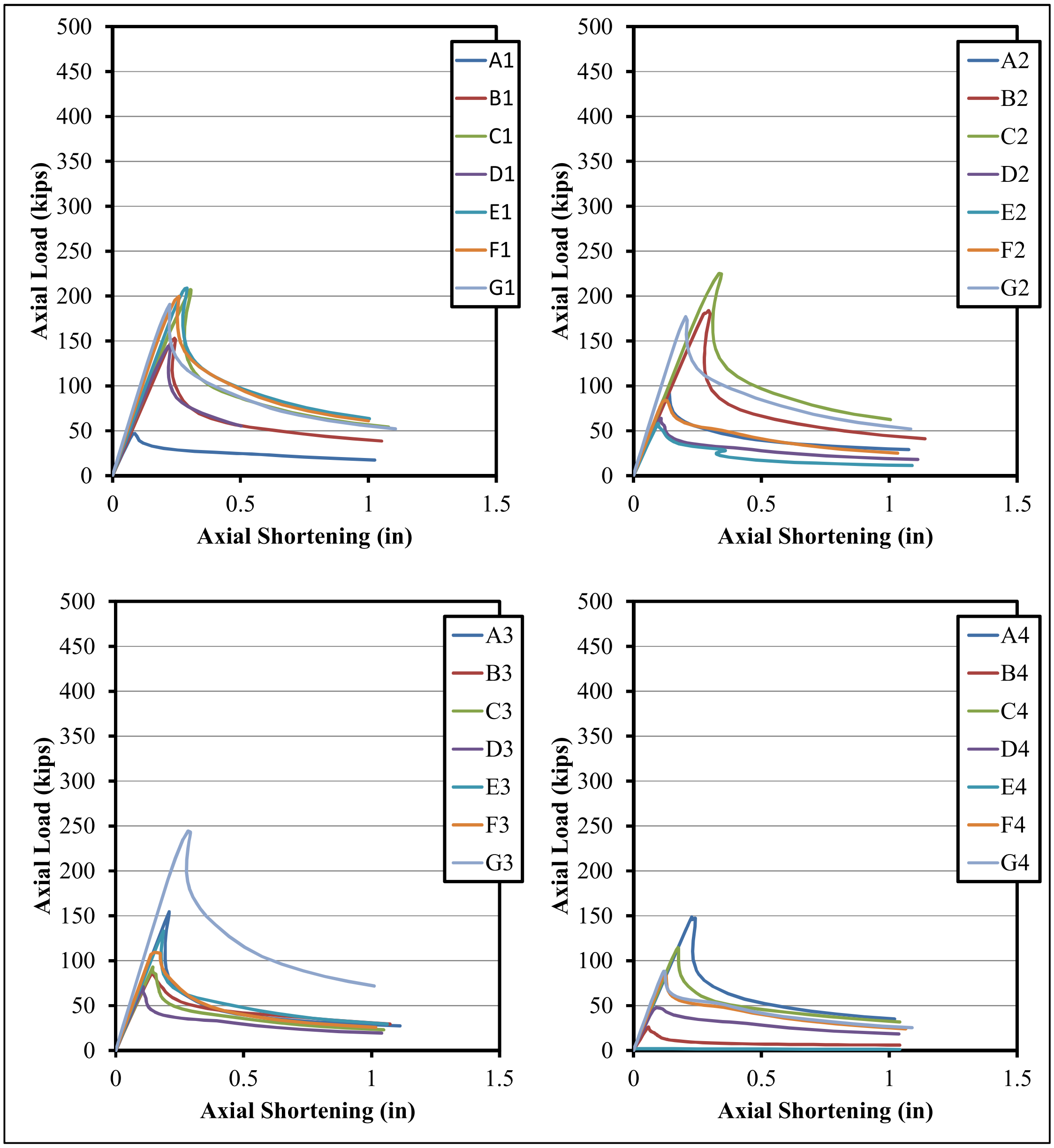

Figure D.1- Axial load-shortening curve for pile-rows 1 to 4

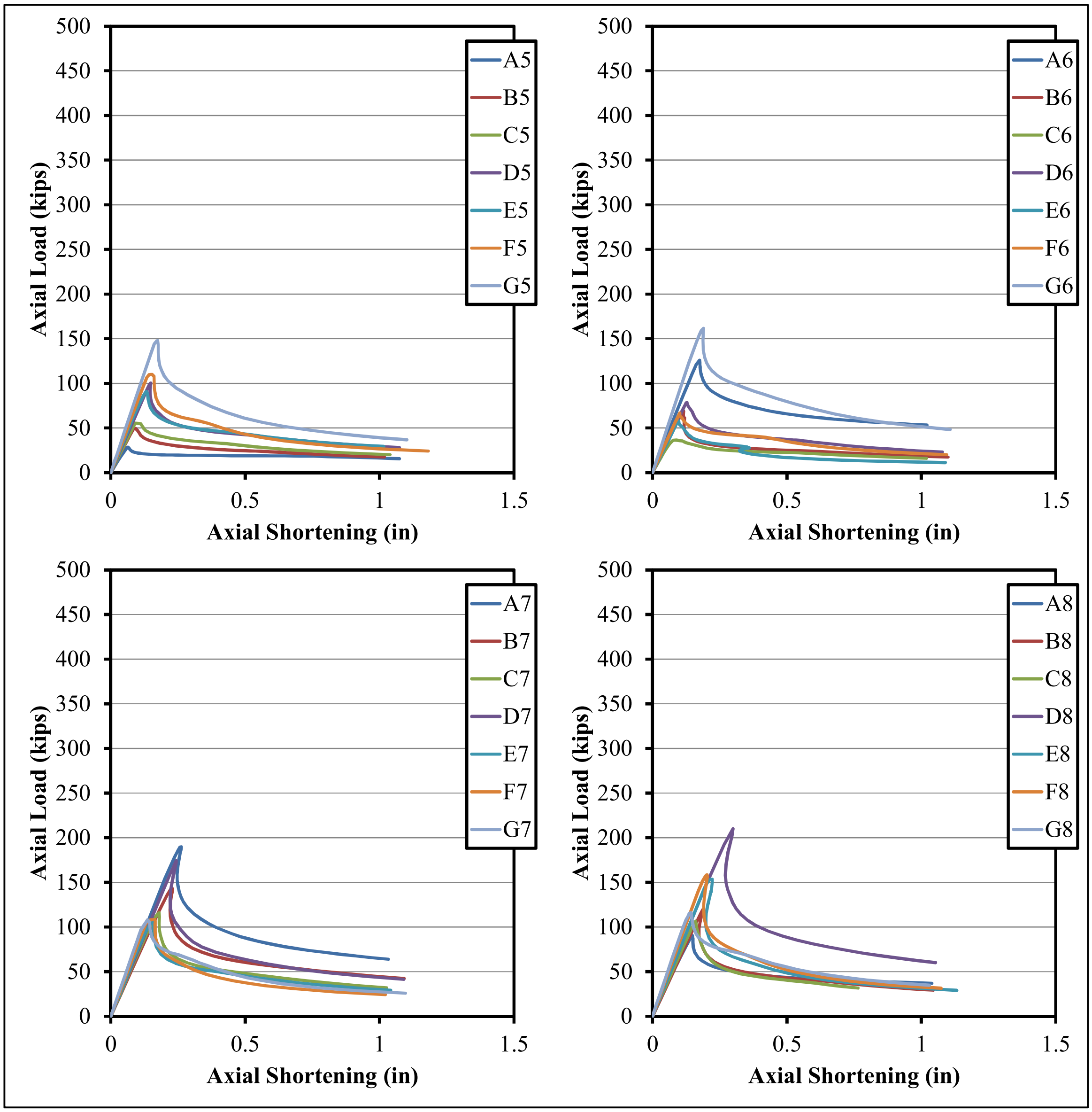

Figure D.2- Axial load-shortening curve for pile-rows 5 to 8

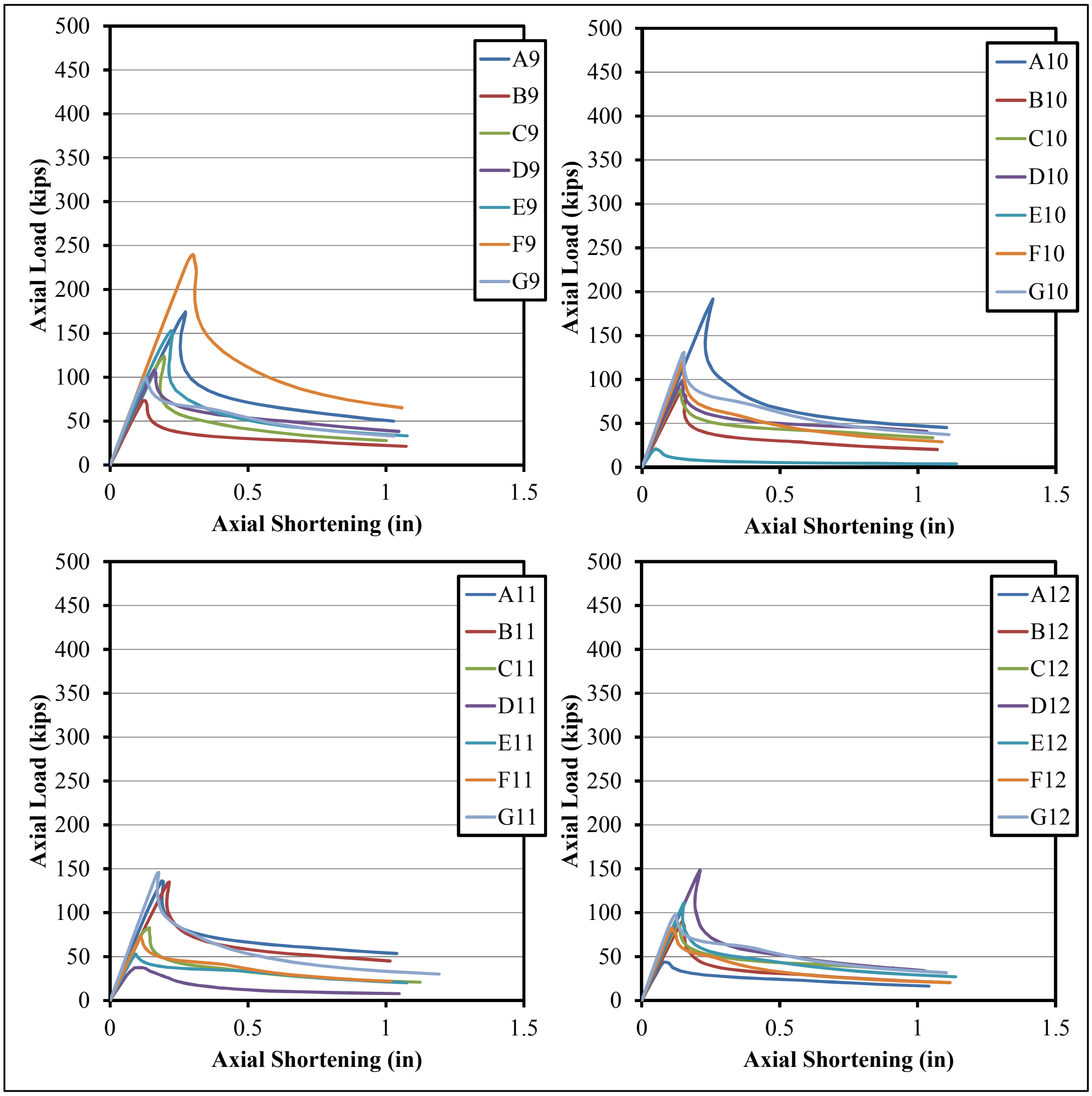

Figure D.3- Axial load-shortening curve for pile-rows 9 to 12

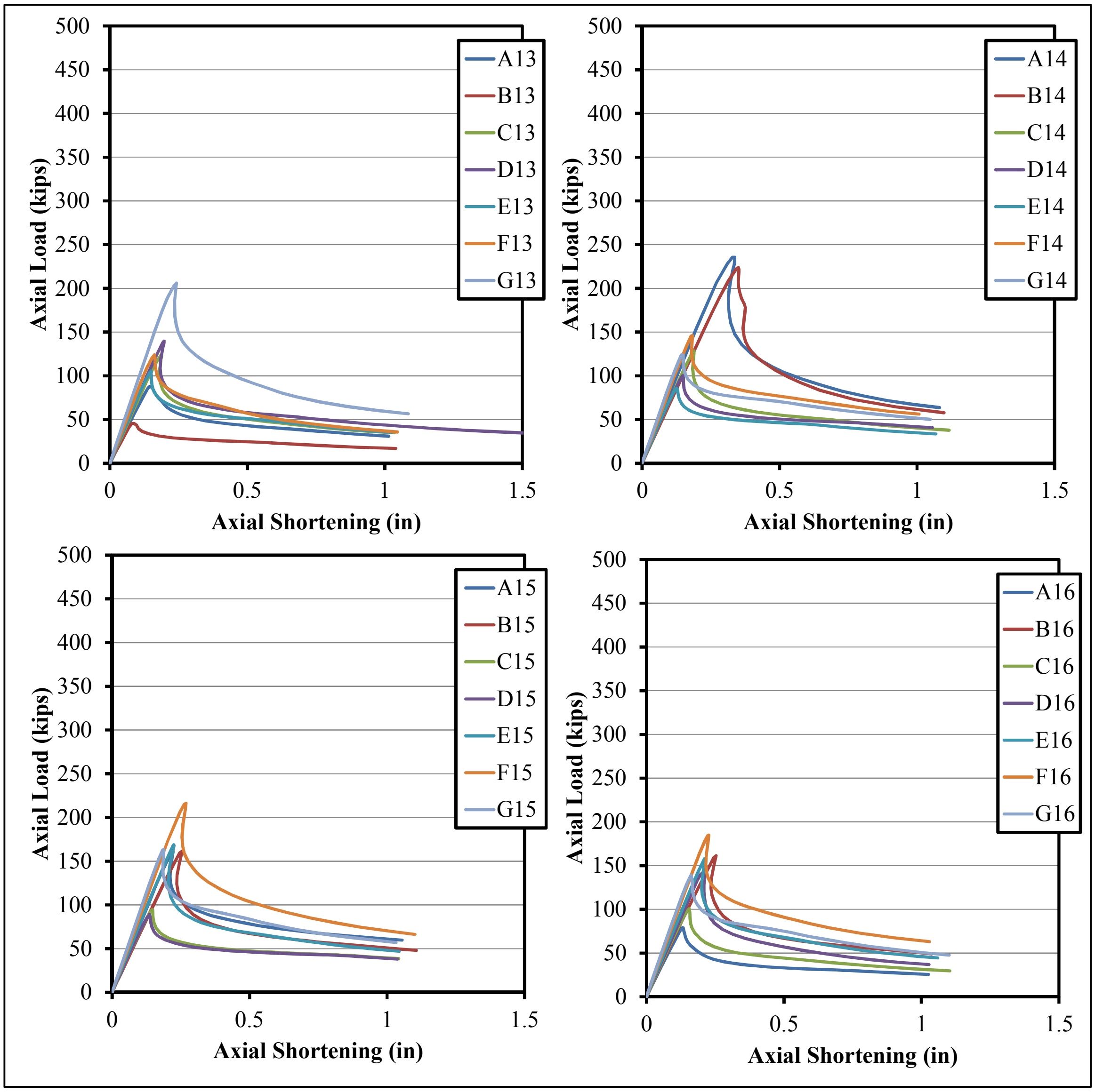

Figure D.4- Axial load-shortening curve for pile-rows 13 to 16

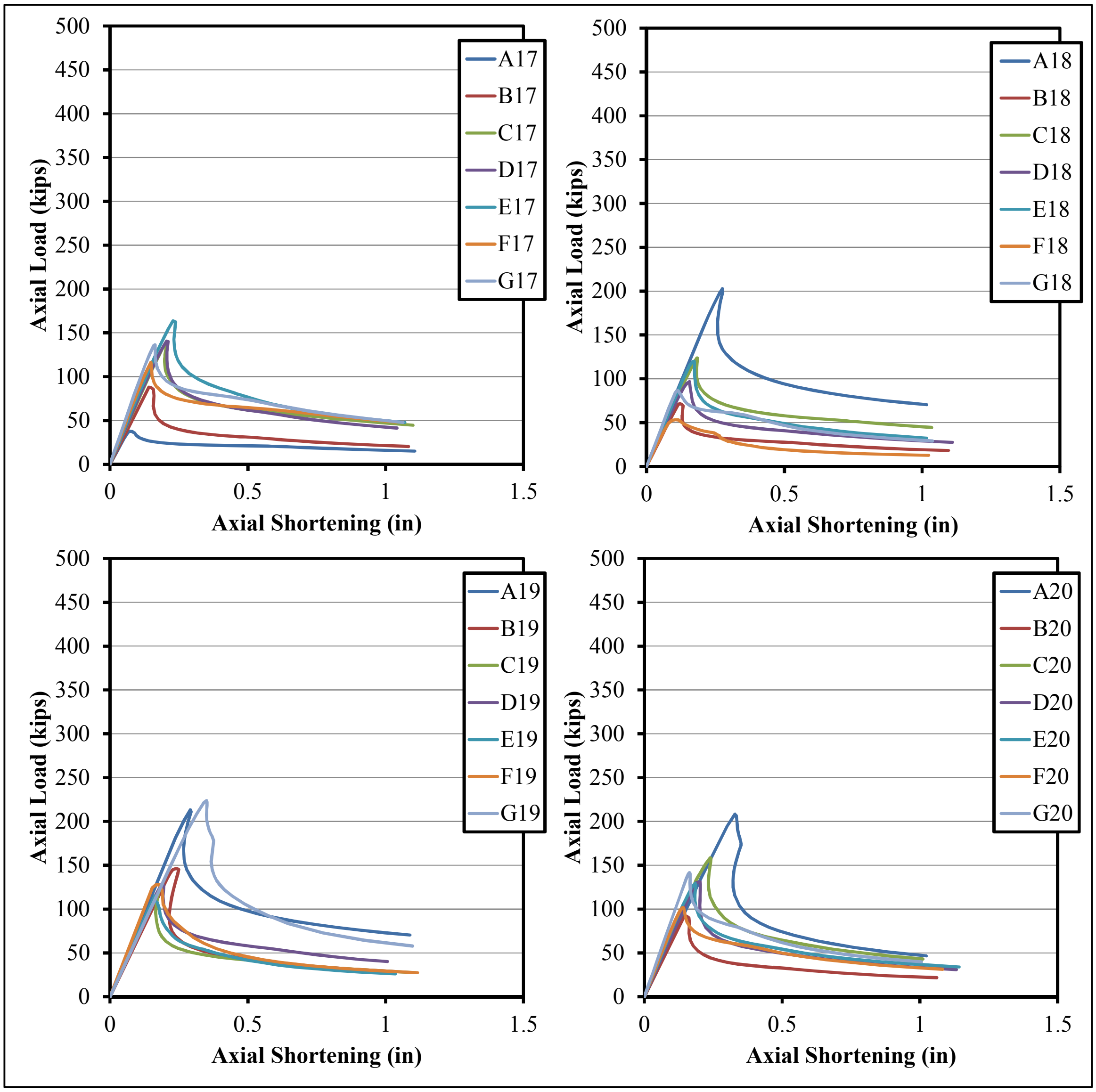

Figure D.5- Axial load-shortening curve for pile-rows 17 to 20

APPENDIX E : Idealized Load-Shortening Curves

The idealized axial load-shortening curves used in the collapse analysis of the USS Salem Wharf are presented in Figure E.1 to Figure E.5.

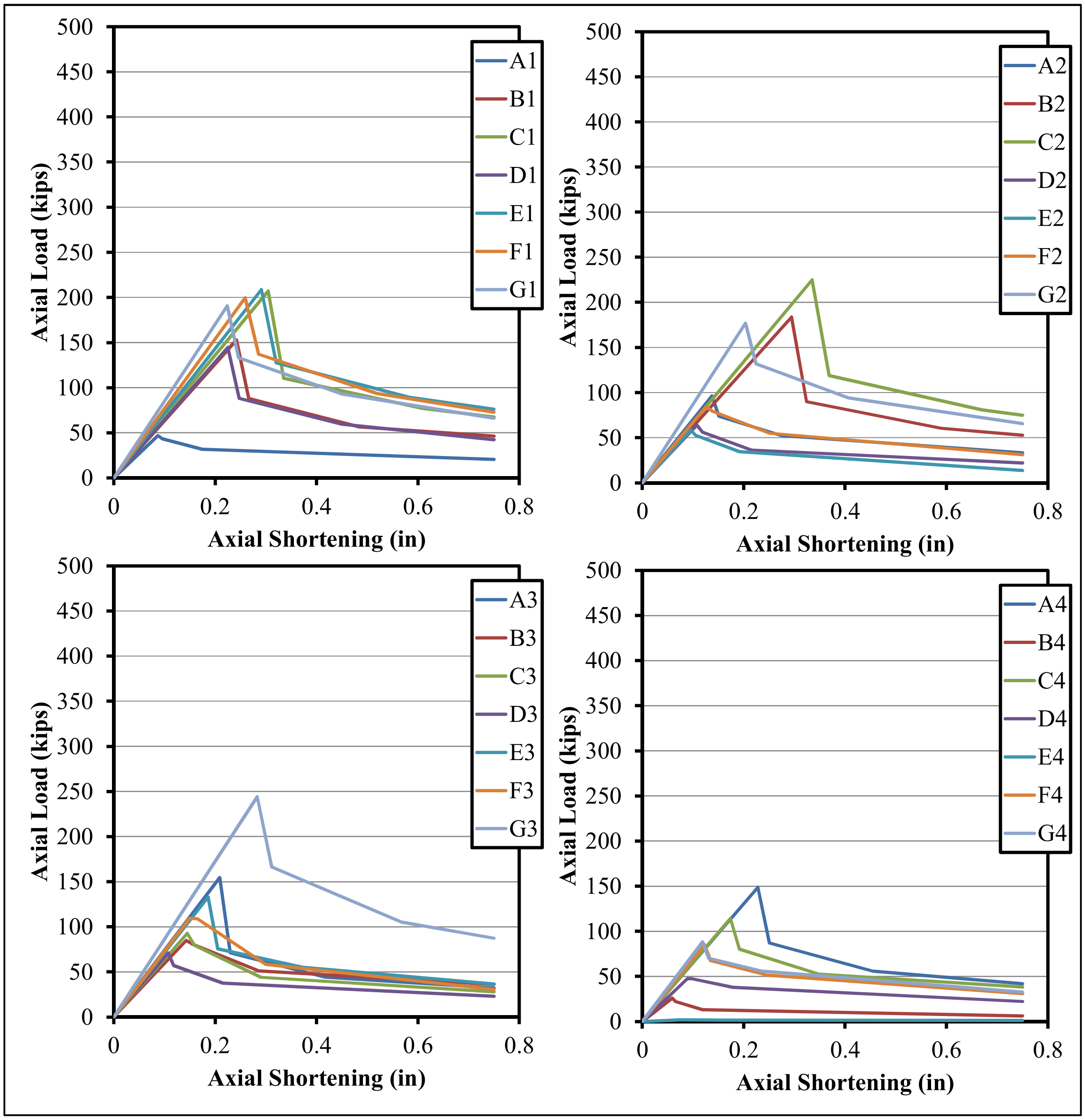

Figure E.1- Idealized axial load-shortening curve for pile-rows 1 to 4

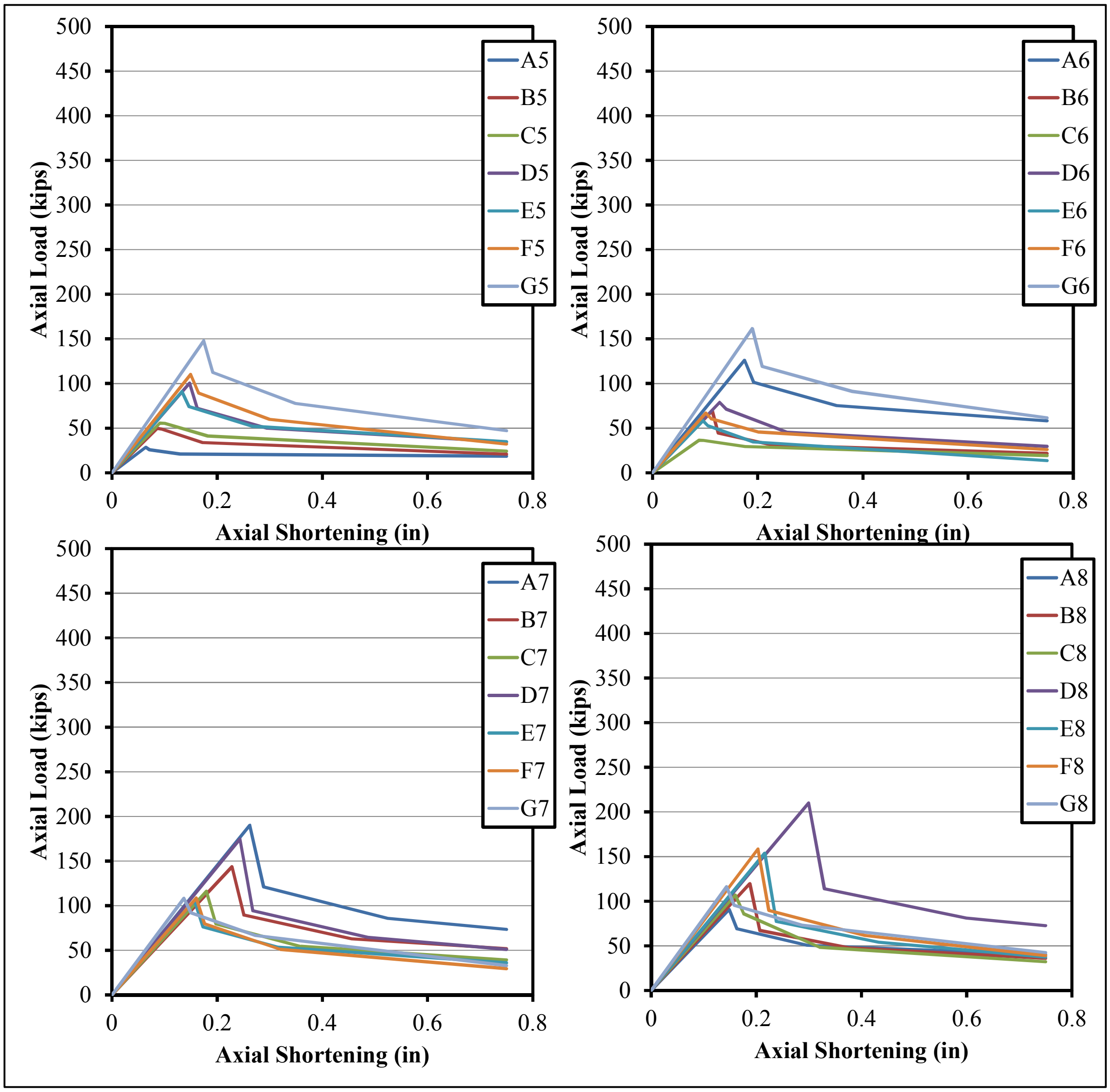

Figure E.2- Idealized axial load-shortening curve for pile-rows 5 to 8

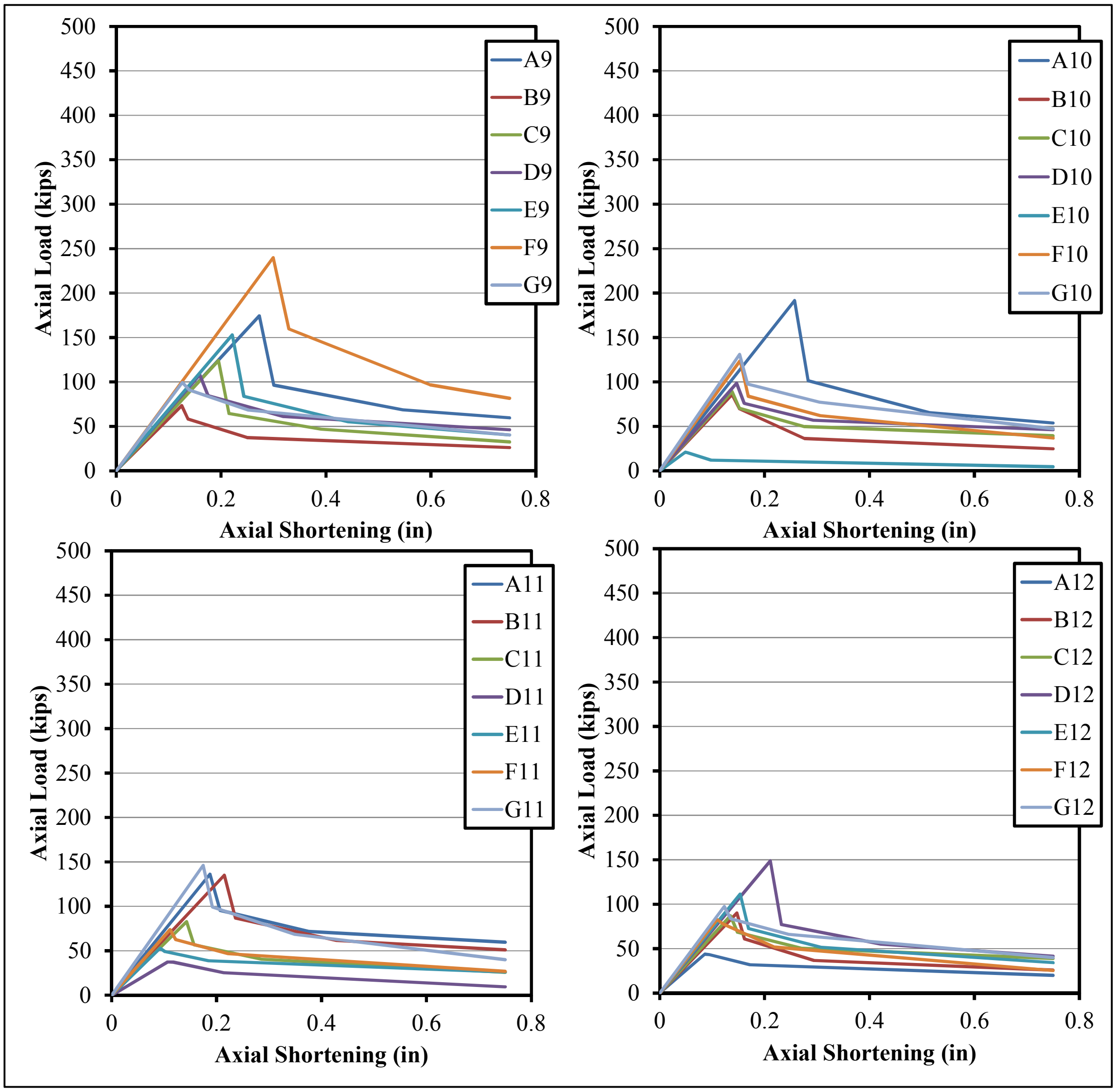

Figure E.3- Idealized axial load-shortening curve for pile-rows 9 to 12

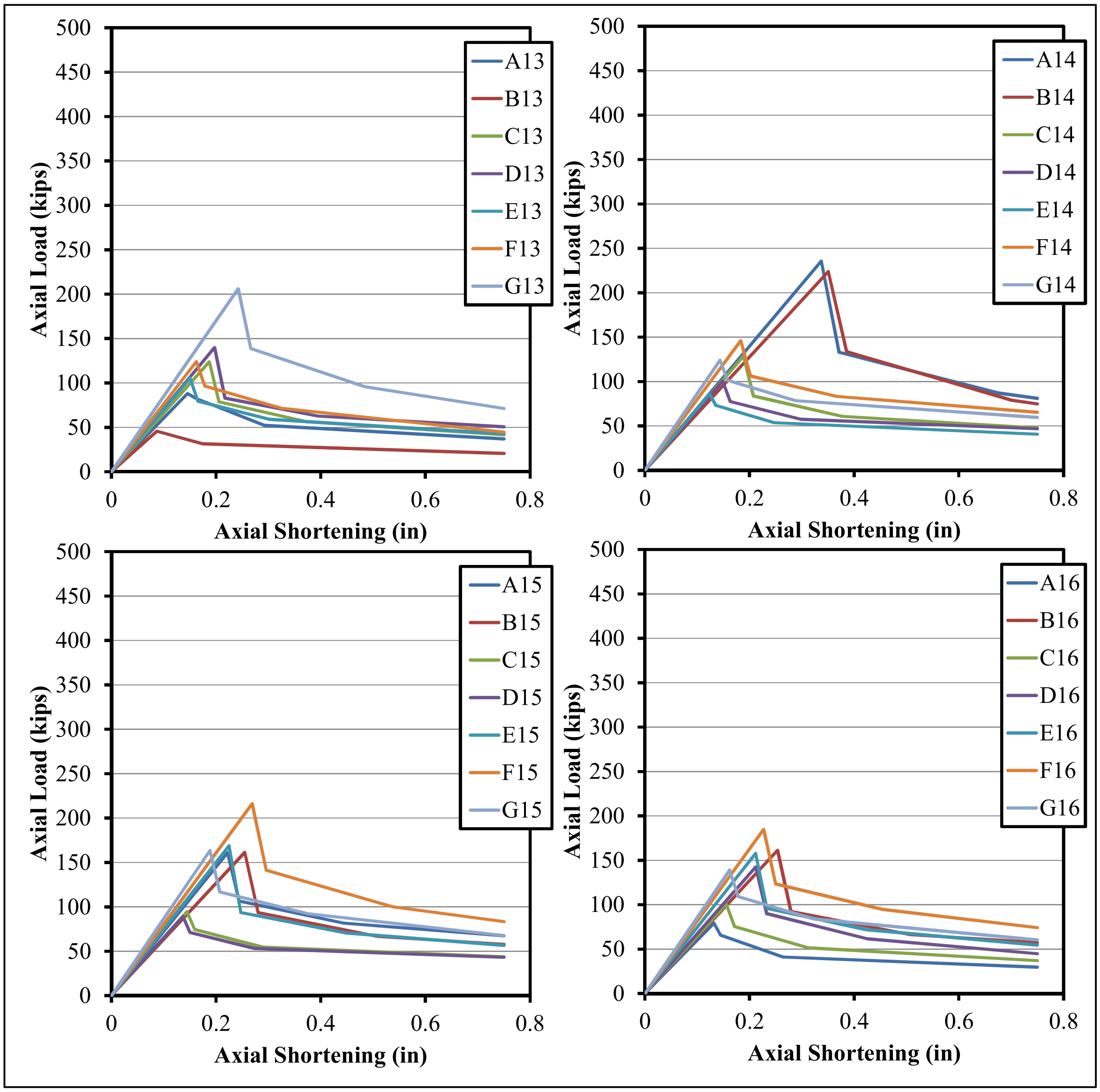

Figure E.4- Idealized axial load-shortening curve for pile-rows 13 to 16

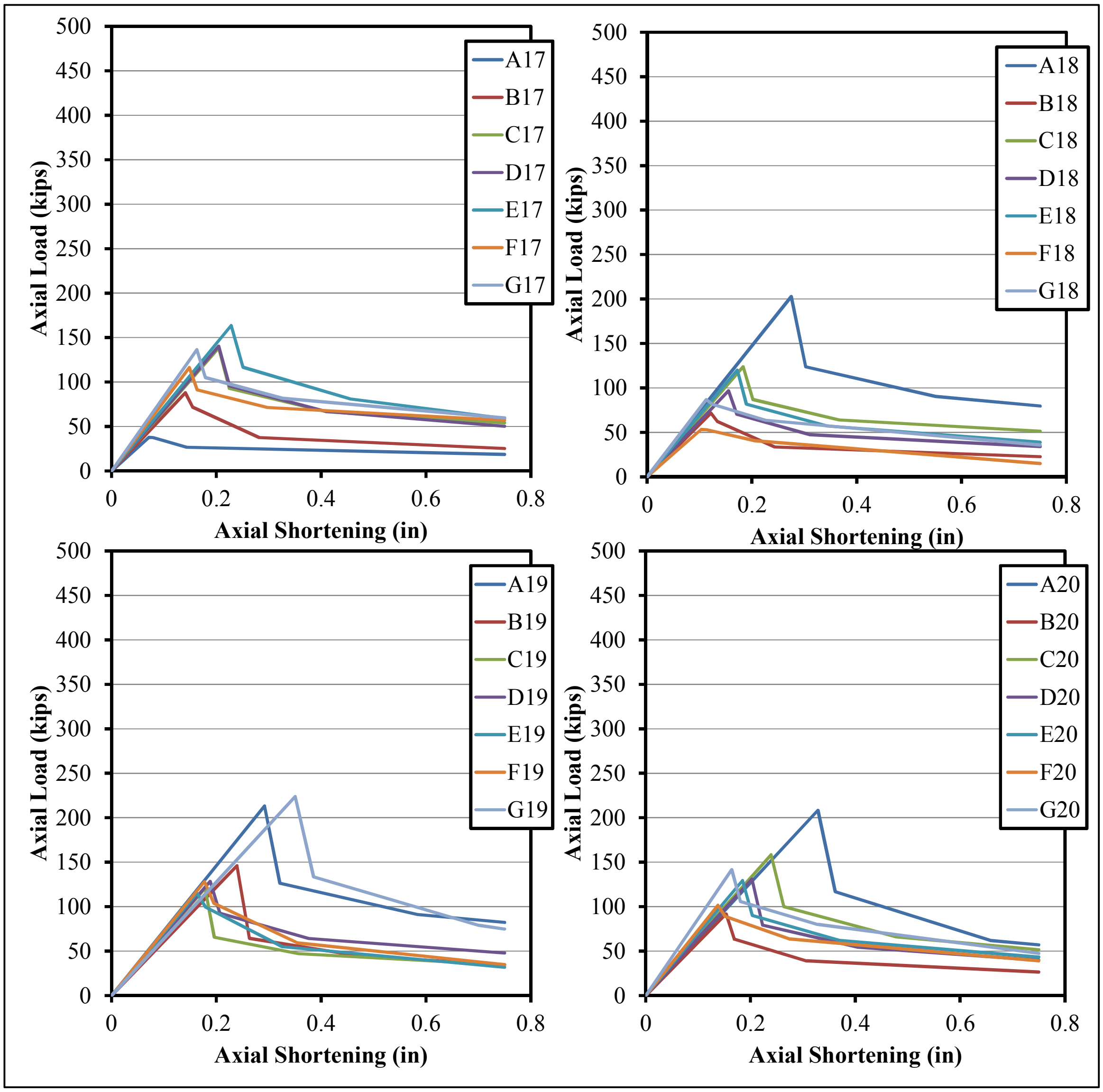

Figure E.5- Idealized axial load-shortening curve for pile-rows 17 to 20

APPENDIX F : Code-Based Computation of Peak Capacity of Piles

In this investigation, the numerical framework developed by Shi, et al. (2015) was implemented to determine the load-shortening behavior of the USS Salem Wharf's vertical piles. To validate the need to implement this numerical framework, the axial capacity of these piles was also computed using the design methods recommended by the American Institute of Steel Construction (AISC) (2010), the American Association of State Highway and Transportation Officials (AASHTO) (2012), and the American Iron and Steel Institute (AISI) (2012). The method adopted by (AISC, 2010) and (AASHTO, 2012) is referred to herein as the AISC Method, while (AISI, 2012) provides two methods to predict axial capacity, the AISI Effective Width Method (AISI-EWM) and the AISI Direct Strength Method (AISI-DSM). A brief review of these three procedures is presented in this appendix. Additionally, the predictions of axial capacity corresponding to code provisions are summarized for a set of sample piles.

- **AISC and AASHTO**

In the AISC method, the SSRC-2P curve was adopted for the calculation of global strength (Zieman, 2010). This curve is one of many developed by Bjorhovde (1988) for this purpose, and is based on a modified Euler buckling equation which considers the effect of initial out-of-straightness, while the inelastic global buckling capacity is calculated through an empirical equation. These curves were adopted by the Structural Stability Research Council for the computation of the global strength of columns, and are presented in Figure F.1.

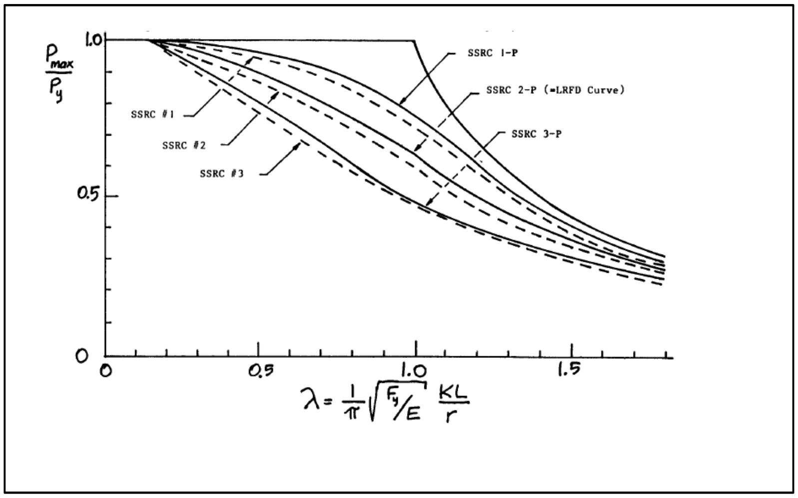

Figure F.1- Comparison of multiple column curves (Bjorhovde, 1988)

In this approach, the presence of slender elements can be accounted for with the introduction of strength reduction factors. The nominal axial strength is calculated as

$$P_n = F_{cr} A_g\,, \tag{F-1}$$

where F_{cr} is the critical stress and A_g is the gross cross-sectional area of the compression member.

To account for the presence of slender elements, reduction factors Q_s and Q_a are introduced for un-stiffened and stiffened slender elements, respectively. The calculation of the critical stress when slender elements are present is given by

$$F_{cr} = Q\left(0.658^{\frac{QF_y}{F_e}}\right)F_y \;\; for \;\; \frac{KL}{r} \leq 4.71\sqrt{\frac{E}{QF_y}} \text{ and} \tag{F-2}$$

$$= 0.877F_e \;\; for \;\; \frac{KL}{r} > 4.71\sqrt{\frac{E}{QF_y}}\,, \tag{F-3}$$

where F_e is the elastic buckling stress while F_y and E are the yield stress and elastic modulus of the material, respectively. Here, K, L, and r represent the effective length factor, length of the member, and radius of gyration of the cross, respectively.

The reduction factors to account for slender elements are determined as

$$Q = Q_a Q_s, \tag{F-4}$$

$$Q_s = 1.0 \quad for \quad \frac{b_f}{2t_f} \le 0.56\sqrt{\frac{E}{F_y}}, \tag{F-5}$$

$$= 1.415 - 0.74\left(\frac{b_f}{2t_f}\right)\sqrt{\frac{F_y}{E}} \quad for \quad 0.56\sqrt{\frac{E}{F_y}} < \frac{b_f}{2t_f} < 1.03\sqrt{\frac{E}{F_y}}, \tag{F-6}$$

$$= \frac{0.69E}{F_y\left(\frac{b_f}{2t_f}\right)^2} \quad for \quad \frac{b_f}{2t_f} \ge 1.03\sqrt{\frac{E}{F_y}}, \tag{F-7}$$

$$Q_s = 1.0 \quad for \quad \frac{d}{t} \le 0.75\sqrt{\frac{E}{F_y}}, \tag{F-8}$$

$$= 1.908 - 1.22\left(\frac{d}{t}\right)\sqrt{\frac{F_y}{E}} \quad for \quad 0.75\sqrt{\frac{E}{F_y}} < \frac{d}{t} < 1.03\sqrt{\frac{E}{F_y}}, \text{ and} \tag{F-9}$$

$$= \frac{0.69E}{F_y\left(\frac{d}{t}\right)^2} \quad for \quad \frac{d}{t} \ge 1.03\sqrt{\frac{E}{F_y}} \tag{F-10}$$

here, Q_s is the reduction factor corresponding to un-stiffened slender elements as given in Equations (F-5), (F-6) and (F-7) for flange elements and Equations (F-8), (F-9) and (F-10) for stems of tees.

The reduction factor for stiffened slender elements, Q_a, is given as

$$Q_a = \frac{h_e}{h}, \tag{F-11}$$

where,

$$h_e = 1.92 t_w \sqrt{\frac{E}{f}} \left[1 - \frac{0.34}{\left(\frac{h}{t_w} \right)} \sqrt{\frac{E}{f}} \right] \le h \ . \tag{F-12}$$

Here, f=F_{cr} which is calculated based on a compression member without slender elements ($Q = 1.0$). The actual width, effective width, and thickness of the stiffened element are represented by h, h_e, and t_w respectively.

- **AISI Effective Width Method (AISI-EWM)**

To account for slender elements, (AISI, 2012) adopted the effective width method. Here, the buckled portion of a slender element is assumed to be ineffective and instead of applying reduction factors to the critical stress as in the AISC method, an effective area is considered based on the minimum local buckling strength of the cross-section by examining each of its elements individually. As such, the nominal axial capacity is given by

$$P_n = F_n A_e, \tag{F-13}$$

where F_n is a nominal critical stress, dependent on the relationship between the yield stress and elastic buckling stress of the member, as given by

$$F_n = \left(0.658^{\lambda_c^2} \right) F_y \ \ for \ \ \lambda_c \le 1.5 \,, \tag{F-14}$$

$$= \frac{0.877}{\lambda_c^{\ 2}} F_y \ \ for \ \ \lambda_c > 1.5 \text{, and} \tag{F-15}$$

$$\lambda_c = \sqrt{\frac{F_y}{F_e}} \,, \tag{F-16}$$

where F_y is the yield stress and F_e is the Euler elastic buckling stress and the effective cross-sectional area, A_e, is calculated as

$$A_e = b_e \times t, \tag{F-17}$$

where b_e is the effective width of the element and t is its thickness. Depending upon the relationship between the calculated nominal critical stress and the critical local buckling stress, the effective width may be taken as the actual width of the slender member, b, or obtained using a reduction factor, ρ. These are given by

$$b_e = b \quad for \quad \lambda \le 0.673 \text{ and} \tag{F-18}$$

$$= \rho b \quad for \quad \lambda > 0.673 \ , \tag{F-19}$$

where

$$\lambda = \sqrt{\frac{F_n}{F_{crl}}} \tag{F-20}$$

and

$$\rho = \left(1 - \frac{0.22}{\lambda}\right) / \lambda, \tag{F-21}$$

where F_{crl} is calculated using

$$F_{crl} = k \frac{\pi^2 E}{12\left(1 - \nu^2\right)} \left(\frac{b}{t}\right)^2 \ , \tag{F-22}$$

where F_{crl} is the critical local buckling stress, ν is the Poisson's ratio of steel (0.3) and k is the plate buckling coefficient (tabulated below). The width and thickness of the plate are given by b and t respectively. The value of the plate buckling coefficient depends on the boundary condition and aspect ratio of the plate.

- **AISI Direct Strength Method (AISI-DSM)**

In contrast with the effective width method, the direct strength method accounts for the presence of slender elements by determining the governing failure mode as calculated on the basis of the properties of the entire cross-section rather than through an element-by-element assessment. In this approach, the nominal strengths associated with the global, local and distortional buckling failure modes are calculated and the critical value is selected as the nominal axial strength of the member. This is given by

$$P_n = \min\{P_{ne}, P_{nl}, P_{nd}\}, \tag{F-23}$$

where P_{ne}, P_{nl}, and P_{nd} are the nominal global, local, and distortional buckling strengths respectively. The nominal global buckling capacity is computed using

$$P_{ne} = \left(0.658^{\lambda_c^2}\right)P_y \quad for \quad \lambda_c \leq 1.5 \text{ and} \tag{F-24}$$

$$= \frac{0.877}{\lambda_c^2} P_y \quad for \quad \lambda_c > 1.5, \tag{F-25}$$

where

$$\lambda_c = \sqrt{\frac{P_y}{P_{cre}}}, \tag{F-26}$$

$$P_y = F_y A_g \text{, and} \tag{F-27}$$

$$P_{cre} = F_e A_g. \tag{F-28}$$

The nominal local buckling capacity is computed using

$$P_{nl} = P_{ne} \quad for \quad \lambda_l \leq 0.776, \tag{F-29}$$

$$= \left[1 - 0.15\left(\frac{P_{crl}}{P_{ne}}\right)^{0.4}\right]\left(\frac{P_{crl}}{P_{ne}}\right)^{0.4} P_{ne} \;\; for \;\; \lambda_l > 0.776, \qquad \text{(F-30)}$$

$$\lambda_l = \sqrt{\frac{P_{ne}}{P_{crl}}}\text{, and} \qquad \text{(F-31)}$$

$$P_{crl} = F_{crl} A_g\text{,} \qquad \text{(F-32)}$$

where F_{crl} is the minimum local buckling stress of the cross-sectional elements as calculated using Equation (F-22).

Finally, the distortional buckling strength of the member is calculated using

$$P_{nd} = P_y \;\; for \;\; \lambda_d \leq 0.561 \text{ and} \qquad \text{(F-33)}$$

$$= \left[1 - 0.25\left(\frac{P_{crd}}{P_y}\right)^{0.6}\right]\left(\frac{P_{crd}}{P_y}\right)^{0.6} P_y \;\; for \;\; \lambda_d > 0.561, \qquad \text{(F-34)}$$

where P_{crd} is the elastic distortional buckling strength of the column.

In this study, the distortional buckling failure mode is not included because the finite element analysis of the piles did not show it to be a dominant failure mode. Additionally, AISI (2012) recommends a fiber element analysis to predict the distortional buckling capacity. This analysis is applicable for prismatic members, but not for non-prismatic members.

- **Code-Based Predictions of Peak Capacity**

Sample calculations of the peak capacity according to the procedures described in the previous sections are summarized for pile-row 1 in this appendix. The pile dimensions used to perform these calculations are presented in Appendix B. The material properties of the piles are presented in Chapter 3. For these calculations, the effective length factor for calculation of the global buckling strength of piles with a web void was taken as 1.20, as recommended by Karagah

(2015). In the AISC method, Q_a was taken as 1.00 for these elements, while Q_s was calculated using Equation (F-8) to Equation (F-10). The peak capacity predictions based on these methods are presented in Table F.1 to Table F.3.

Table F.1- AISC method calculations summary

Pile	KL/r_{min}	F_e (ksi)	Q_s	Q_a	$Q=Q_sQ_a$	F_{cr} (ksi)	$P_{n,c}$ (ksi)
A1	468.7	1	1.00	1.00	1.00	1	5
B1	125.7	18	0.442	1.00	0.442	10	76
C1	96.3	31	0.478	1.00	0.478	13	117
D1	128.9	17	0.220	1.00	0.220	6	40
E1	90.2	35	0.455	1.00	0.455	13	115
F1	86.8	38	0.329	1.00	0.329	10	85
G1	80.4	44	0.310	1.00	0.310	9	79

Table F.2- AISI-EWM calculations summary

Pile	Web Effective Width					Flange Effective Width						
	k	F_{cr} (ksi)	λ	ρ	h_e (in.)	k	F_{cr} (ksi)	λ	ρ	b_{fe} (in.)	A_e (in^2)	$P_{n,c}$ (kips)
A1	6.97	76	0.122	N/A	12.9	1.28	142	0.090	N/A	4.60	4.4	5
B1	6.97	76	0.449	N/A	12.9	1.28	24	0.795	0.91	11.5	6.9	106
C1	6.97	90	0.484	N/A	12.9	1.28	26	0.894	0.84	12.3	8.3	174
D1	6.97	105	0.375	N/A	13.0	1.28	12	1.10	0.73	9.14	5.7	84
E1	6.97	98	0.478	N/A	12.9	1.28	25	0.94	0.81	11.9	8.1	181
F1	6.97	126	0.427	N/A	12.9	1.28	18	1.12	0.72	10.4	7.4	169
G1	6.97	117	0.454	N/A	12.9	1.28	17	1.19	0.69	10	7.0	169

Table F.3- AISI-DSM calculations summary

Pile	Overall Buckling Load				Local Buckling Load			$P_{n,c}$ (kips)
	P_y (kips)	P_{cre} (kips)	λc	P_{ne} (kips)	P_{crl} (kips)	λ_l	P_{nl} (kips)	
A1	144	6	5.03	5	333	0.122	5	5
B1	239	132	1.35	112	177	0.795	110	110
C1	304	284	1.03	194	243	0.894	178	178
D1	215	112	1.38	97	79	1.104	77	77
E1	303	323	0.969	205	231	0.942	181	181
F1	290	333	0.932	201	159	1.12	158	158
G1	281	376	0.864	205	145	1.19	156	156

APPENDIX G : FEA vs. Code Provisions Comparison

To highlight the need to implement appropriate numerical frameworks to determine the axial capacity and behavior of compressive members with localized corrosion, a comparison between the axial capacity results obtained through finite element analysis and code methods (AISC, AISI-EWM and AISI-DSM) is presented herein. A summary of those results, including the maximum, minimum and average capacities determined through code provisions, and the corresponding ratios with respect to the capacities obtained through finite element analysis are presented in Table G.1.

Table G.1- Field inspection geometry data

Pile	**Capacity (kips)**				**FEA/Codes Comparison**		
	AISC	AISI-DSM	AISI-EWM	FEA	FEA/AISC	FEA/DSM	FEA/EWM
A1	5	5	5	47	9.4	9.4	9.4
B1	76	106	110	153	2.0	1.4	1.4
C1	117	174	178	207	1.8	1.2	1.2
D1	40	84	77	145	3.6	1.7	1.9
E1	115	181	181	209	1.8	1.2	1.2
F1	85	169	158	200	2.4	1.2	1.3
G1	79	169	156	191	2.4	1.1	1.2
A2*	39	68	73	96	2.5	1.4	1.3
B2	99	125	126	184	1.9	1.5	1.5
C2	159	203	214	225	1.4	1.1	1.1
D2	12	12	12	64	5.1	5.1	5.1
E2	5	5	5	58	11.5	11.5	11.5
F2	38	41	41	84	2.2	2.1	2.1
G2	76	163	151	177	2.3	1.1	1.2
A3*	49	49	49	155	3.2	3.2	3.2
B3	33	46	48	85	2.5	1.8	1.8
C3	32	32	32	93	2.9	2.9	2.9
D3	15	15	15	71	4.8	4.8	4.8
E3	53	53	53	133	2.5	2.5	2.5
F3	29	29	29	109	3.7	3.7	3.7
G3	200	250	262	244	1.2	1.0	0.9
A4	66	69	69	149	2.3	2.2	2.2
B4	4	4	4	26	5.8	5.8	5.8
C4	61	78	78	115	1.9	1.5	1.5

(Table G.1 continued)

Pile	Capacity (kips)				FEA/Codes Comparison		
	AISC	AISI-DSM	AISI-EWM	FEA	FEA/AISC	FEA/DSM	FEA/EWM
D4	6	6	6	48	7.7	7.7	7.7
E4	0	0	0	2	80.1	80.1	80.1
F4	26	26	26	85	3.3	3.3	3.3
G4	30	30	30	88	2.9	2.9	2.9
A5	37	42	43	28	0.8	0.7	0.7
B5	38	83	71	50	1.3	0.6	0.7
C5	7	7	7	55	7.5	7.5	7.5
D5	42	43	43	100	2.4	2.3	2.3
E5	36	62	63	91	2.5	1.5	1.5
F5	32	32	32	110	3.5	3.5	3.5
G5	88	113	116	148	1.7	1.3	1.3
A6*	35	107	112	126	3.6	1.2	1.1
B6	12	12	12	69	5.7	5.7	5.7
C6	4	4	4	36	8.7	8.7	8.7
D6	28	28	28	79	2.9	2.8	2.8
E6	5	5	5	58	11.5	11.5	11.5
F6	17	17	17	67	4.0	4.0	4.0
G6	87	140	139	162	1.9	1.2	1.2
A7*	71	143	135	190	2.7	1.3	1.4
B7	60	117	113	144	2.4	1.2	1.3
C7	47	62	63	116	2.5	1.9	1.9
D7	96	103	103	174	1.8	1.7	1.7
E7	43	64	65	106	2.5	1.7	1.6
F7	28	28	28	108	3.9	3.9	3.9
G7	46	51	51	108	2.3	2.1	2.1
A8	20	74	78	91	4.7	1.2	1.2
B8	122	142	148	120	1.0	0.8	0.8
C8	35	131	93	107	3.0	0.8	1.1
D8	126	196	209	210	1.7	1.1	1.0
E8	52	71	73	154	3.0	2.2	2.1
F8	69	69	69	158	2.3	2.3	2.3
G8	56	88	88	116	2.1	1.3	1.3
A9	91	145	146	174	1.9	1.2	1.2
B9	26	26	26	73	2.8	2.8	2.8
C9	41	55	56	124	3.0	2.3	2.2
D9	25	81	71	108	4.3	1.3	1.5
E9	44	94	85	153	3.5	1.6	1.8
F9	190	236	249	240	1.3	1.0	1.0
G9	36	73	71	99	2.8	1.4	1.4
A10	103	111	111	191	1.9	1.7	1.7

(Table G.1 continued)

Pile	Capacity (kips)				FEA/Codes Comparison		
	AISC	AISI-DSM	AISI-EWM	FEA	FEA/AISC	FEA/DSM	FEA/EWM
B10	17	17	17	86	5.2	5.2	5.2
C10	23	66	70	89	3.9	1.3	1.3
D10	23	85	89	99	4.3	1.2	1.1
E10	1	1	1	21	29.3	29.3	29.3
F10	59	60	60	124	2.1	2.1	2.1
G10	74	112	116	131	1.8	1.2	1.1
A11	36	110	120	136	3.8	1.2	1.1
B11	48	115	117	135	2.8	1.2	1.2
C11	27	27	27	83	3.1	3.1	3.1
D11	4	4	4	37	8.7	8.7	8.7
E11	14	14	14	53	3.8	3.8	3.8
F11	19	19	19	74	4.0	4.0	4.0
G11	72	73	73	146	2.0	2.0	2.0
A12	85	85	85	44	0.5	0.5	0.5
B12	103	125	124	90	0.9	0.7	0.7
C12	22	65	66	87	4.0	1.4	1.3
D12	55	55	55	149	2.7	2.7	2.7
E12	50	52	52	111	2.2	2.1	2.1
F12	20	20	20	82	4.2	4.2	4.2
G12	41	75	72	97	2.4	1.3	1.4
A13	36	49	51	88	2.4	1.8	1.7
B13	25	45	41	46	1.8	1.0	1.1
C13	45	85	82	124	2.7	1.5	1.5
D13	46	120	126	140	3.0	1.2	1.1
E13	28	79	72	105	3.7	1.3	1.5
F13	54	81	82	124	2.3	1.5	1.5
G13	104	189	181	206	2.0	1.1	1.1
A14	185	230	241	235	1.3	1.0	1.0
B14	171	209	214	224	1.3	1.1	1.0
C14	54	106	106	129	2.4	1.2	1.2
D14	24	87	90	100	4.2	1.2	1.1
E14	23	71	71	86	3.7	1.2	1.2
F14	52	135	135	146	2.8	1.1	1.1
G14	38	120	120	124	3.3	1.0	1.0
A15	63	142	149	161	2.6	1.1	1.1
B15	72	140	145	161	2.3	1.2	1.1
C15	20	80	77	95	4.6	1.2	1.2
D15	17	76	70	89	5.2	1.2	1.3
E15	63	140	136	169	2.7	1.2	1.2
F15	144	203	208	216	1.5	1.1	1.0

(Table G.1 continued)

Pile	Capacity (kips)				FEA/Codes Comparison		
	AISC	AISI-DSM	AISI-EWM	FEA	FEA/AISC	FEA/DSM	FEA/EWM
G15	71	161	164	163	2.3	1.0	1.0
A16	42	90	93	79	1.9	0.9	0.9
B16	71	138	141	161	2.3	1.2	1.1
C16	39	55	57	100	2.6	1.8	1.8
D16	71	81	81	143	2.0	1.8	1.8
E16	82	135	141	158	1.9	1.2	1.1
F16	88	174	179	185	2.1	1.1	1.0
G16	43	131	118	139	3.2	1.1	1.2
A17	4	4	4	38	9.5	9.5	9.5
B17	17	17	17	88	5.2	5.2	5.2
C17	49	121	123	138	2.8	1.1	1.1
D17	43	112	99	140	3.3	1.3	1.4
E17	47	124	107	163	3.5	1.3	1.5
F17	27	103	93	116	4.3	1.1	1.3
G17	40	127	112	136	3.4	1.1	1.2
A18	102	178	184	203	2.0	1.1	1.1
B18	12	12	12	71	5.9	5.9	5.9
C18	38	108	114	124	3.2	1.2	1.1
D18	40	57	59	97	2.4	1.7	1.7
E18	58	76	78	120	2.1	1.6	1.5
F18	6	6	6	53	8.7	8.7	8.7
G18	48	53	53	87	1.8	1.6	1.6
A19	112	183	188	213	1.9	1.2	1.1
B19	43	43	43	146	3.4	3.4	3.4
C19	47	47	47	120	2.6	2.6	2.6
D19	35	102	88	128	3.6	1.3	1.5
E19	38	38	38	115	3.0	3.0	3.0
F19	37	37	37	128	3.5	3.5	3.5
G19	109	128	128	224	2.1	1.7	1.7
A20	104	104	104	208	2.0	2.0	2.0
B20	18	18	18	92	5.2	5.2	5.2
C20	67	106	106	158	2.4	1.5	1.5
D20	66	76	76	131	2.0	1.7	1.7
E20	45	93	87	129	2.9	1.4	1.5
F20	51	76	78	102	2.0	1.3	1.3
G20	94	115	117	141	1.5	1.2	1.2
* indicates haunch				**Max**	80.1	80.1	80.1
** indicates void in web				**Min**	0.5	0.5	0.5
				Mean	3.9	3.1	3.1

APPENDIX H : Stiffness Modification Factor Calculations

The calculations conducted to determine the cracked moment of inertia of the longitudinal concrete beams with 48x24, and 48x15 cross-sections are summarized and presented in Table H.1. The effective widths of these beams were determined according to the provisions in ACI 318 (2014). These calculations were based on minimum reinforcement requirements and a uniform slab thickness of 8 in.

Table H.1- Cracked moment of inertia of longitudinal beams

Beam	Material Properties		Beam Dimensions			Cross-Section Properties		
	Es (ksi)	Ec (ksi)	b_{eff} (in.)	h (in.)	d (in.)	Ig (in.^{4})	Icr (in.^{4})	Icr/Ig
48x15	29000	3605	33.0	48.0	46.5	187008	20787	0.11
48x24	29000	3605	78.0	48.0	46.5	349161	34659	0.10
18x15	29000	3605	69.0	18.0	16.5	13748	3236	0.24
72x36	29000	3605	72.0	72.0	70.5	1386701	171694	0.12

Based on the values of Icr/Ig presented in Table H.1, a modification factor of 0.10 was selected and applied to the flexural stiffness of the superstructure of the wharf in order to represent the assumption of cracked concrete sections for analysis.

In the analysis of the influence of the distribution of corroded piles, an additional level of stiffness of the superstructure was included. The corresponding superstructure stiffness modification factor was determined based on the effective moment of inertia of the longitudinal when the applied load reached approximately 1.3 times the load for cracking of the concrete, under the assumption of simply supported beams. In this sense, the effective moment of inertia of the beams was determined according to ACI 318 (2014), and given as

$$I_e = \left(\frac{Mcr}{Ma}\right)^3 Ig + \left[1 - \left(\frac{Mcr}{Ma}\right)^3\right] Icr \ \leq Ig \ , \qquad \text{(H-1)}$$

where I_e is the effective moment of inertia of the beam at the given load level, M_a is the simply supported moment corresponding to the applied load and M_{cr} is the cracking moment of the beam.

In this procedure, M_a/M_{cr} was maintained at approximately 1.30. The calculations are presented in Table H.2.

Table H.2- Effective moment of inertia of longitudinal beams

Dimensions	Span (in.)	wa/wcr	Ie (in^4)	Ie/Ig
48x15	216	1.30	96445	0.52
48x24	216	1.30	177809	0.51
18x15	216	1.30	8021	0.58
72x36	216	1.30	724724	0.52

From these calculations, the intermediate superstructure stiffness modification factor was set at 0.50, for the analysis of the influence of the distribution of the corroded piles on the collapse load of the wharf.